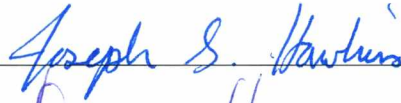# RAY TRACING APPLICATIONS FOR HIGH-FREQUENCY RADAR: CHARACTERIZING ARTIFICIAL LAYERS AND BACKGROUND DENSITY PERTURBATIONS IN THE IONOSPHERE

By

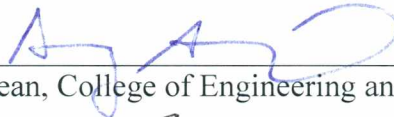Timothy E. Theurer

RECOMMENDED:

Advisory Committee Chair

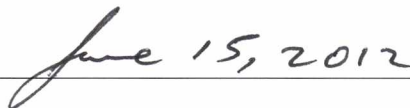_Chair, Electrical & Computer Engineering Department_

APPROVED:

Dean, College of Engineering and Mines

Dean of the Graduate School

June 15, 2012

Date

RAY TRACING APPLICATIONS FOR HIGH-FREQUENCY RADAR:

CHARACTERIZING ARTIFICIAL LAYERS AND BACKGROUND DENSITY

PERTURBATIONS IN THE IONOSPHERE

A

THESIS

Presented to the Faculty

of the University of Alaska Fairbanks

in Partial Fulfillment of the Requirements

for the Degree of

MASTER OF SCIENCE

By

Timothy E. Theurer, B.S.

Fairbanks, Alaska

August 2012

Abstract

In this thesis a numerical method of calculating ground-scattered power from the results of a ray tracing analysis is presented. The method is based on a conservation of energy approach and offers advantages over an alternative method derived from the radar equation. The improved numerical method is used to investigate two different physical phenomena by comparison with measured ground-scattered power observed by a high-frequency (HF) radar located in Kodiak, AK that is part of the Super Dual Auroral Radar Network (SuperDARN). First, the effects of artificial electron density layers on observed ground scatter is studied through a comparison of simulated and measured power profiles. The results demonstrate that the location and spatial dimensions of artificial layers may be estimated by a comparison of the location and amplitude of simulated and measured power enhancements. Second, a Monte-Carlo simulation method is used to characterize the temporal distribution of ground-scattered power. Random processes including background electron density perturbations, polarization, noise, and sample correlation are modeled in simulation and used to estimate statistical moment profiles. The simulated statistical moment profiles are compared to measured profiles as a means of model verification and to roughly approximate background electron density perturbations in the ionosphere.

Table of Contents

List of Figures

List of Tables

List of Appendices

Chapter 1   Introduction

1.1 Objective

In this thesis, ray tracing techniques and observations made by a high-frequency (HF) radar are used to characterize the structure of artificial density layers and the statistical properties of ground scatter observed by an over-the-horizon (OTH) radar. High-power HF heating experiments recently have been shown to produce artificial density layers in the ionosphere, which have been observed using both optical instruments and ionosondes [*Pedersen et al.*, 2009; *Pedersen et al.*, 2010]. The ability to generate artificial layers may have important radio applications, particularly for HF communications. The analysis performed in this thesis provides an independent tool for investigating both the structure of these artificial layers as well as potential radio applications.

The other concentration of this thesis is the statistics of ground scatter observed by OTH HF radars. By identifying influential random processes and using a Monte-Carlo simulation technique, the mean and standard deviation of ground scatter distributions versus time delay range are estimated and compared to observations. A comparison of simulation results and measurements yields insight into random ionospheric processes and a tool for resolving desired targets from clutter.

The topics studied here are just two applications of a numerical method for calculating ground-scattered power that is presented in Chapter 3. Through detailed modeling and an analysis of simulated and measured results, this thesis provides an independent tool for studying artificial density layers as well as insight into the physical phenomena that contribute to ground clutter distributions for HF OTH radars. Before exploring the focus of this thesis, sections 1.2-1.4 provide a brief introduction to the ionosphere, radio wave propagation in the ionosphere, and the background of the SuperDARN program.

1.2 The Ionosphere

As radiation from the sun enters the Earth's atmosphere, energetic photons ionize neutral gas molecules creating free ions and electrons [*Davies*, 1965]. The amount of ionization that occurs depends on gas density and composition with the greatest concentration of free charge produced in the altitude region 60-600 km, which is termed the ionosphere [*Budden*, 1985]. Above the ionosphere the atmosphere is nearly fully ionized but sparsely populated whereas below the ionosphere the density of neutral gas molecules and the absorption of radiation at high altitudes results in a small degree of ionization.

The structure of the ionosphere in altitude is influenced by the composition of gas and is typically divided into layers corresponding to local maximums in electron density. The principal layers include the E and F layers, which have peak altitudes in the range 100-110 km and 200-400 km [*Budden*, 1985]. A typical altitude cross-section of electron density depicting the principal layers is illustrated in Figure 1.1.
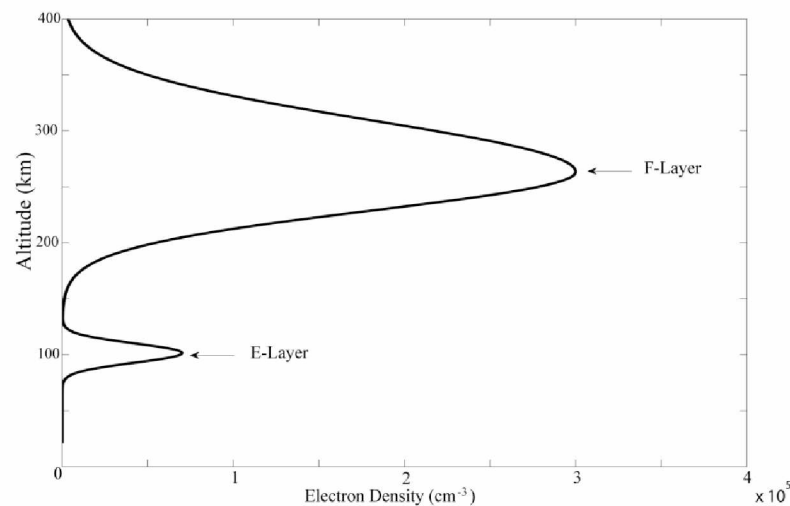
Figure 1.1: Example ionosphere density profile versus altitude illustrating principal layers. The density profile illustrated here was generated with arbitrary values of peak electron density and a Gaussian distribution of density with altitude for illustration purpose only.

The structure of the ionosphere is often assumed to be spherically symmetric due to the symmetry in the neutral atmosphere. In this thesis, ray-tracing is restricted to two-dimensions so that variations in the horizontal dimension may be investigated but variations in the lateral dimension are neglected. Restricting ray-tracing to two dimensions and ignoring out-of-plane deviations has been shown to be sufficiently accurate for applications such as simulating ionograms and performing coordinate-registration for OTH radars [*Coleman* 1994, *Coleman* 1997, *Coleman* 1998]. Appendix II is devoted to investigating the effects of the lateral structure of artificial density layers, which cannot be determined from the ray-tracing performed here.

1.3 Radio Wave Propagation in the Ionosphere

A variety of physical phenomena contribute to how radio waves propagate in the ionosphere. The most important of these include the presence of free charges, particle collisions, and the influence of the Earth's magnetic field. From the viewpoint of an electrical engineer, the influence of these physical phenomena is elegantly summarized in the relationship between electric field intensity $\vec{E}$ and the displacement flux $\vec{D}$, or the permittivity ε, in the ionosphere. Maxwell's equations along with the expression for permittivity can be used to determine the fundamental characteristics of waves in the ionosphere. Here the subjects of wave polarization, phase-refractive index, and energy propagation for radio waves in the ionosphere are briefly presented. Note that the relationships derived here are conditioned on the important assumption that the ionosphere can be treated as a homogeneous plasma.

A plasma can be defined as a quasi-neutral gas that exhibits collective behavior. The quasi-neutrality condition implies that free charge is approximately evenly distributed between ions and electrons, or positive and negative charges. Collective behavior refers to the idea that motion in the plasma depends on the state of the plasma as a whole rather than any local volume. A plasma demonstrates collective behavior on scale sizes that exceed a constant called the Debye length, which is the physical distance at which a potential introduced in a plasma decays by factor of e^{-1} due to shielding by

opposing charges [*Chen*, 1984]. If a process occurs over scale sizes much larger than a Debye length than the plasma acts collectively like a fluid. Typical Debye lengths in the ionosphere are on the order of centimeters so for high-frequency radio waves the ionosphere can be treated as a plasma [*Budden*, 1985].

1.3.1 Permittivity

The permittivity of the ionosphere is derived by considering the influence of free charge, particle collisions, and the Earth's magnetic field, which are related by the force balance equation

$$\vec{E}q + q\frac{\partial \vec{r}}{\partial t} \times \vec{B} - m\nu\frac{\partial \vec{r}}{\partial t} = m\frac{\partial^2 \vec{r}}{\partial t^2}.$$ (1.1)

In (1.1), $\vec{r}$ represents the displacement of the charges due to the electric field, $\vec{B}$ represents a constant background magnetic field from the Earth, ν represents the average number of particle collisions per unit time, q is the total charge per unit volume, and m is the total mass equivalent to the particle density N times the mass of a single charge. Note that the three terms on the left hand side (LHS) of (1.1) are the forces exerted by the electric field, magnetic field, and particle collisions on the plasma as a whole. Considering that the mass of ions is on the order of 10^3 greater than the mass of electrons, the acceleration experienced by ions is correspondingly 10^3 smaller than the acceleration experienced by electrons. Therefore, the assumption will be made that the ions are stationary and that $q = Ne$, which is the total number of free electrons [*Budden*, 1985].

Now define $\vec{P} = Ne\vec{r}$ as the electric polarization vector where $\vec{D} = \varepsilon_0\vec{E} + \vec{P}$. If (1.1) is multiplied through by the factor $\frac{e}{m\omega^2}$, the expression in (1.1) can be re-written as

$$\frac{Ne^2}{m\omega^2}\vec{E} + \frac{e}{m\omega^2}\frac{\partial \vec{P}}{\partial t} \times \vec{B} - \frac{\nu}{\omega^2}\frac{\partial \vec{P}}{\partial t} = \frac{1}{\omega^2}\frac{\partial^2 \vec{P}}{\partial t^2}.$$ (1.2)

At this point, consider that the field vectors $\vec{E}$ and $\vec{P}$ can be written in the form $\vec{A} = \vec{A_0}e^{j\omega t}$, which corresponds to time-harmonic waves. Time derivatives of the fields can be simply replaced with the term $j\omega$ and (1.2) can be simplified to

$$-\varepsilon_0 X \vec{E} = U\vec{P} + i\vec{P} \times \vec{Y} \tag{1.3}$$

where $= \frac{Ne^2}{\varepsilon_0 m \omega^2}$, $\vec{Y} = \frac{\vec{B}e}{m\omega}$, and $U = 1 - i\frac{\nu}{\omega}$. The values X and $Y = |\vec{Y}|$ have physical significance and are termed the plasma frequency and electron gyro-frequency [*Budden*, 1985]. It is important to note the presence of a cross product on the right-hand side (RHS) of (1.3). The presence of a cross-product implies that the components of $\vec{E}$ are dependent on multiple components of $\vec{P}$. In general, the exact relationship between $\vec{E}$ and $\vec{P}$ depends on the geometry between the wave normal $\vec{k}$ and the magnetic field. Consider the diagram in Figure 1.2, which illustrates a Cartesian coordinate system with a plane wave propagating in the $\hat{z}$ direction and the field vector $\vec{Y}$ at an angle of θ to the z-axis.
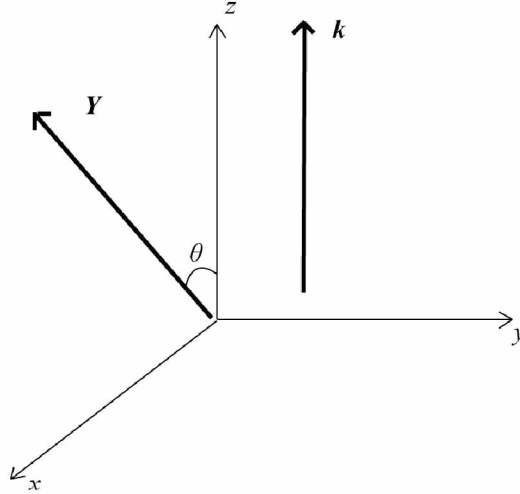
Figure 1.2: Geometry of $\vec{Y}$, θ, and $\vec{k}$ used to develop permittivity tensor.

Using the geometry of Figure 1.2 , the relationship in (1.3) reduces to

$$-\varepsilon_0 X \begin{bmatrix} E_x \\ E_y \\ E_z \end{bmatrix} = \begin{bmatrix} U & jY\cos\theta & 0 \\ -jY\cos\theta & U & jY\sin\theta \\ 0 & -jY\sin\theta & U \end{bmatrix} \begin{bmatrix} P_x \\ P_y \\ P_z \end{bmatrix}. \tag{1.4}$$

Similarly, the displacement flux can be expressed as $\vec{D} = \varepsilon_0 \vec{E} + \vec{P} = \varepsilon_0 \overleftrightarrow{\varepsilon} \vec{E}$ where $\overleftrightarrow{\varepsilon}$ is a tensor given by

$$\overleftrightarrow{\mathcal{E}} = \begin{bmatrix} \frac{1}{2}(\varepsilon_1+\varepsilon_2)\cos^2\theta+\varepsilon_3\sin^2\theta & \frac{1}{2}j(\varepsilon_1-\varepsilon_2)\cos\theta & \left(\frac{1}{2}(\varepsilon_1+\varepsilon_2)+\varepsilon_3\right)\sin\theta\cos\theta \\ -\frac{1}{2}j(\varepsilon_1-\varepsilon_2)\cos\theta & \frac{1}{2}(\varepsilon_1+\varepsilon_2) & -\frac{1}{2}j(\varepsilon_1-\varepsilon_2)\sin\theta \\ \left(\frac{1}{2}(\varepsilon_1+\varepsilon_2)+\varepsilon_3\right)\sin\theta\cos\theta & \frac{1}{2}j(\varepsilon_1-\varepsilon_2)\sin\theta & \frac{1}{2}(\varepsilon_1+\varepsilon_2)\sin^2\theta+\varepsilon_3\cos^2\theta \end{bmatrix}, \quad (1.5)$$

and

$$\begin{cases} \varepsilon_1 = 1 - X/(U+Y) \\ \varepsilon_2 = 1 - X/(U-Y). \\ \quad \varepsilon_3 = 1 - X/U \end{cases} \quad (1.6)$$

The significance of (1.5) is that $\vec{D}$ depends on multiple components of $\vec{E}$, which is characteristic of an anisotropic medium. Using Maxwell's equations and the permittivity tensor in (1.5), it can be shown that anisotropy affects wave polarization, phase refractive index, and energy propagation in the ionosphere.

1.3.2 Polarization

An important consequence of anisotropy between $\vec{E}$ and $\vec{D}$ in the ionosphere is that a limited number of wave polarizations can exist. Specifically, using Maxwell's equations and the tensor in (1.5), the polarization ρ expressed as the ratio of E_x/E_y can be shown to be restricted to two values given by

$$\rho = \frac{\frac{1}{2}iY\sin^2\theta \pm i\left[\frac{1}{4}Y^2\sin^4\theta+\cos^2\theta(U-X)^2\right]}{(U-X)\cos\theta}. \quad (1.7)$$

The two values of polarization that can exist are often distinguished as the ordinary and extraordinary polarizations [*Budden*, 1985].

1.3.3 Index of Refraction

Anisotropy also plays a pivotal role in the expression for phase refractive index, which under the assumption that the ionosphere is a cold, collision-less plasma simplifies to

$$\mu_p{}^2 = 1 - \frac{X(1-X)}{1-X-\frac{1}{2}Y_t{}^2\pm\left\{\frac{1}{4}Y_t{}^4+Y_l{}^2(1-X)^2\right\}^{1/2}} \quad (1.8)$$

where $Y_t = Y \sin\theta$ and $Y_l = Y \cos\theta$. (1.8) is known as the Appleton-Hartree equation for a cold collision-less plasma. Note that the $\pm$ in the denominator of the Appleton-Hartree equation corresponds to ordinary and extraordinary polarizations respectively. Consequently, the ionosphere is birefringent medium where refraction depends on polarization [*Budden*, 1985].

1.3.4 Energy Propagation

For time-harmonic waves, energy propagation can be shown to be in the direction of the time-average Poynting vector expressed as

$$\vec{S} = \frac{1}{2}\text{Re}\left[\vec{E} \times \vec{H}^*\right]. \tag{1.9}$$

For plane waves in isotropic media, $\vec{S}$ is directed along the wave normal so that energy and phase propagate in the same direction [*Rao*, 2004]. However, in anisotropic media the coupling between different components of $\vec{D}$ and $\vec{E}$ leads to energy propagation in a direction other than the wave normal. Given the geometry illustrated in Figure 1.2, it can be shown that in the case of collision-less plasmas the components of $\vec{S}$ are

$$\vec{S} = \begin{pmatrix} S_x \\ S_y \\ S_z \end{pmatrix} = \begin{pmatrix} \frac{j\rho\mu_p(\mu_p^2-1)Y\sin\theta}{2Z_0(1-X)}|E_x|^2 \\ 0 \\ \frac{\mu_p(1-\rho^2)}{2Z_0}|E_x|^2 \end{pmatrix} \tag{1.10}$$

where Z_0 is the impedance of free space and the values of ρ and μ_p are given by (1.7) and (1.8) [*Budden*, 1985]. Note that (1.10) illustrates that energy propagates in the (x, z) plane which is offset from the wave normal by an angle of

$$\alpha = \tan^{-1}\left(\frac{iY\rho\sin\theta(\mu_p^2-1)}{(1-\rho^2)(1-X)}\right). \tag{1.11}$$

1.4 SuperDARN

The Super Dual Auroral Radar Network (SuperDARN) consists of a global network of HF radars used to perform high-latitude ionospheric research [*Greenwald et al.*, 1985, 1995]. Each radar measures line-of-sight (LOS) plasma velocity at ranges up to 3500 km and over a field of view (FOV) of approximately 56° in order to provide an instantaneous mapping of ionospheric convection. Although the main objective of SuperDARN is providing a real time map of ionospheric convection, the radars also provide a valuable tool for investigating a variety of other ionospheric phenomena ranging from gravity waves to artificial field-aligned irregularities produced by high power HF heaters [*Bristow and Greenwald* 1995; *Wright et al.*, 2009; *Wright et al.*, 2006].

In this thesis, the SuperDARN radar located in Kodiak, Alaska is used to provide observations of ground scatter. The SuperDARN radar observes ground scatter when a transmitted pulse launched by the radar refracts through the ionospheres and scatters off the ground. For the purpose of characterizing artificial layers in Chapter 4, ground scatter measurements made at Kodiak are analyzed and compared to simulation results during a period of time when an artificial layer is induced at the High Frequency Active Auroral Research Program (HAARP) station in Gakona, Alaska. In Chapter 5, measured statistical moment profiles made during a short interval of time are analyzed and compared to simulation results to study clutter distributions and to quantify physical phenomena such as background density perturbations.

Chapter 2   Ray Theory

2.1 Introduction

Ray tracing is a useful tool for determining the path of electromagnetic waves in anisotropic mediums. In this chapter a brief description of ray theory and its limitations are presented before developing ray path equations by applying variational calculus to Fermat's principle of least time. Next, the general form of ray path equations as derived by Haselgrove are presented along with the derivations of the explicit ray path equations in a cold-collisionless plasma. Finally, the ray tracing software and the specific numerical integration algorithm utilized in this thesis are discussed.

2.2 Ray Theory

Consider the wave equation in free space which has the form

$$\nabla^2 E + (\beta_0 \mu)^2 E = 0 \tag{2.1}$$

where β_0 is the free space phase propagation constant and μ is the (possibly complex) index of refraction. The solution to (2.1) is a time-harmonic phasor of the form

$$\vec{E} = E_0 e^{-j\beta_0 \mu(\vec{r}\cdot\vec{n})} = E_0 e^{-j\beta_0 S(x,y,z)} \tag{2.2}$$

where $\vec{n}$ is a unit vector in the direction of phase propagation, $\vec{r}$ is a point in space, and the dot product of these vectors is the function $S(x, y, z)$. Now we would like to find the solution to the wave equation in the case that the refractive index varies with position, i.e. $\mu = \mu(x, y, z)$. Assume that the solution to the wave equation is almost (2.2) but let the amplitude of the field vary in space as well so that the (2.2) becomes

$$\vec{E} = E_0(x, y, z)e^{-j\beta_0 S(x,y,z)}. \tag{2.3}$$

After substituting (2.3) into the wave equation, simplifying, and re-arranging we obtain

$$E_0[\mu^2 - (\nabla S)^2] = (j/\beta_0)[E_0 \nabla^2 S + 2(\nabla E_0) \cdot (\nabla S)] - (\nabla^2 E_0/\beta_0{}^2). \tag{2.4}$$

If $\nabla^2 E_0 \ll \beta_0{}^2$ and $[E_0 \nabla^2 S + 2(\nabla E_0) \cdot (\nabla S)] \ll \beta_0$ the terms on the RHS of (2.4) can be ignored and the wave equation simplifies to

$$E_0 [\mu^2 - (\nabla S)^2] = 0. \tag{2.5}$$

Ignoring the trivial solution $E_0 = 0$, we have the relationship

$$\mu^2 = (\nabla S)^2, \tag{2.6}$$

which is known as the *iconal equation*. Under the condition that planes of constant phase and planes of constant amplitude are both normal to the phase propagation direction $\vec{n}$, it can be shown that

$$\mu \vec{n} = \nabla S. \tag{2.7}$$

The expression in (2.7) is the fundamental result of ray theory and states that waves propagate normal to surfaces of constant refractive index. Therefore, given a description of how the refractive index varies in space, the direction of wave propagation can be determined. However, (2.7) is only valid under the assumptions that $\nabla^2 E_0 \ll \beta_0{}^2$ and $[E_0 \nabla^2 S + 2(\nabla E_0) \cdot (\nabla S)] \ll \beta_0$. The restriction $\nabla^2 E_0 \ll \beta_0{}^2$ limits ray theory only to regions where the amplitude of the wave, E_0, does not vary rapidly which eliminates regions containing point sources. Similarly, the restriction $[E_0 \nabla^2 S + 2(\nabla E_0) \cdot (\nabla S)] \ll \beta_0$ limits ray theory to regions where both ∇S, which is proportional to the refractive index μ, and E_0 vary slowly over spatial lengths compared to a wavelength. In general, ray theory is an accurate approximation whenever wave parameters such as index of refraction and amplitude are constant relative to a wavelength [*Kelso*, 1964].

2.3 Fermat's Principle

Let us define a ray path as a curve that is everywhere tangent to the direction of energy propagation. Using the result in (2.7) derived from ray theory, the phase path φ of a wave traveling along a ray between points A and B in an anisotropic medium can be expressed as

$$\varphi = \int_A^B \mu_r \cos(\alpha) \, ds = S(B) - S(A) \tag{2.8}$$

where ds is taken along the phase path, $\mu_r = \frac{c}{v_r}$ is the ray refractive index (directed along the Poynting vector), α is the angle between the Poynting vector and the wave normal vector, and S is the function introduced in (2.2). Fermat's principle states that a ray will follow the path between two points that minimizes φ in (2.8). Mathematically, this principle is expressed as a variation of the integral in (2.8):

$$\delta \int_A^B \mu_r ds = 0. \tag{2.9}$$

The relationship in (2.9) signifies that the phase path φ in (2.8) will be a stationary point (a minimum) when (2.8) is integrated along the path that the wave travels. Given the condition imposed in (2.9) by Fermat's principle, one can apply the calculus of variations to the integrand in (2.8) to obtain a set of differential equations that describe ray paths through a medium whose index of refraction varies with position.

2.4 Application of Calculus of Variations

Consider the general functional I in (2.10),

$$I = \int_A^B F(y, \dot{y}, x) dx. \tag{2.10}$$

The value of I depends on the limits of integration, the integrand function $F(y, \dot{y}, x)$, and the curve $y(x)$. In many physical problems, the limits of integration and the form of the integrand function $F(y, \dot{y}, x)$ are known so the only way to manipulate the value of I is to vary the curve $y(x)$. Further, in some cases the value of I is known to be an extremum or a stationary value. The statement that I is stationary is equivalent to saying that first order changes in the curve $y(x)$ only produce second order changes in the value of I, which restricts the form of the curve $y(x)$. Mathematically, this condition is expressed as

$$\delta I = \delta \int_A^B F(y, \dot{y}, x) dx = 0. \tag{2.11}$$

It can be shown that for (2.11) to be valid, a differential equation called the *Euler-Lagrange* equation that is expressed in (2.12) must be satisfied:

$$\frac{\partial F}{\partial y} = \frac{d}{dx}\left(\frac{\partial F}{\partial \dot{y}}\right). \tag{2.12}$$

For a complete derivation of the Euler-Lagrange equation see *Riley* [2006] pp.835-836. Note that the Euler-Lagrange equation is a differential equation in y because the function F is known. If the integrand function in (2.10) depends on n dependent variables, $y_{1...n}$, their derivatives, and a single dependent variable x, then n separate but simultaneous Euler-Lagrange equations must be satisfied, each taking the form

$$\frac{\partial F}{\partial y_i} = \frac{d}{dx}\left(\frac{\partial F}{\partial \dot{y}_i}\right). \tag{2.13}$$

For the purpose of ray tracing, the integrand function F in (2.13) corresponds to the ray refractive index μ_r. In the ionosphere μ_r may be related to the phase refractive index μ_P as given by the Appleton-Hartree equation, which has dependent parameters including electron density and angle from the magnetic field that are in turn a function of the independent spatial coordinates (x, y, z).

2.5 Haselgrove Method

The principles of Hamiltonian optics were first applied to the problem of determining oblique ray paths through an anisotropic ionosphere by Haselgrove. The results of applying Haselgrove's method in Cartesian coordinates will be presented here and a detailed derivation of this method may be found in *Kelso* [1964] pp.331-339.

As discussed in the previous sections, Fermat's principle states that the phase path of a ray is a stationary point, which in anisotropic media leads to set a set of Euler-Lagrange equations relating the ray refractive index to various parameters. However, the ray refractive index μ_r is a function of the phase refractive index μ_P and the angle between the ray (energy) normal and wave (phase) normal directions. The set of Euler-Lagrange equations obtained from Fermat's principle is simplified by working with the phase refractive index μ_P instead of μ_r. The Haselgrove equations governing ray propagation in the ionosphere are

$$\begin{cases} \dfrac{du_{x,y,z}}{dt} = -c\dfrac{\partial G}{\partial(x,y,z)} \\[4mm] \dfrac{d(x,y,z)}{dt} = c\dfrac{\partial G}{\partial u_{x,y,z}} \end{cases} \tag{2.14}$$

where c is the velocity of light, and $\vec{u}$ and G are defined as

$$\vec{u} = \mu_p \vec{n}, \qquad (2.15)$$

and

$$G\left(x, y, z, u_x, u_y, u_z\right) = \frac{1}{\mu_p} |\vec{u}| = \frac{1}{\mu_p} u = 1. \qquad (2.16)$$

As defined previously, the vector $\vec{n}$ in (2.15) is a unit vector in the direction of phase propagation so that $\vec{u}$ has a magnitude equal to the local phase refractive index and is directed along the wave normal. The function G in (2.16) is the description of a surface where at every point on the surface the product of the magnitude of the vector $\vec{u}$ and the phase refractive index is unity. This surface is termed the wave normal surface. The six differential equations in (2.14) depend only on the integration variable t, position coordinates, direction of the wave normal, and the phase refractive index [*Kelso*, 1964].

2.6 Ray Path Equations for a Cold, Collision-less Plasma

In the previous section, six differential equations governing ray propagation in Euclidean space were presented in terms of position coordinates, wave normal direction, and the phase refractive index. A specific set of differential equations used by ray tracing software is obtained by evaluating the right hand side of (2.14) using the Appleton-Hartree equation for phase refractive index. As discussed in 1.3.3, the Appleton-Hartree equation for a cold, collision-less plasma is

$$\mu_P{}^2 = 1 - \frac{X(1-X)}{1-X-\frac{1}{2}Y_t{}^2 \pm \left\{\frac{1}{4}Y_t{}^4 + Y_l{}^2(1-X)^2\right\}^{1/2}}. \qquad (2.17)$$

Note from (2.17) and the previous definitions of X and $Y_{t/l}$ that μ_P is in general a function of electron density and the angle between the magnetic field and wave normal, i.e. $\mu_P = f(\theta, n_e)$. However, given that n_e is a function of position (x, y, z) and the angle θ is a function of the vector $\vec{u}$ directed along the wave normal, the phase refractive index can be written as $\mu_P = f\left(\theta\left(u_x, u_y, u_z\right), n_e(x, y, z)\right)$. The two expressions of interest in obtaining the differential equations used in the ray tracing software are the

partial derivatives of the wave normal surface function G with respect to position (x, y, z) and the wave normal direction $\vec{u}$.

The differential equations governing the wave normal vector $\vec{u}$ in (2.14) used in software are found by simplifying the term $-c \frac{\partial G}{\partial (x,y,z)}$. Noting that $G = \frac{1}{\mu_p} u$ and only μ_p is a function of position (x, y, z), the term $\frac{\partial G}{\partial x_k}$ reduces to

$$\frac{\partial G}{\partial x_k} = \frac{-u}{\mu_p^2} \frac{\partial \mu_p}{\partial x_k} = \frac{-1}{\mu_p} \frac{\partial \mu_p}{\partial n_e} \frac{\partial n_e}{\partial x_k}. \tag{2.18}$$

The positional derivatives $\frac{\partial n_e}{\partial x_k}$ can be calculated directly from the density profile used in simulation and the factor $\frac{\partial \mu_p}{\partial n_e}$ can be derived from (2.17) as

$$\frac{\partial \mu_p}{\partial n_e} = \frac{1}{2\mu_p} \frac{BC - AD}{C^2} \tag{2.19}$$

where

$$\begin{cases} A = X(1 - X) \\ B = \frac{X}{n_e}(1 - 2X) \\ C = 1 - X - \frac{1}{2}Y_t^2 \pm \left\{ \frac{1}{4}Y_t^4 + Y_l^2(1 - X)^2 \right\}^{1/2} \\ D = -\frac{X}{n_e} \mp Y_l^2(1 - X) \frac{X}{n_e} \left\{ \frac{1}{4}Y_t^4 + Y_l^2(1 - X)^2 \right\}^{-1/2} \end{cases} \tag{2.20}$$

The ray position equations in (2.14) are similarly derived by considering the term $\frac{\partial G}{\partial u_k}$. Substituting the expression $G = \frac{1}{\mu_p} u$ and applying the rules of differentiation yields

$$\frac{\partial G}{\partial u_k} = \left[\frac{1}{\mu_p} \frac{\partial u}{\partial u_k} - \frac{u}{\mu_p^2} \frac{\partial \mu_p}{\partial u_k} \right]. \tag{2.21}$$

Noting that

$$\frac{\partial u}{\partial u_k} = \frac{\partial}{\partial u_k} \left(\sqrt{u_x^2 + u_y^2 + u_z^2} \right) = \frac{u_k}{u}, \tag{2.22}$$

and

$$\frac{\partial}{\partial u_k} \left(\mu_p(\theta, n_e) \right) = \frac{\partial \mu_p}{\partial \theta} \frac{\partial \theta}{\partial u_k}, \tag{2.23}$$

then (2.21) reduces to

$$\frac{\partial G}{\partial u_k} = \left[\frac{1}{\mu_p}\frac{u_k}{u} - \frac{u}{\mu_p{}^2}\frac{\partial \mu_p}{\partial \theta}\frac{\partial \theta}{\partial u_k}\right].$$

(2.24)

Finally, noting that $|\vec{u}| = \mu_p$, the ray position equations in (2.14) may be written as

$$\frac{d(x,y,z)}{dt} = \frac{c}{\mu_p{}^2}\left[u_k - \mu_p\frac{\partial \mu_p}{\partial \theta}\frac{\partial \theta}{\partial u_k}\right]$$

(2.25)

where the term $\frac{\partial \mu_p}{\partial \theta}$ can be shown from (2.17) to be

$$\frac{\partial \mu_p}{\partial \theta} = X(1-X)\left\{1 - X - Y_tY_l \pm \frac{1}{2}\left\{\frac{1}{4}Y_t{}^4 + Y_l{}^2(1-X)^2\right\}^{-1/2}\left(Y_t{}^3Y_l - 2Y_lY_t(1-X)^2\right)\right\},$$

(2.26)

and the term $\frac{\partial \theta}{\partial u_k}$ can be derived from the inner product relation $\vec{B}\cdot\vec{u} = |\vec{B}||\vec{u}|\cos\theta$ to

be

$$\frac{\partial \theta}{\partial u_k} = \left[\frac{-B_k}{|\vec{B}||\vec{u}|} + \cos\theta\frac{u_k}{|\vec{u}|}\right]\frac{1}{\sin\theta},$$

(2.27)

where $\vec{B}$ is the local magnetic field.

In summary, using the Appleton-Hartree equation for a cold collisionless plasma the differential equations in (2.14) may be reduced to

$$\begin{cases} \dfrac{du_{x,y,z}}{dt} = \dfrac{1}{\mu_p}\dfrac{\partial \mu_p}{\partial n_e}\dfrac{\partial n_e}{\partial (x,y,z)} \\ \dfrac{d(x,y,z)}{dt} = \dfrac{c}{\mu_p{}^2}\left[u_{x,y,z} - \mu_p\dfrac{\partial \mu_p}{\partial \theta}\dfrac{\partial \theta}{\partial u_{x,y,z}}\right] \end{cases}$$

(2.28)

where the partial derivative on the RHS are evaluated using (2.19), (2.20), (2.26), and (2.27).

2.7 Ray Tracing Software

The original version of the ray tracing software used for the research presented in this thesis was developed at the John Hopkins University Applied Physics Laboratory. Given parameters specifying the ionospheric conditions and the desired number of rays and ray elevation angles, the ray tracing code numerically integrates the differential equations governing ray propagation illustrated in (2.28) over a two-dimensional grid.

The ionospheric density profile is modeled as a collection of layers that are normally distributed in elevation. The user may manipulate the peak density, peak density altitude, and width of each layer. In addition to the background profile, a variety of density perturbations may be added including sinusoidal perturbations, model gravity waves, and a model of the HAARP induced perturbation. Note that the electron density grid is populated in a spherically symmetric manner in order to account for the curvature of the earth.

The software is implemented in FORTRAN and consists of a collection of subroutines and data files. The parameters specifying the ionospheric conditions and the desired number of rays and elevation angles are passed to the software by modifying the appropriate text files prior to execution. A logical flow diagram of the main routine *raytrace.f* which serves as an envelope for the rest of the subroutines is depicted in Figure 2.1. The subroutines and/or data files associated with each logical partition of *raytrace.f* are also illustrated in Figure 2.1.

raytrace.f

↓

```
Populate electron density values on grid
             initdens.f, dparms.txt
Populate intensity and direction of magnetic field on grid
                  initfield.f
```

↓

(For each ray)

↓

```
Initialize current position and elevation angle
                 params.txt
```

↓

Calculate parameters at current position including:

$$n_e , \frac{\partial n_e}{\partial x,y,z}$$

$$\theta , \frac{\partial \theta}{\partial u_{x,y,z}}$$

$$\mu_p, \frac{\partial \mu_p}{\partial \theta} , \frac{\partial \mu_p}{\partial n_e}$$

} evaldens.f
bfield.f
plpars.f
getderivs.f

↓

```
Advance the ray using 4th order Runge-Kutta method
                  rayadv.f
```

↓

```
Record new ray position
       raypath.dat
```

↓

```
Test if new ray position is within grid domain
```

'Yes'

'No'

Figure 2.1: Logical flow diagram of envelope routine *raytrace.f*. Subroutines and data files at each stage are depicted.

2.7.1 Runge-Kutta Method

The cornerstone of the ray tracing software is the numerical integration of (2.28) using a fourth-order Runge-Kutta (RK4) method. Although more efficient methods of approximating solutions to ordinary differential equations (ODE's) are available, Runge-

Kutta methods can be simply implemented and only require knowledge of x_n in order to compute x_{n+1}.

The RK4 method approximates the solution to the initial value ODE problem

$$\begin{cases} x'(t) = f(t, x) \\ \quad x(a) = x_o \end{cases} \tag{2.22}$$

by using a sum of weighted slopes to estimate the value of $x(t + h)$. For the discrete case, the RK4 approximation to the ODE in (2.22) is

$$x_{n+1} = x_n + \frac{h}{6}(F_1 + F_2 + F_3 + F_4) \tag{2.23}$$

where

$$\begin{cases} \quad\quad F_1 = f(t_n, x_n) \\ F_2 = f(t_n + \frac{1}{2}h, x_n + \frac{1}{2}F_1) \\ F_3 = f(t_n + \frac{1}{2}h, x_n + \frac{1}{2}F_2) \\ \quad F_4 = f(t_n + h, x_n + F_3) \end{cases} \tag{2.24}$$

Note that the factors $F_{1..4}$ are approximations to the slope $x'(t)$ at the start, midpoint, and end of an interval of width h. The RK4 method can be simply but tediously derived from the Taylor series of $x(t + h)$ and $f(t + h, x + hf)$ by including the terms up to the one involving h^4. As the RK4 method replicates the terms of a Taylor series expansion up to h^4, it has a local truncation error of $O(h^5)$. A truncation error of $O(h^n)$ implies that the error converges to zero at a rate of h^n as the step size h approaches zero [*Kincaid and Cheney* 2002].

The current ray tracing code applies the RK4 method given a hard coded step size in the software without monitoring the local truncation error. The precision of the current ray tracing software would be improved by monitoring the local truncation error and dynamically altering the step size if the error exceeds some threshold. One efficient method of dynamically altering the integration step size is the Runge-Kutta-Fehlberg method which limits the truncation error at the cost of two additional function evaluations over the RK4 method.

Chapter 3   Estimation of Ground-Scattered Power from Ray Tracing[1]

3.1 Introduction

In this chapter we present a numerical method for calculating ground-scattered power from the results of ray tracing analysis. Comparing estimates of received power with measurements is a tool for studying ionospheric phenomena where the structure of the electron density profile directly influences the received power profile. The motivation for developing a new method of calculating ground-scattered power is discussed in Section 3.2 by illustrating the shortcomings of the derivation presented by *Bristow & Greenwald* [1995]. The method presented here is based on a conservation of energy approach and overcomes those shortcomings. In addition, we briefly introduce terrain cross section and a method of modeling terrain cross section in Section 3.4.

3.2 Bristow & Greenwald Method

Consider the radar geometry illustrated in Figure 3.1 where a pulse of length τ is transmitted from the origin at the elevation angle α, refracted by the ionosphere, and scatters from the ground at a distance x.
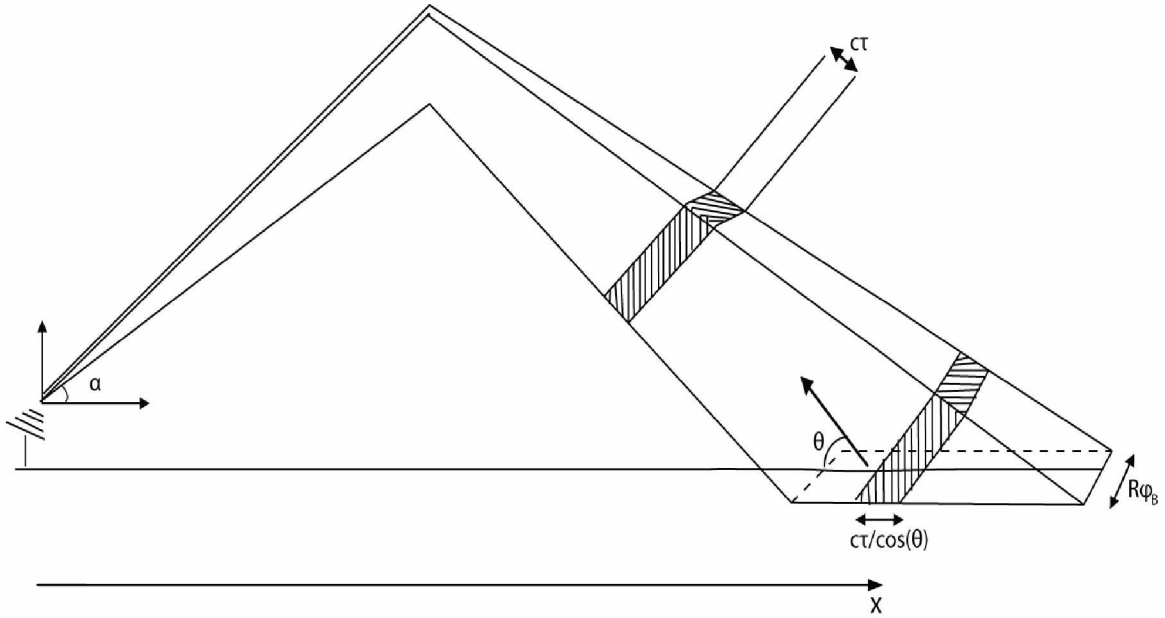
Figure 3.1: Illustration of radar geometry used in derivation of ground-scattered power by *Bristow & Greenwald 1995*.

The radar transmits over a beam broad in elevation but restricted in azimuth to a beam width of φ_b. The area subtended by the pulse on the ground is a function of the incidence angle θ, total ray path length R, beam width φ_b, and pulse length τ. Given the radar geometry illustrated in Figure 3.1, *Bristow & Greenwald* [1995] illustrated that the ground-scattered power could be calculated as

$$P_A = \sigma^0 P_t \varphi_b c \tau A_A G(\alpha, \varphi) f(\alpha) f(\theta) \sin(\alpha) \sin(\theta) \{8\pi R^3 \cos(\theta)\}^{-1} \qquad (3.1)$$

where σ^0 is the surface backscattering coefficient, P_t is the total transmitted power, and $G(\alpha, \varphi)$ is the antenna gain pattern as a function of take-off angle α and azimuth angle φ. The term $f(\alpha/\theta)$, labeled the focusing factor, in (3.1) accounts for the power focusing that is a function of the reflecting layer structure. The focus factor term was derived by *Bristow & Greenwald* [1995] as

$$f(\alpha) = R \left\{ \frac{\partial x}{\partial \alpha} \sin^2(\theta) \right\}^{-1}, \qquad (3.2)$$

and contains discontinuities at points where $\frac{\partial x}{\partial \alpha} \sin^2(\theta)$ approaches zero. In practice, it is assumed that the incidence angle θ equals the take-off angle α which is restricted to the angular extent 5-45 degrees by the antenna gain pattern so that discontinuities in the focus factor are only introduced by sign changes in the term $\partial x / \partial \alpha$. Sign changes in $\partial x / \partial \alpha$ are the result of a non-monotonic relationship between ground range and take-off angle and physically correspond to the intersection of rays on the ground. Numerically, these points of discontinuity result in arbitrarily large calculated power returns when using the *Bristow & Greenwald* [1995] method.

There are many common situations where the ionospheric conditions result in a non-monotonic relationship between ground range and take-off angle. For example, a strong E-layer in conjunction with an F-layer can produce two distinct regions of ground scatter where there exists a non-monotonic relationship between ground range and take-off angle. Figure 3.2 (a-c) illustrates a ray path plot, $x(\alpha)$ plot, and the calculated ground-scattered power plot in such a situation. Note that the ground-scattered power plot in Figure 3.2 (c) contains curves for two sets of take-off angles and demonstrates that discontinuities in $f(\alpha)$ result in an arbitrarily large received power, which in the limiting case approaches infinity.
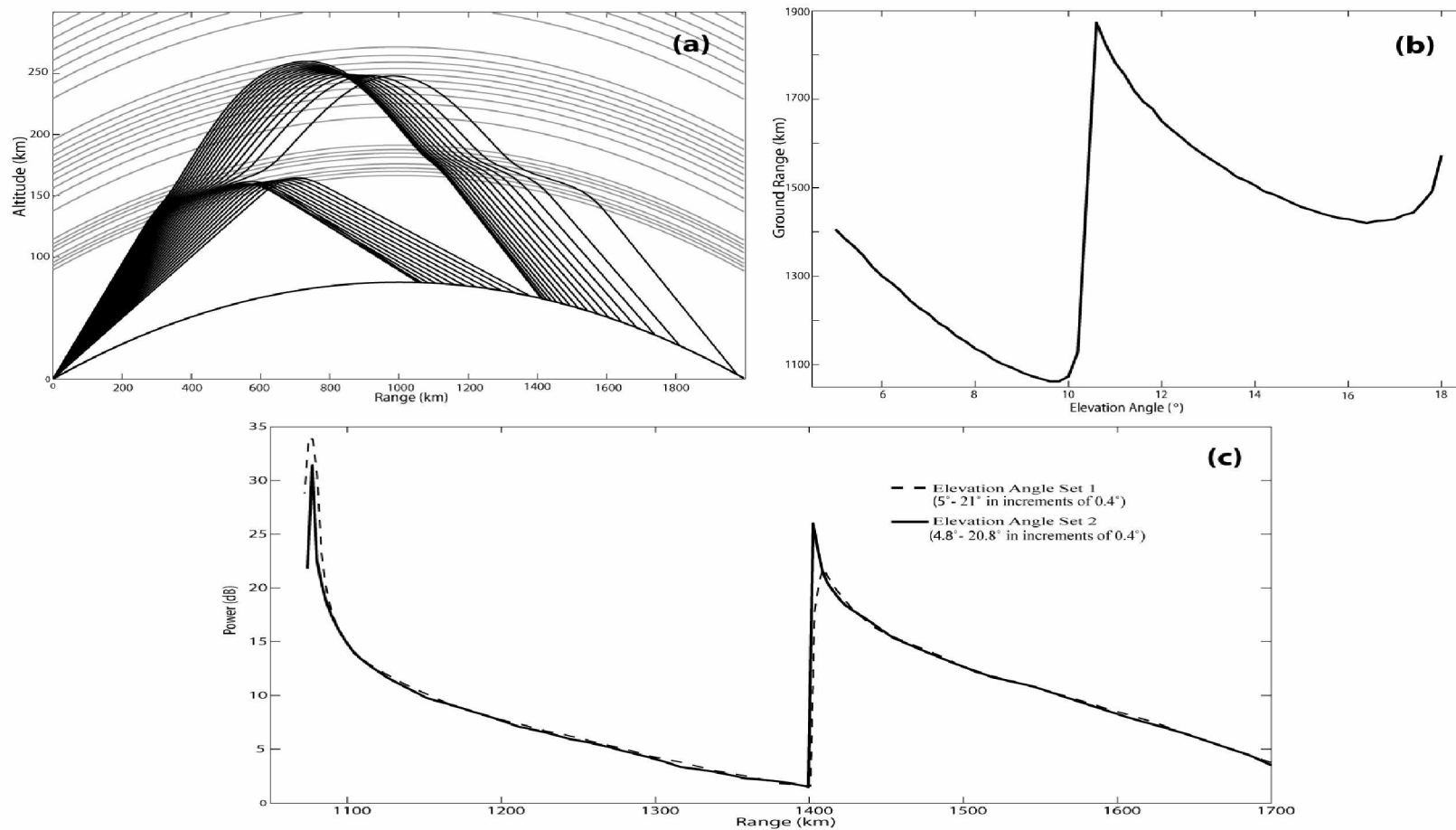
Figure 3.2: Comparison of (a) ray path plot, (b) $x(\alpha)$ plot where x is the ground distance to the scattering point for a ray launched at angle α, and (c) the calculated ground-scattered power plot given a background ionosphere with a strong E-layer in conjunction with an F-layer. Note (c) contains curves for two sets of take-off angles to illustrate the arbitrarily large power return calculated using the *Bristow & Greenwald* [1995] method at time delay range locations where $\partial x / \partial \alpha$ changes sign.

3.3 Beam Method

The derivation presented by *Bristow & Greenwald* [1995] is simply obtained from theory and can be readily applied to the results of a ray tracing analysis, but it fails to gracefully handle the common case where there is a non-monotonic relationship between ground range and take-off angle. A new approach based on simply the conservation of energy is presented here.

The distribution of power per unit solid angle of a transmitted pulse of power P_t is $S_t(\alpha) = P_t G(\alpha)/\{4\pi\}$ (W/Ω) where $G(\alpha)$ is the normalized antenna gain. In an unconstrained medium, power spreads in azimuth and elevation such that the power per unit area at a distance of R is $S_t R^{-2}$ (W/m^2). Here we assume power spreads normally in the azimuth direction so that the power per unit length-angle in elevation is $S_t R^{-1}$ (W/(rad $\cdot$ m)). However, the spreading in elevation is a function of ionospheric structure. Assuming that the target fills the beam in azimuth, the total power scattered from the illuminated area per unit elevation angle is $(S_t R^{-1})(R\varphi_B) = S_t \varphi_B$ which has units of (W/rad) and illustrates that scattered power is conserved in the azimuth dimension. The total scattered power from the illuminated area is

$$P_s(t) = \varphi_B \int_{\alpha_1}^{\alpha_2} \sigma^0(u)\, S_t(u)\, du \qquad (3.3)$$

where σ^0 is the surface backscattering coefficient to be discussed in section 3.4 and the limits of integration correspond to the illuminated angular extent. Given a transmitted pulse of length τ and the time delay to the scattering point as a function of elevation angle, $t_{delay}(\alpha)$ or equivalently $\alpha(t_{delay})$, the angular extent in elevation that is illuminated at time t is $\alpha(t_{delay})\big|_{t-\tau} \leq \alpha \leq \alpha(t_{delay})\big|_t$. Figure 3.3 graphically illustrates the relationship between total scattered power and the plots of $S_t(\alpha)R^{-1}(\alpha)$ and $\alpha(t_{delay})$.
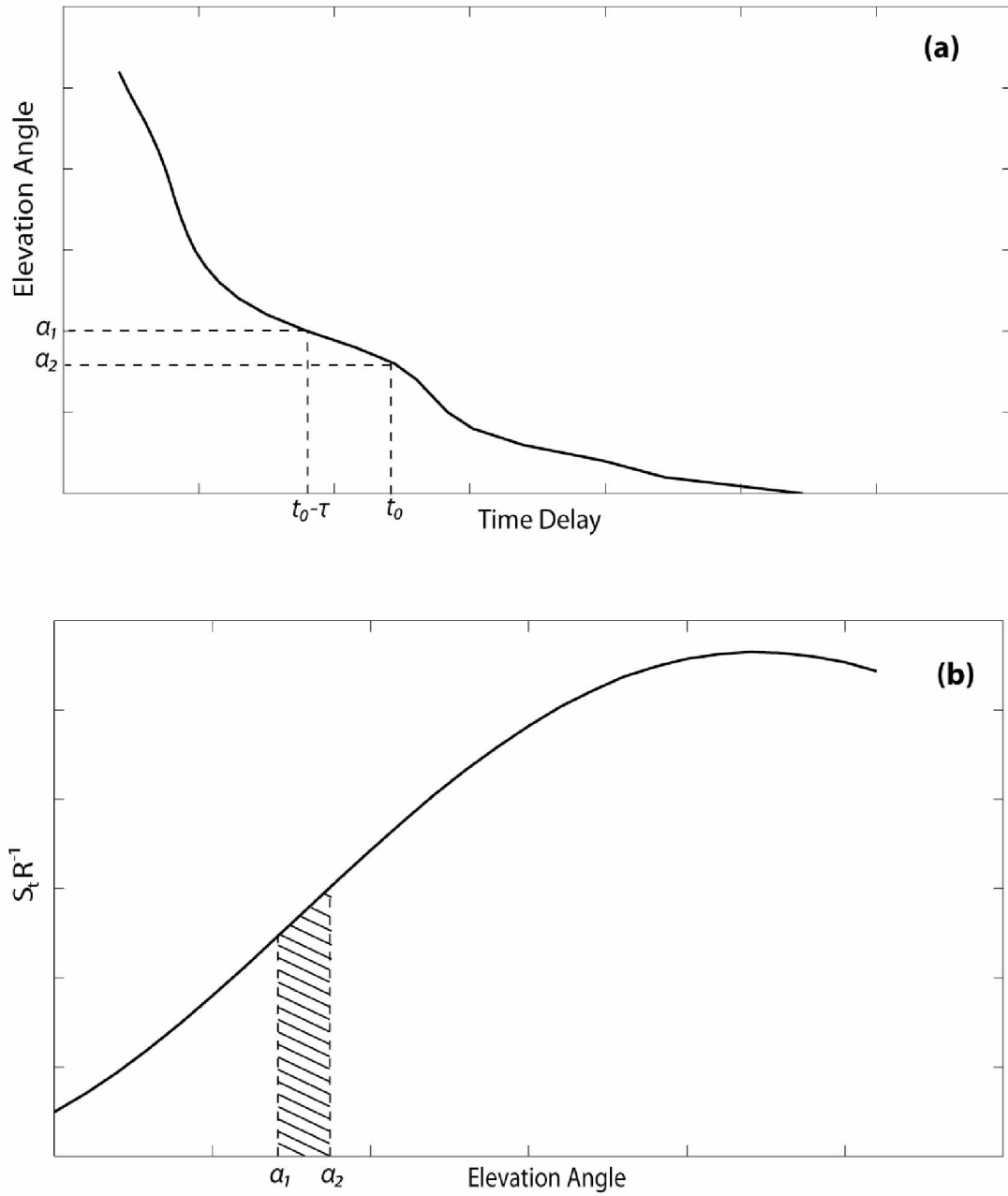
Figure 3.3: Graphical illustration of calculating scattered power in (3.3) from plots of (a) $\alpha\left(t_{delay}\right)$ and (b) $S_t(\alpha)R^{-1}(\alpha)$. Plot (a) illustrates an example of the angular extent that corresponds to the projection of a pulse on the ground at a given time. Plot (b) depicts the energy contained in the angular extent in (a) as the shaded area under the curve $S_t(\alpha)R^{-1}(\alpha)$.

Note that ionospheric focusing occurs through the spacing of the limits of integration in (3.3). In situations where $t_{delay}(\alpha)$ is not monotonic, $t_{delay}(\alpha)$ can first be divided into monotonic segments so that $\alpha(t_{delay})$ is a single-valued function and $P_s(t)$ is then the sum of the results of (3.3) for each segment.

Given the expression in (3.3) for the scattered power, the power received is found in a similar fashion. Assuming isotropic re-radiation in the upper half-plane, the distribution of scattered power per unit solid angle is a constant $S_s = P_s/2\pi$ (W/Ω). Again we assume power spreads normally in azimuth but is a function of ionospheric structure in elevation so that the power per unit length-angle in elevation is $S_s R^{-1}$ (W/(rad $\cdot$ m)). The radar presents a fixed effective area A_A (m^2) assumed to be a function of elevation angle but uniform with respect to azimuth within the beam width. Let L_φ (m) be the effective length of the antenna in the azimuth dimension so that the power per unit elevation angle is $(S_s R^{-1})(L_\varphi) = S_s R^{-1} L_\varphi$ (W/rad). The total power received may then be found by integrating over the elevation angular extent from the scattering area that subtends the illuminated length of the antenna in elevation which may be formulated as

$$P_R(t) = \int_{\alpha_1}^{\alpha_2} L_\varphi S_s R^{-1}(u) G(u)\, du = L_\varphi S_s \int_{\alpha_1}^{\alpha_2} R^{-1}(u) G(u)\, du. \quad (3.4)$$

In (3.4) we include the antenna gain pattern $G(u)$ in the integrand to account for the dependence of the antenna illuminated area on elevation angle. The effective length of the antenna in elevation is proportional to the wavelength and on the order of tens of meters in this study. An effective length on this scale size corresponds to a minute angular extent from the scattering area so that (3.4) may be approximated as

$$P_R(t) = C L_\varphi S_s R^{-1}(\alpha(t)) G(\alpha(t)) \quad (3.5)$$

where we assume that the integrand in (4) is constant over a minute angular extent C (rad). The expressions in (3.3) and (3.5) can be combined to give

$$P_R(t) = \{8\pi^2\}^{-1} P_t \varphi_B CL_\varphi R^{-1}\big(\alpha(t)\big) G\big(\alpha(t)\big) \left(\int_{\alpha_1}^{\alpha_2} \sigma^0(v) G(v) dv\right). \qquad (3.6)$$

An important note is that in the applications studied here simulation results are expressed as a signal-to-noise ratio (SNR) where the noise level is scaled to produce the best fit of simulated SNR profiles to measured SNR profiles. Therefore, the constant terms that appear in (3.6) have no bearing on the results. A comparison of the calculated received power from a smooth ionosphere given identical parameters using the alternative derivations presented in (3.1) and (3.6) is illustrated in Figure 3.4.
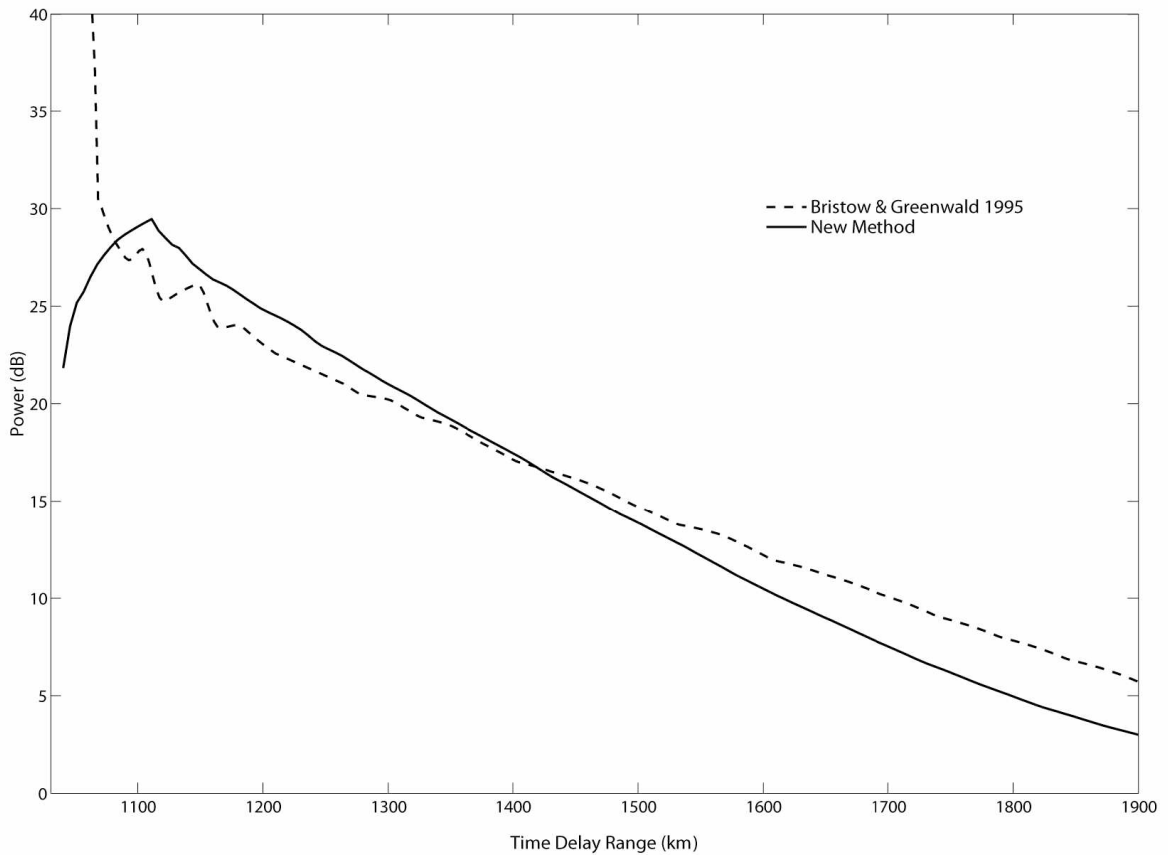
Figure 3.4: Comparison of calculated received power under identical operating parameters using *Bristow & Greenwald* [1995] derivation in (3.1) and the alternative derivation presented in (3.6).

Figure 3.4 illustrates that the new method produces a power profile that decays more rapidly than the *Bristow & Greenwald* [1995] derivation and differs near the skip distance in amplitude and trend. The *Bristow & Greenwald* [1995] derivation results in a

peak value at the skip distance range of ~1050 km with an amplitude of 55 dB that exceeds the dimensions of the graph in Figure 3.4 before monotonically decreasing. The large amplitude at the skip distance in the *Bristow & Greenwald* [1995] derivation is the result of a discontinuity in the focus factor at this range as discussed in section 3.1. The alternative derivation in (3.6) results in a power profile that increases to a local maximum at ~1100 km of 30 dB before monotonically decreasing at a slightly greater rate than given by the *Bristow & Greenwald* [1995] derivation. The smearing of the skip distance peak in the power profile given by (3.6) is the result of a convolution effect of the spatial dimensions of the transmitted pulse and the illuminated area. Near the skip distance, the illuminated area is smaller than the projection of the transmitted pulse on the ground. Equivalently, at t_0 where $(t_0 - t_{minimum}) < \tau$, the limits of integration in (3.3) are $[\alpha_1, \alpha_2]$ where $\alpha_1 = \alpha(t_{delay})\big|_{t_{minimum}}$ and $\alpha_2 = \alpha(t_{delay})\big|_{t_0}$. The effect is that the scattered power increases up until the point that the entire transmitted pulse is projected onto the ground and the limits of integration in (3.3) are governed by the pulse dimensions. A similar effect is not witnessed in the *Bristow & Greenwald* [1995] derivation because the method is derived for the case that the entire pulse is projected onto the ground. The presence of a skip distance maximum preceded by increasing power samples is consistent with measured results. The discrepancy between the trend of the power profiles given by the *Bristow & Greenwald* [1995] derivation and the method presented here are not investigated further as it will be shown in later chapters that power profiles generated using the new method produces curves that accurately approximate the trend of measured results.

3.4 Terrain Cross Section

An influential factor in the received ground scatter power is the ground cross section σ. Given that the ground is a distributed target, the ground cross section is a function of the effective scattering area and can be written as

$$\sigma = \sigma^0 A_C \tag{3.7}$$

where σ^0 (m^2/m^2) is the surface backscattering coefficient per unit area and A_c (m^2) is the effective scattering area [*Peebles*, 1998]. In general, σ^0 is a function of angle of incidence, polarization, frequency, roughness, and permittivity at the scattering point [*Moore*, 2008]. Although various theoretical approximations of σ^0 have been derived, the complicated nature of the scattering coefficient lends itself to an experimental approach where distributions of σ^0 are measured and used to derive empirical models. Empirical models of σ^0 for various terrain classes, polarization, and frequency are provided by *Moore et al.* [1980], *Nathanson et al.* [1991], and *Ulaby* [1980]. Figure 3.5 illustrates a comparison of empirical models of σ^0 as a function of incidence angle for similar parameters given by the aforementioned authors.
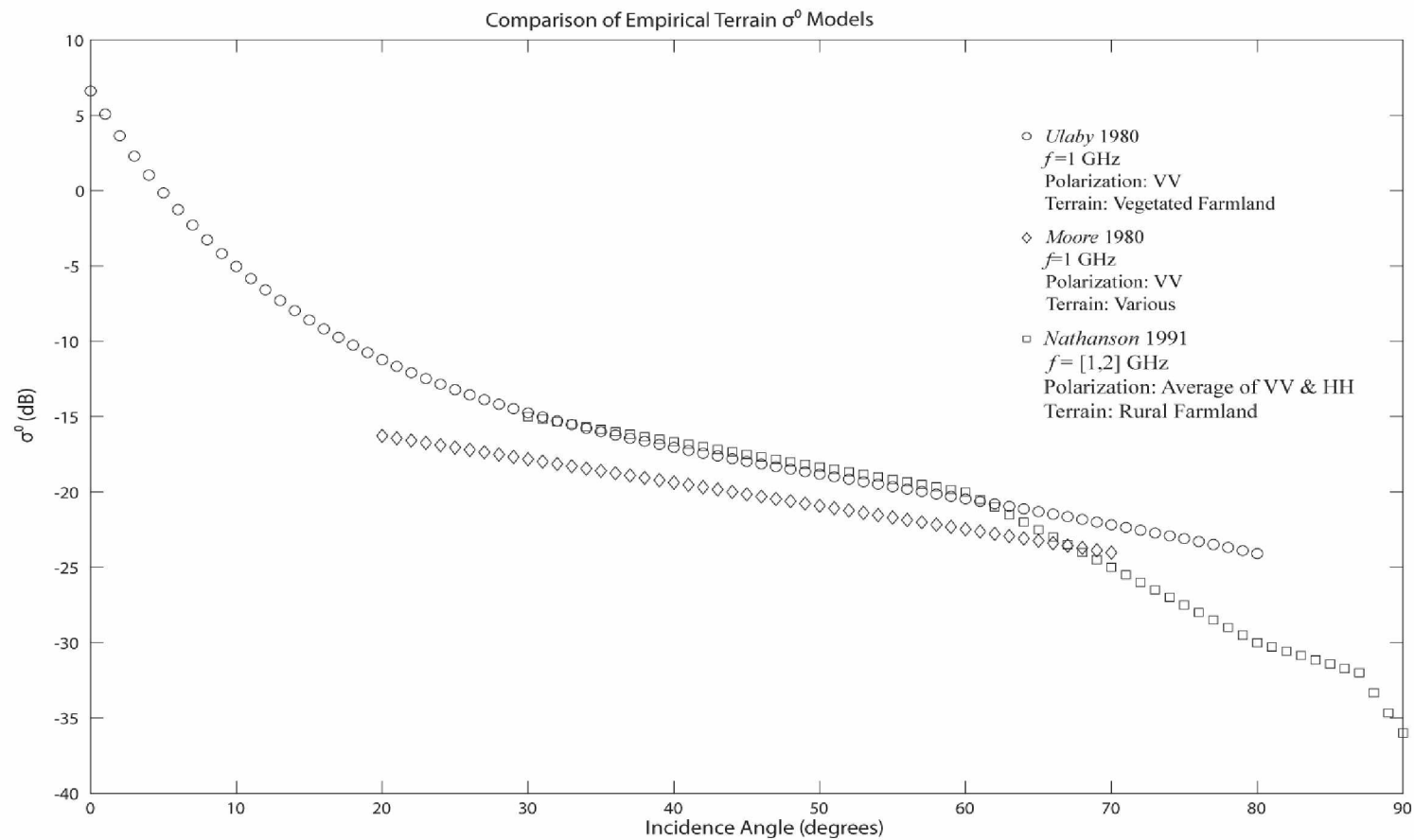
Figure 3.5: Empirical curves of σ^0 as a function of angle of incidence using models presented by *Moore et al.* [1980], *Nathanson et al.* [1991], and *Ulaby* [1980].

3.4.1 Modeling Terrain Cross Section

Several methods of estimating and incorporating a terrain cross section into the simulation of the ground scatter return profile were investigated with the goal of isolating power enhancements due to ionospheric phenomena from those due to variations in σ^0.

Ground cross section estimates based on empirically fitted curves for $\bar{\sigma}^0(\theta, f)$ given by *Ulaby* [1980] and *Nathanson et al.*[1991] were both implemented. The empirically fitted curve for $\bar{\sigma}^0(\theta, f)$ provided by *Ulaby* [1980] is valid for $\theta \in [0,80]$ degrees and $f \in [1,18]$ GHz and the empirically fitted curve provided by *Nathanson et al.* [1991] is valid for $\theta \in [30,90]$ degrees and $f \in [1,2]$ GHz. However, lacking an empirical model of $\bar{\sigma}^0(\theta, f)$ for HF-band, the curve of $\bar{\sigma}^0(\theta, 1 \text{ GHz})$ from both models was used for calculations. In addition, we note that the results obtained using these empirical models are crude because the models are based on scatter from vegetation and/or rural farmland which are significantly different than Alaskan terrain. The value of incidence angle θ with respect to the surface normal was calculated from ray tracing parameters for both a smooth, spherical earth and also from a terrain profile generated with digital elevation model (DEM) data. The DEM data used in analysis was taken at a 3-arc second (~100 m) resolution along the bore-sight of the radar. Given a terrain profile, the surface normal can be calculated using the geometry depicted in Figure 3.6 (a) and equations (3.8)-(3.12).

$$a = R_{Earth} + h1 \tag{3.8}$$

$$b = R_{Earth} + h2 \tag{3.9}$$

$$c = \sqrt{a^2 + b^2 - 2ab\cos\varphi} \tag{3.10}$$

$$\gamma = \sin^{-1}\left(\frac{a}{c}\sin\varphi\right) \tag{3.11}$$

$$\theta = \pi - (\gamma + \frac{\pi}{2}) \tag{3.12}$$

Note that the surface backscattering coefficient as defined in (3.7) is given per unit area. However, in this application the total scattered power is found by integrating over an angular extent as depicted in (3.3) and (3.4). Conversion of σ^0 to units of per radian is achieved by multiplying the backscattering coefficient by the area per unit elevation

angle. Considering the geometry of Figure 3.6 (b), the illuminated area can be expressed in terms of elevation angle as

$$A = (R\varphi_B)X = (R\varphi_B)(R\Delta\alpha\{\sin(\alpha)\}^{-1}), \tag{3.13}$$

so that the surface backscattering coefficient per unit radian is

$$\sigma_\alpha^0 = A\sigma^0 = (R\varphi_B)(R(1)\{\sin(\alpha)\}^{-1})\sigma^0 = \sigma^0 R^2 \varphi_B \{\sin(\alpha)\}^{-1}. \tag{3.14}$$
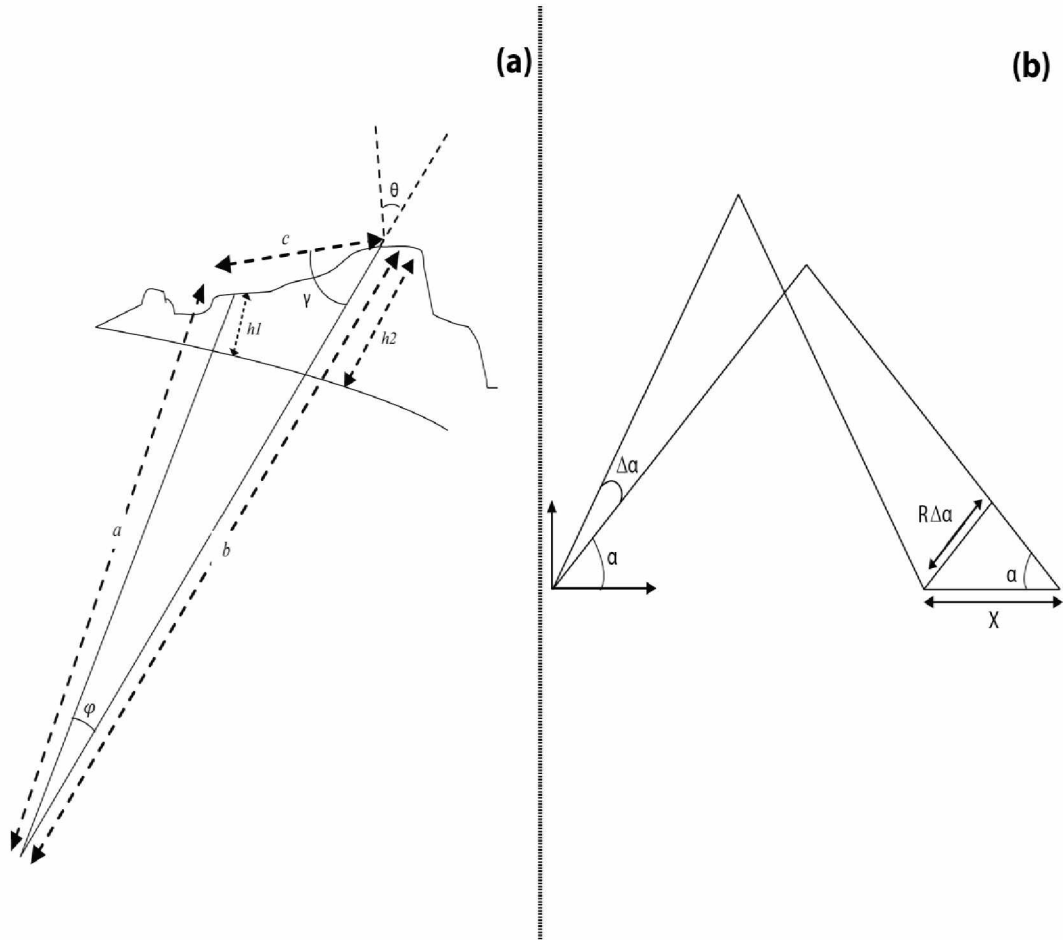
Figure 3.6: Illustration of geometry pertinent to modeling terrain cross section. (a) illustrates the geometry of surface normal angle calculation from DEM data necessary to determine angle of incidence related by equations (3.8)-(3.12). (b) illustrates geometry relating elevation angle to distance along the ground necessary for conversion of σ^0 to units of per radian in equations (3.13)-(3.14).

Chapter 4   Characterizing Artificial Layers[1]

4.1 Introduction

HF ionospheric heating experiments at HAARP appear to produce bottom-side plasma density enhancements. The signature associated with the enhancement is the formation of an optical ring that results from the excitation of electrons at energy levels consistent with ionization production [*Pedersen et al.*, 2009]. The results of ray tracing illustrate that modeling the artificial bottom-side density layer as a density perturbation Gaussian distributed in the horizontal and vertical directions results in the deflection of rays into a ring structure consistent with optical observations during heating experiments [*Pedersen et al.*, 2009].

Independent observations of the production of artificial density layers at the HAARP station located in Gakona, Alaska were sought from the ground scatter return measured by the Kodiak, Alaska SuperDARN. The Kodiak SuperDARN is uniquely located to observe density perturbations due to its field of view with respect to the Gakona HAARP station as illustrated in Figure 4.1 and has been used in previous studies to analyze the time scales of irregularities produced by heating experiments [*Kendall et al.*, 2010]. The potential effects of an artificial density layer on received ground scatter at the Kodiak SuperDARN were investigated through ray tracing by inserting a model artificial layer into the density profile and using the resultant ray path lengths and time delays to calculate from (3.6) the expected ground scatter return. The expected ground scatter return was then compared to the observed ground scatter return during a period of time when high-power HF heating experiments were performed.
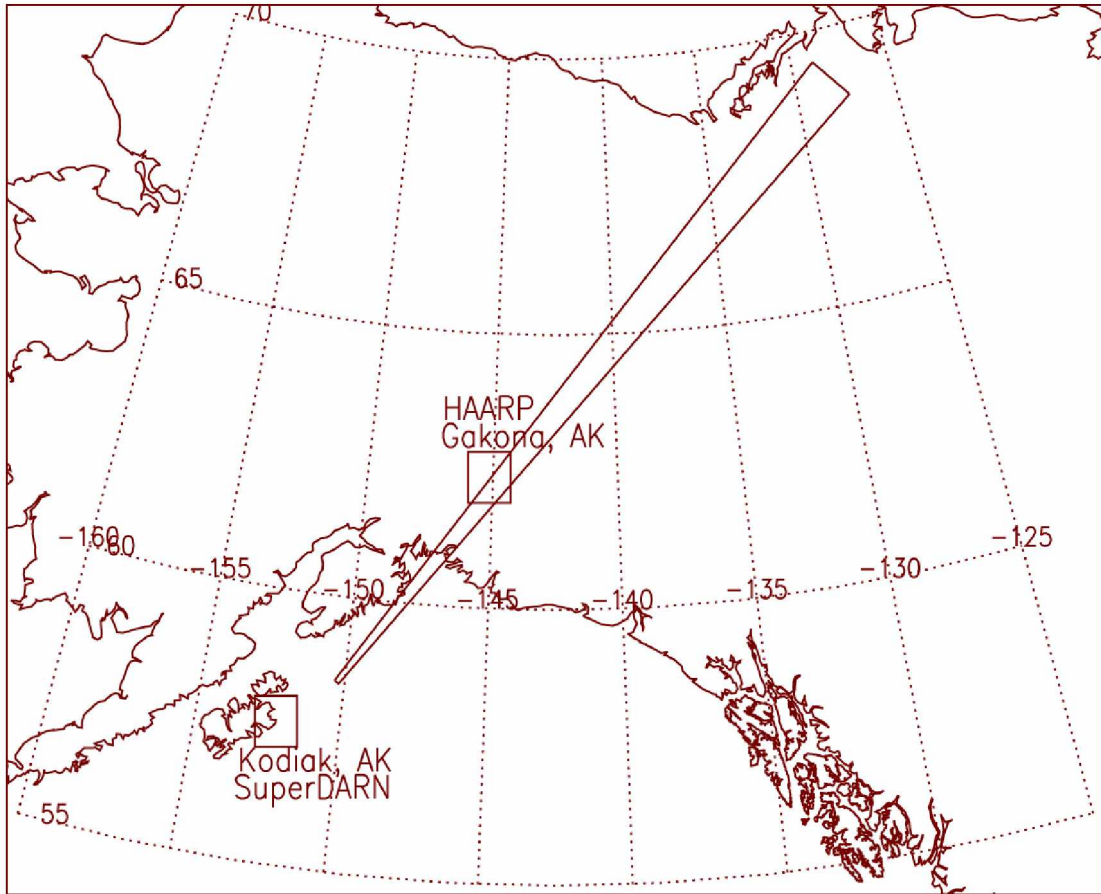
Figure 4.1: Map of the location of the Gakona, HAARP station with respect to the field of view in beam direction 9 of the Kodiak SuperDARN.

4.2   Measurement Interval

One period that high-power HF heating experiments were conducted with the potential to produce artificial layers was 18 November 2009 between 01:17-01:34 UT. An RTI plot of the return power observed by the Kodiak SuperDARN during this interval is illustrated in Figure 4.2.
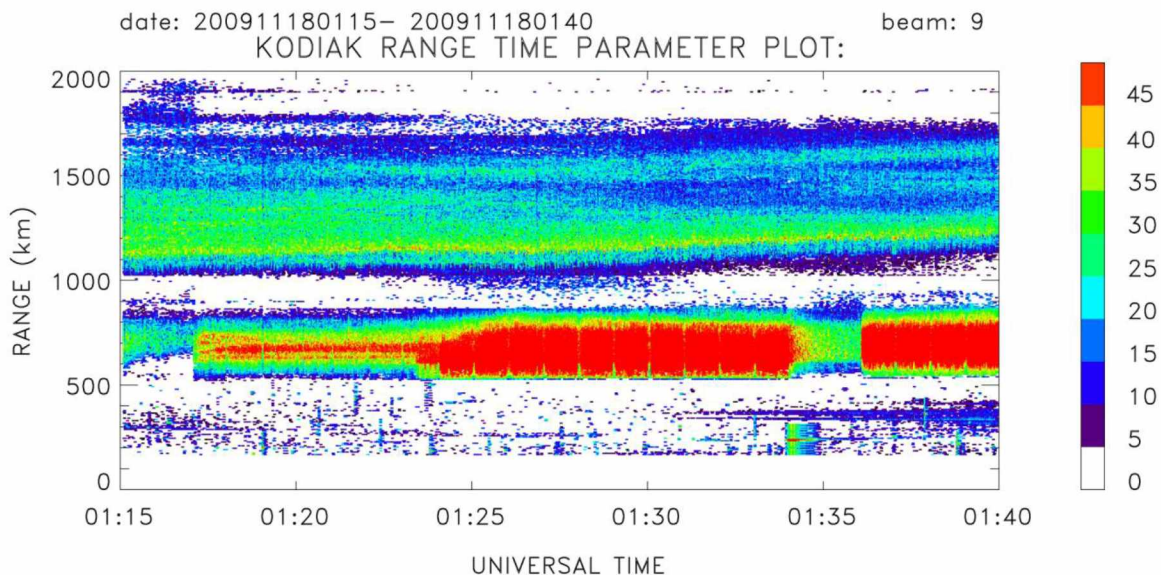
Figure 4.2: RTI plot of return power observed by Kodiak SuperDARN on 18 November 2009 between 01:15-01:40 UT.

During the interval 01:17-01:34 UT, HAARP was operated at 2.92 MHz with O-mode polarization at a power of ~440 MW ERP, which is consistent with test conditions under which artificial layers had been generated previously [*Pedersen et al.*, 2010]. In Figure 4.2, the high-power back scatter observed in the range [500,800] km is an indicator of high-power HF heating and results from specular reflection from plasma irregularities in regions of instability. Note that the back scatter power present from [1100,1800] km can be divided into two regions, the first with a skip distance in the range [1100,1200] km and the second with a skip distance between [1500,1600] km in range. Ionograms measured during the period 1:15-1:35 UT demonstrate that the background ionosphere is composed of distinctive E and F layers. The results of a ray tracing simulation based on measured ionogram characteristics is illustrated in Figure 4.3.
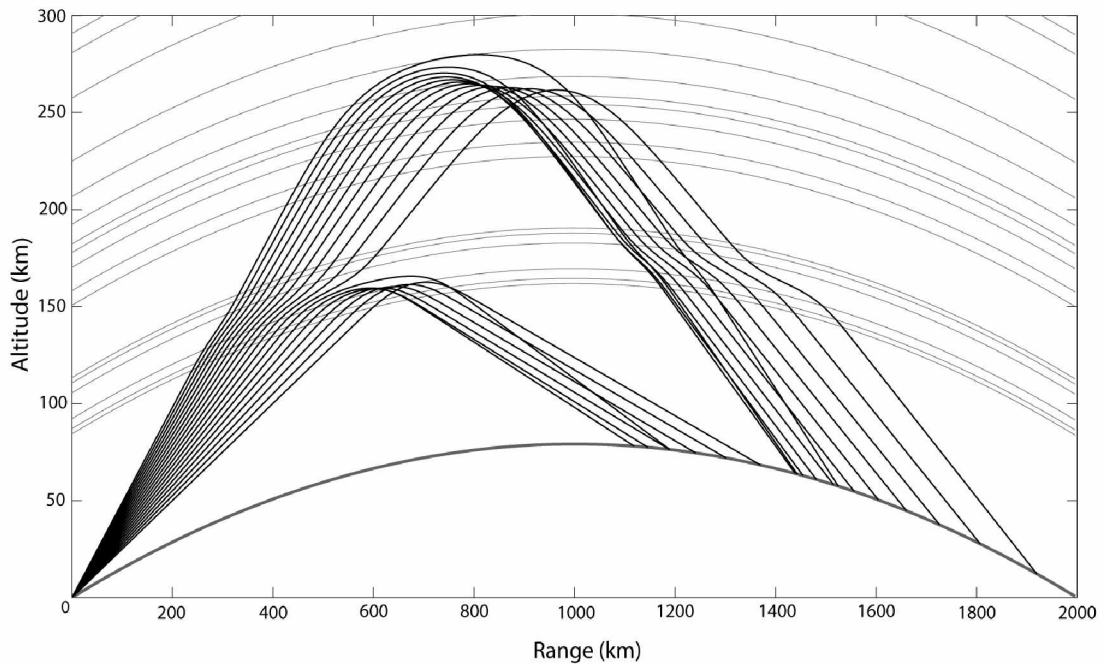
Figure 4.3: Ray path plot given ionospheric profile based on UT 01:17-01:34 ionosondes at HAARP on 18 November 2009. The ray path plot indicates that the ground-scattered power is divided into two distinct regions which is supported by the structure of the RTI plot in Figure 7.

Note that the ray path plot in Figure 4.3 clearly depicts two distinct regions of ground scatter return from E-region deflected rays at low elevation angles and from F-region deflected rays at higher elevation angles, which supports the structure of the RTI plot in Figure 4.2. Researchers have postulated that artificial density layers form when the transmit frequency, f_T, matches the upper-hybrid frequency, f_{uh}, and/or multiples of the electron gyro frequency, f_{ce} [*Pedersen et al.*, 2010]. These characteristic plasma frequencies correspond to electron densities obtained in the F-region during the time period in question and consequently the simulation results will be limited to calculating the expected ground scatter return due to rays deflected from the F-region.

A comparison of the F-region simulated ground scatter return with the measured return power during the interval UT 01:32:34-01:32:35 on 18 November 2009 is illustrated in Figure 4.4.
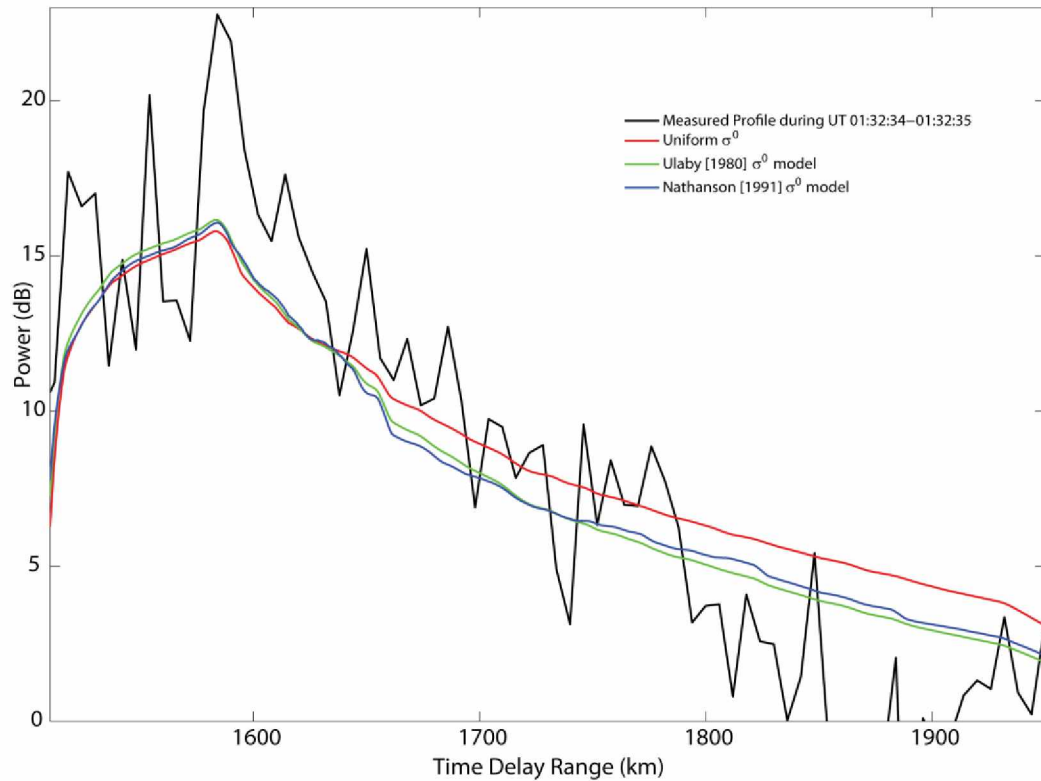
Figure 4.4: Comparison of F-region simulated ground scatter return using various terrain cross section models with the measured return during UT 01:32:34-01:32:35 on 18 November 2009. Note that the noise level of the simulation results was set such the the simulated profiles matched the mean of the measured profile.

Note from Figure 4.4 that the measured profile features very large fluctuations in power between range bins. Furthermore, a comparison of consecutive integration intervals also demonstrates that there is a large variation in power at the same range bin over time. Despite the large natural fluctuations in the measured profile in Figure 4.4, note that the simulated ground-scattered power profiles accurately approximates the skip distance location and the trend of the mean of the measured profile regardless of terrain cross section model implemented. It will be illustrated that the observed ground-scattered power over the time interval that was studied had a standard deviation of approximately 4 dB at all time delay ranges. Due to the large variance in the measured return power and the comparatively small difference between the simulated results using either the

Nathanson [1991] or *Ulaby* [1980] ground cross section models instead of a uniform ground cross section, a uniform ground cross section will be assumed for all results presented here.

4.3   Artificial Layer Model

Given a brief comparison of the simulated and measured ground-scattered power as a function of range due to the background density profile, the effects of a model artificial layer on the simulated ground-scattered power can be investigated. Figure 4.5 illustrates an ionogram from 18 November 2009 at UT 01:26:40 that illustrates an artificial density layer in addition to the background density profile.
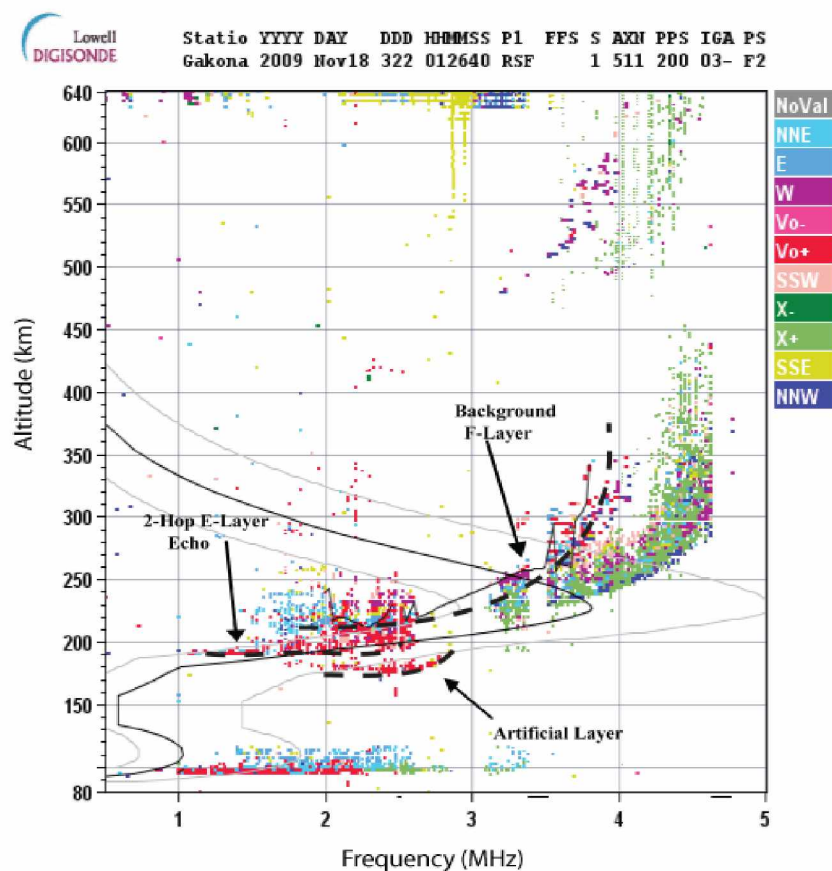
Figure 4.5: Ionogram at UT 01:26:40 on 18 November 2009 illustrating an artificial density layer in addition to background profile. Ionogram publicly available from the HAARP webserver at http://www.haarp.alaska.edu.

The artificial density layer present in Figure 4.5 was simulated in ray tracing by inserting a perturbation in the density profile grid. The perturbation was Gaussian distributed in horizontal and vertical directions. The peak density, peak density altitude, and half-widths in the horizontal and vertical directions were all free parameters. In order to maintain consistency with previously published results, the horizontal and vertical half-widths were chosen to be 30 km and 8 km respectively [*Pedersen et al.*, 2009]. The peak density was estimated from ionograms to be in the range 2.5-3.0 MHz. Note from Figure 4.6 (a) that a model artificial density layer produces a power reduction region with a width of 60-100 km followed by a smaller amplitude power enhancement region with a width of 80-120 km. The width of the power reduction and enhancement regions increases as the artificial layer descends in altitude because lower elevation angle rays subtend a larger time delay region than the same angular extent at higher elevation angles.

Before comparing simulation results to the measured data, the format of the measured data must be considered. In this study, the measured data from the Kodiak SuperDARN was analyzed in *fitted* form. Fitted data consists of the measured return signal from a number of transmit sequences averaged over an integration interval. The fact that the return signal is being averaged over a period of time has practical implications. Optical observations during high-power HF heating experiments demonstrate that after artificial density layers form, the layers rapidly descend at rates up to 0.26 km/s until reaching an altitude of ~150 km where recombination processes exceed ionization production and the density perturbation dissipates [*Petersen et al.*, 2010]. The effect of integration can be approximated in the simulated ground-scattered power results by averaging the ground-scattered power profiles calculated with the density perturbation vertically displaced by the product of the rate that the density layer descends and the length of the integration interval. The effect of the vertical displacement of an artificial layer over an integration interval on the simulated ground-scattered power profile is illustrated in Figure 4.6 (b). Figure 4.6 (b) illustrates that the simulated profiles

generated with the artificial layer displaced by 0.25 km in altitude differ by fractions of a decibel. As the effect of averaging produces a negligible change in the ground-scattered power profile compared to natural fluctuations, it will be ignored in all results presented here.
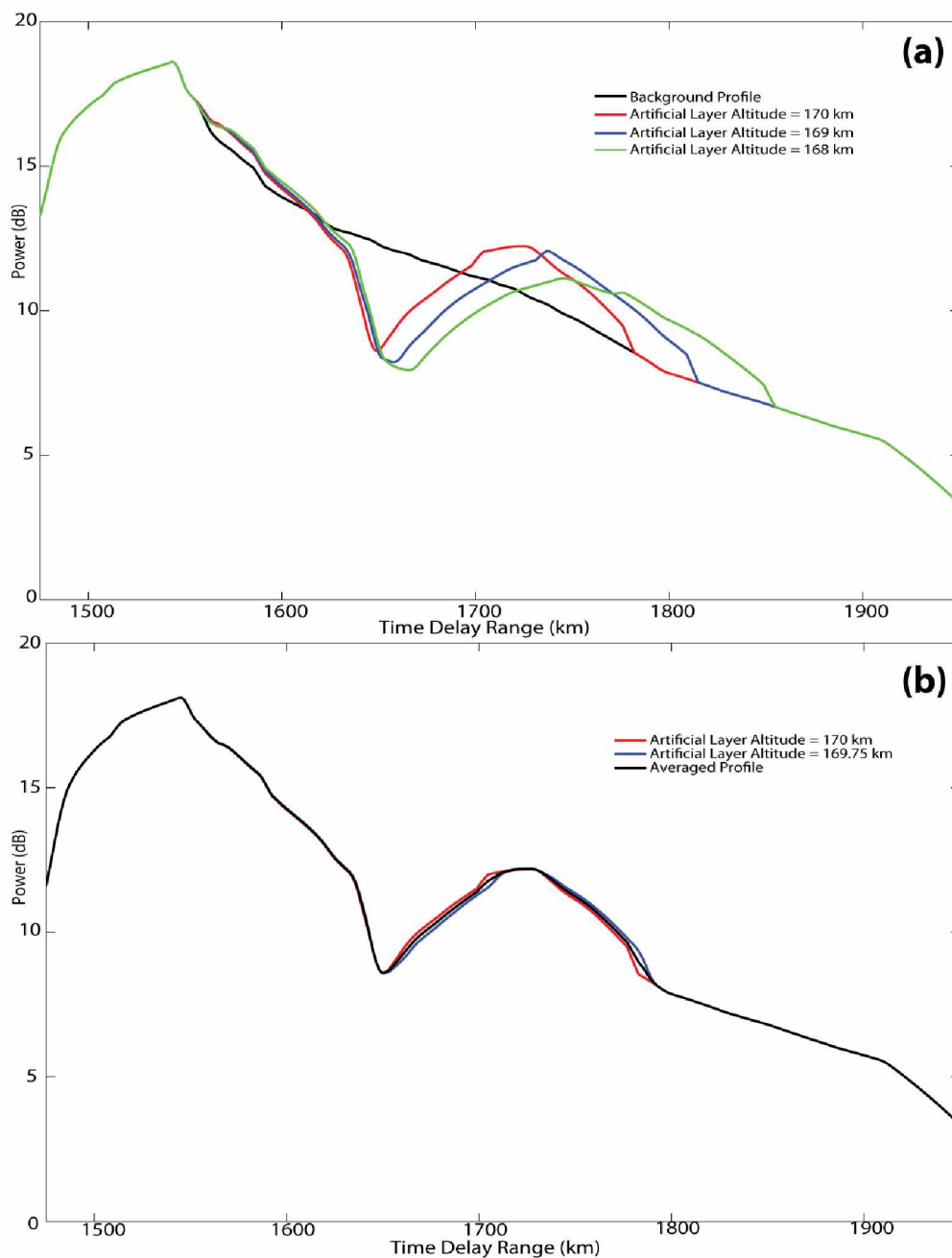
Figure 4.6: Plots illustrating the effects of artificial layer altitude and vertical displacement on simulated ground-scattered power profiles. (a) provides a comparison of simulated ground-scattered power as a function of range including model artificial layers at various altitudes. (b) illustrates a comparison of ground-scattered power as a function of range given a model artificial density layer at altitudes displaced by the product of the estimated layer velocity and the integration interval of the Kodiak radar. The averaged profile depicted in (b) provides an estimate of the effect that the artificial layer vertical movement has on the measured ground-scattered power during an integration interval.

4.4   Measurement Ambiguity

Given a description of the effects of a model artificial density layer on the simulated ground-scattered power, the measured data was examined for power reductions that may be due to focusing by an artificial layer. A challenge faced in determining possible power reductions due to focusing by an artificial layer was the natural temporal distribution of received ground-scattered power. For example, Figure 4.7 illustrates the mean and standard deviation of back scattered power as a function of range on 18 November 2009 during the interval UT 01:20:00-01:25:00, which is during the period HAARP was heating but prior to any evidence of artificial layers in ionograms. In Figure 4.7, the mean and standard deviation in the range [1600, 1800] km where focusing from an artificial layer might be expected to create power enhancements is approximately 7 dB and 4 dB respectively. Application of Chebyshev's inequality with these parameters then implies that one could expect received power levels anywhere between 1-13 dB 56% of the time at these ranges, which demonstrates the ambiguity in discerning a power enhancement rather than a natural fluctuation.
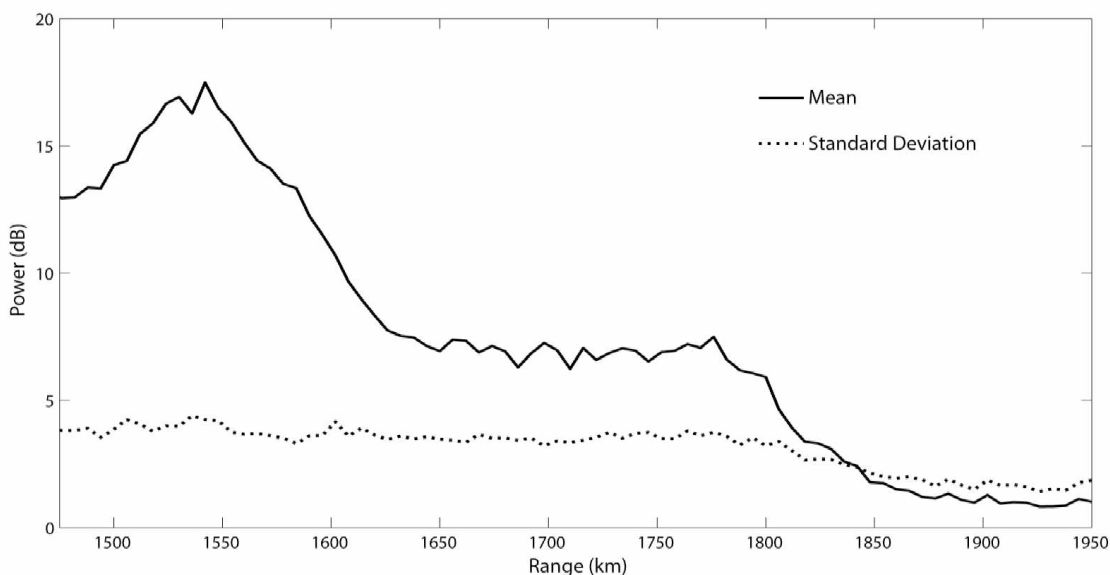
Figure 4.7: Mean and standard deviation of return power observed by Kodiak SuperDARN on 18 November 2009 during the time interval UT 01:20-01:25.

4.5   Results

Despite the difficulties mentioned, several measured profiles were identified that contained possible power reductions due to focusing by an artificial layer. Simulated profiles were generated to re-create the power reductions observed in these measured profiles. A model artificial layer was included in the density profile and the parameters of the artificial layer were varied in an attempt to fit the resultant simulated profile to the mean of the measured profile. A comparison of the simulated profiles with and without a model artificial layer and the measured profile during the integration interval at UT 01:26:58 is depicted in Figure 4.8.
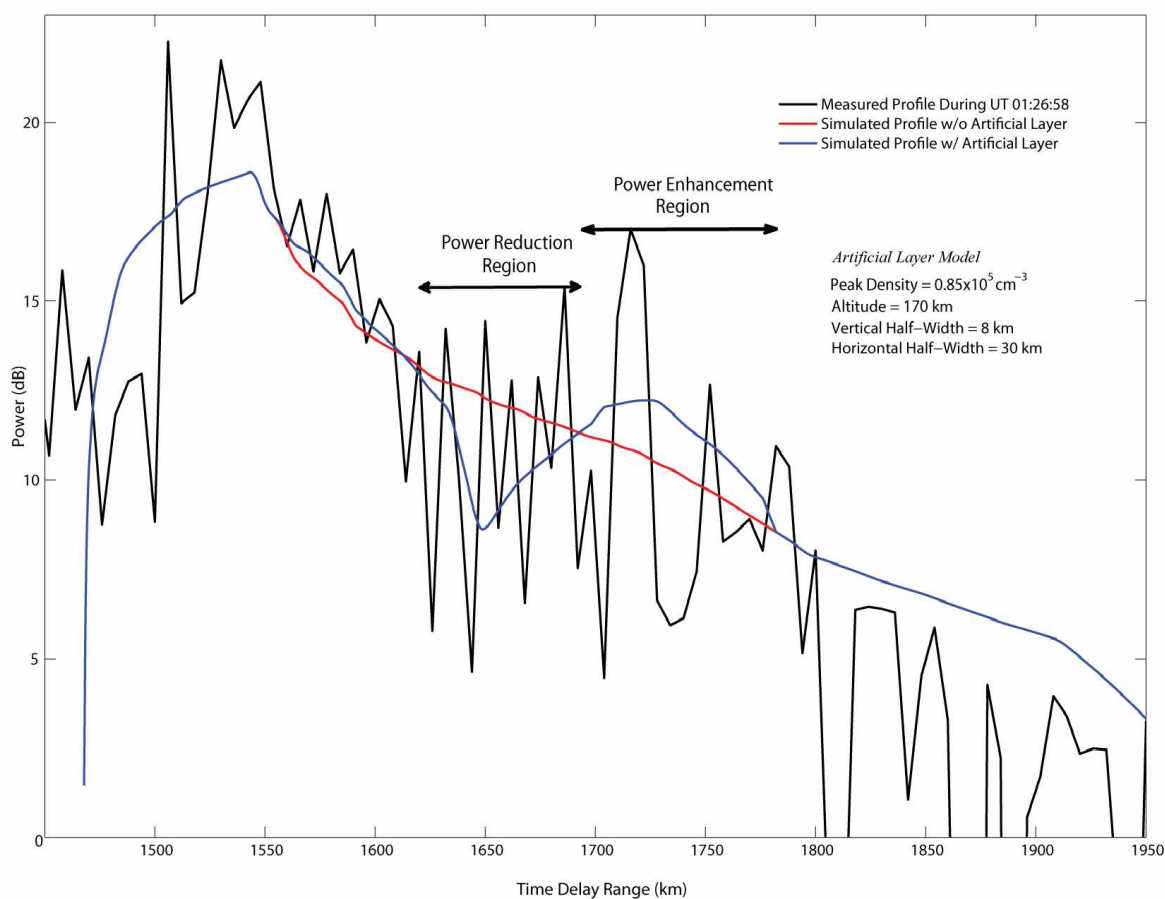
Figure 4.8: Comparison of Kodiak SuperDARN observed return power during 18 November 2009 during UT 01:26:58 integration interval with simulated ground-scattered power profiles generated with and without model artificial layers.

Note in Figure 4.8 that both simulated profiles accurately approximate the location of the skip distance maximum and the trend of the mean of the measured profile outside of the regions annotated as power reduction or enhancement regions. At ranges between [1620, 1700] km corresponding to the artificial layer induced power reduction region, the simulated profile generated without a model artificial layer overestimates the mean of the measured profile whereas the simulated profile generated with a model artificial layer approximates the mean of the measured profile. Similarly, at ranges between [1700, 1780] km corresponding to the power enhancement region, the simulated profile without a model artificial layer underestimates the mean of the measured profile whereas the simulated profile generated with a model of the artificial layer approximates the mean of the measured profile. Given the similarity between the simulated profile including a model artificial layer and the measured profile, an estimate of the actual dimensions and location of the artificial layer is provided by the model parameters listed in Figure 4.8.

Some discrepancy between the location, width, and amplitude of the simulated and observed power reductions is due to the oversimplification of the artificial density layer model. While the evolution of the artificial density layer in altitude has been discussed and found to be negligible, the spatial evolution of the density perturbation has been neglected. Optical observations during HF heating experiments illustrate that the interior of an artificial density layer is highly structured [*Pedersen et al.*, 2010]. Specifically, the interior of an artificial density layer contains field-aligned filaments that evolve over the lifetime of the artificial density layer [*Pedersen et al.*, 2010].

4.6   Conclusions

In this chapter, the estimated ground-scattered power profile generated using a simple model of an artificial layer was compared to the measured return power profile during a time interval where an artificial layer was present in ionograms. It was found that a simple model of the artificial layer could be used to generate a simulated ground-

scattered power profile that contained a power reduction of the appropriate width and location as the power reduction observed in the measured data.

However, a number of challenges presented ambiguity in the results. Foremost, it was found that the observed return power naturally fluctuates over a wide range of values, which limits the ability to discern enhancements. Future work might include quantifying the natural variation in ground-scattered power through a Monte Carlo approach of varying the ionospheric density in a random fashion and observing the resulting spread of simulated ground-scattered power. In addition, the model of the artificial density layer used in simulations is an oversimplification that does not account for the evolution of the artificial layer density and structure. Although some encouraging simulation results have been illustrated, the combination of these factors make the identification of power enhancements in ground-scattered power return due to artificial layers a challenging task.

Chapter 5   Statistical Properties of Oblique HF Ground Scatter[1]

5.1 Introduction

HF radar ground scatter measurements made by the SuperDARN radar located in Kodiak, AK exhibit fluctuations in power over short periods of time in which the average ionospheric conditions appear to be static. To illustrate, Figure 5.1 (a) depicts the range-time-intensity (RTI) plot of signal-to-noise ratio (SNR) in beam direction 9 on 16 October 2009 between UT 00:25:00-00:40:00 and Figure 5.1 (b) illustrates a time series of 816 samples taken from a range bin in the skip distance region. Although the RTI plot in Figure 5.1 (a) illustrates that the ground-scattered power appears to be relatively uniform over the time interval, the corresponding time-series plot of observed SNR at a particular range bin in Figure 5.1 (b) has a sample standard deviation of more than five decibels. The sample mean in Figure 5.1 (b) is 28.4 dB above the estimated noise level which indicates that the fluctuations in observed power are not simply the result of noise, but rather the result of some fluctuation of the target or of the index of refraction along the propagation path from the radar to the ground scatter location and back. Since the fluctuations of the ground scatter cross section at HF are expected to be small, we assume the observed fluctuations are due to the latter effect.

(a)

(b)
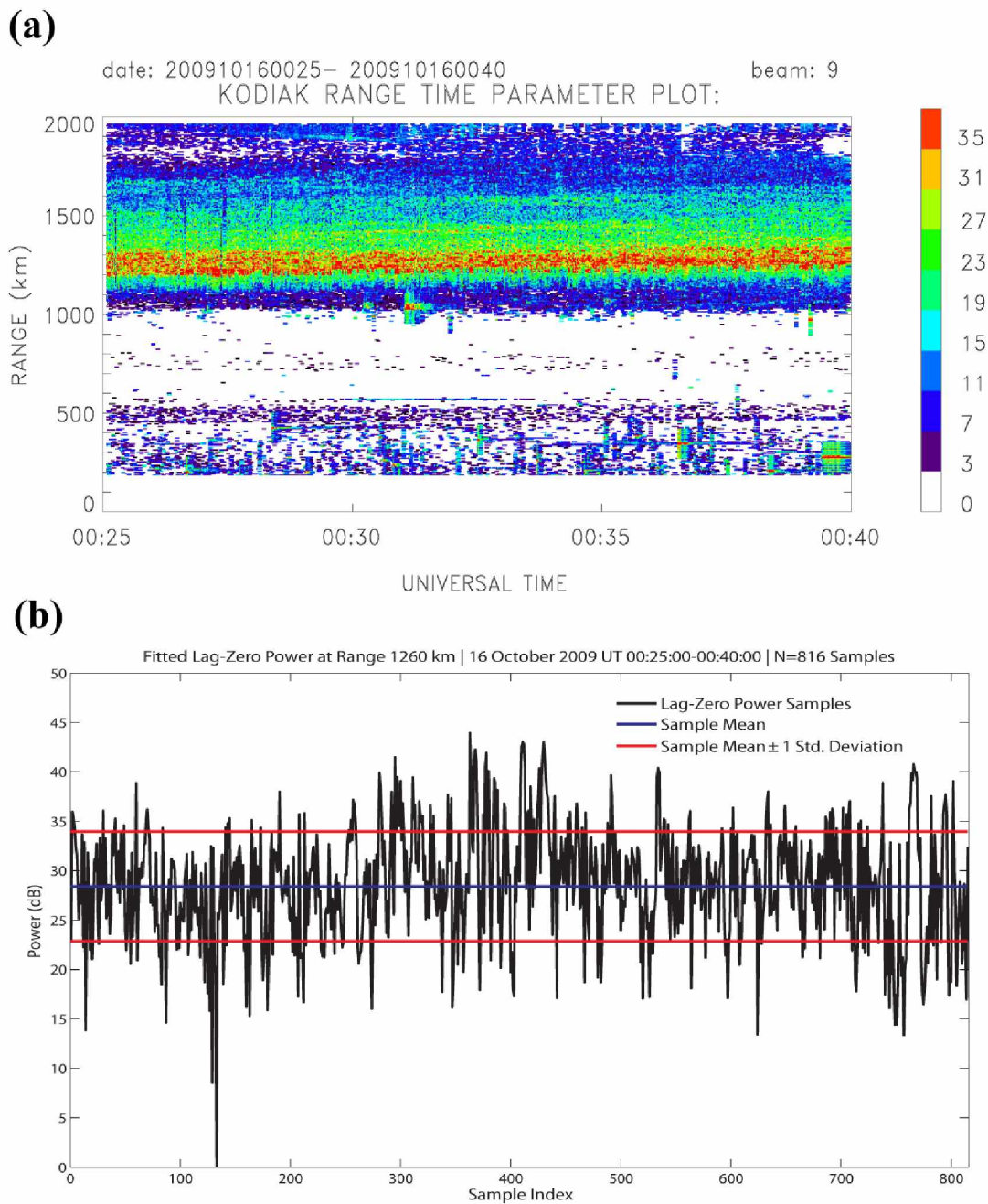
Figure 5.1: (a) depicts an RTI plot of lag-zero power measured in beam direction nine at Kodiak on 16 October 2009 UT 00:25:00-00:40:00 while (b) depicts the time-series of observed power at a range of 1260 km along with sample mean and standard deviation levels. Time-series samples in (b) are spaced by the integration period of 1 second.

In this study, a Monte-Carlo approach to quantifying observed distributions of ground-scattered power has been investigated using ray-tracing techniques. Four influential random processes were considered in modeling the expected distribution of ground-scattered power. These processes include a time-variant propagation path due to random electron density fluctuations, random signal polarization, noise, and data processing. Using the numerical technique of estimating ground-scattered power from ray tracing results presented in Chapter 3, simulated distributions of ground-scattered power were generated for randomly perturbed ionospheric conditions. Subsequently, the effects of a random signal polarization, noise, and data averaging were modeled as transformations of the probability density function (PDF) obtained from considering a time-variant propagation path. Sample estimates of the mean and standard deviation obtained from simulation and from measured distributions are compared to analyze the validity of the models and obtain an estimate of electron density fluctuations in the ionosphere. An accurate characterization of the expected ground-scatter distribution has important applications for any HF radar work involving target discrimination.

5.2 Simulation Models

The objective of this study was to re-create the ground-scattered power distributions observed by the Kodiak SuperDARN radar. At a given range bin, the distribution of ground-scattered power observed over a short interval of time is a function of several random processes including propagation path, signal polarization, noise, and data processing. A discussion of how each of these random processes is modeled in simulation follows.

5.2.1 Electron Density Perturbations

Perturbations in electron density correspond to perturbations in the group refractive index seen by a radar pulse as it traverses the ionosphere. The perturbations in group refractive index create focusing effects that either enhance or diminish the received power. Therefore, the amount of ground-scattered power observed by a radar at a given sample time during two different measurement intervals will vary if the background electron density is perturbed between measurement intervals. Consequently, a randomly fluctuating ionospheric density profile will produce a distribution of observed ground-scattered power.

In this study, ray tracing was performed using software that numerically integrates the equations of Hamiltonian optics over a two dimensional grid. A randomly fluctuating ionosphere was modeled by perturbing the background electron density profile grid used by the ray tracing software. Assuming that electron density perturbations occur perpendicular to the local magnetic field and considering the high latitude location of the Kodiak radar, perturbations in simulation were restricted to the horizontal direction. Specifically, the two dimensional density grid was assumed to be composed of M columns and the background density profile of each column was perturbed by the factor $(1 + \varepsilon)$ where M values of ε were drawn from a random distribution. Figure 5.2 illustrates a ray path plot where the background density profile has been perturbed given

column widths of 5 km and values of ε drawn from a zero mean Gaussian distribution with a standard deviation of 5%, $\aleph(0,5\%)$.
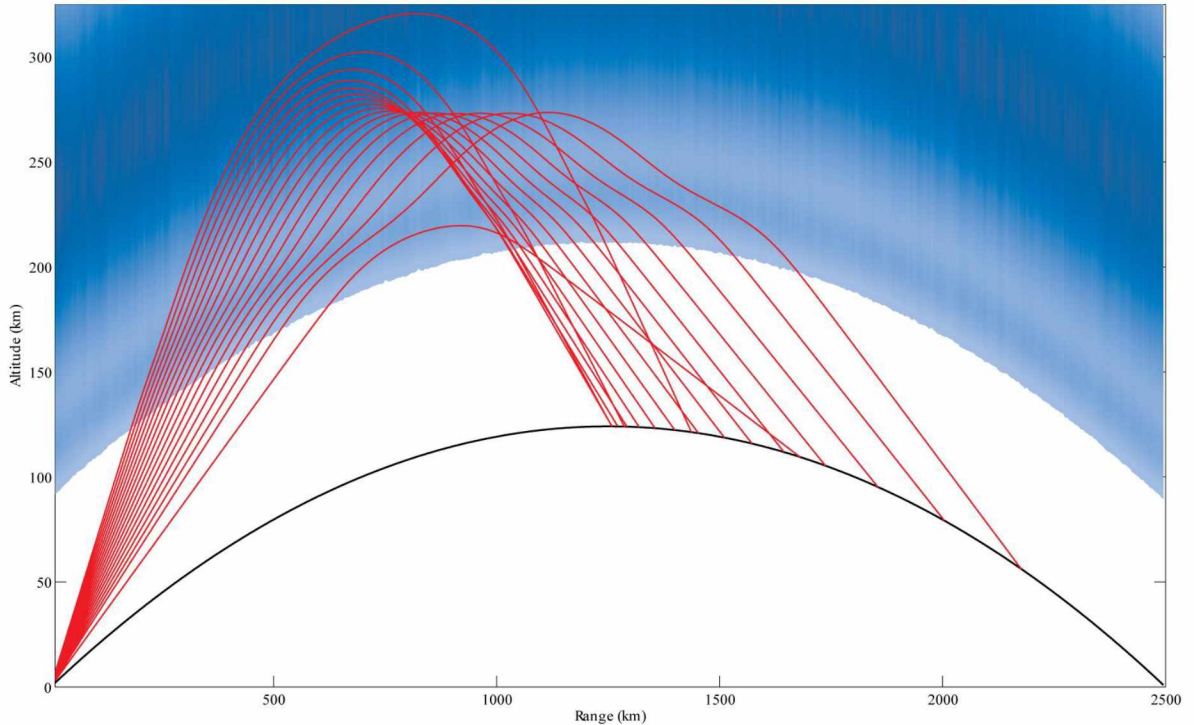
Figure 5.2: A ray path plot illustrating a randomly perturbed ionospheric density profile. The amplitude of the perturbations is $(1 + \varepsilon)$ times the background density where ε is distributed according to $\aleph(0,5\%)$. The perturbations widths are 5 km in the horizontal direction.

Ground-scattered power is estimated from ray tracing results using the technique described in Chapter 3. The process of randomly perturbing the background electron density and calculating a resultant ground-scattered power profile was repeated N times to generate a distribution of ground-scattered power at each time delay range where observations are made. Unless otherwise mentioned, $N = 10^4$ trials are performed for a given set of perturbation parameters in this study.

5.2.2 Random Polarization

The ionosphere is a birefringent medium where phase velocity depends on polarization. The difference in phase velocities for ordinary and extraordinary polarizations in the ionosphere result in a phenomenon termed Faraday rotation. When a linearly polarized signal propagates through the ionosphere the direction of polarization will rotate through an angle θ given by

$$\theta = \frac{1}{2}k(P_O - P_X) \qquad (5.1)$$

where k is the free space propagation constant and $P_{O/X}$ are the phase paths for the ordinary and extraordinary modes [*Budden*, 1988]. Due to Faraday rotation, the signal that is incident on the ground after propagation through the ionosphere will have components in both the vertical and horizontal polarizations so that we may assume the back-scattered signal also contains components in both polarizations. Here we model the received signal at the antenna as the sum of two transverse components that are rotated from a reference plane by the Faraday rotation angle θ as illustrated in Figure 5.3.
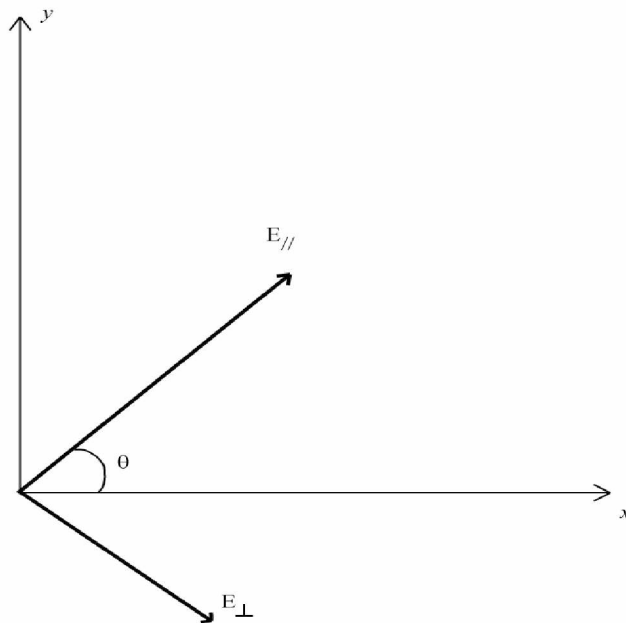
Figure 5.3: Geometry relating the incident backscattered signal to the reference frame. The angular rotation θ between the received signal polarization axes and the reference frame is assumed to be due to Faraday rotation.

The general expression for the total field incident at the antenna is

$$E_t = E_{//}\cos(\omega t) + E_{\perp}\cos(\omega t + \varphi) \tag{5.2}$$

where any signal polarization may be formed by appropriately modifying the transverse field amplitudes $E_{//}$ / $E_{\perp}$ and the relative phase shift φ between these components. If we assume the antenna is linearly polarized along the x-axis, the field seen by the antenna is the projection of the total electric field onto the antenna, which is

$$E_x = E_{//}\cos\theta\cos(\omega t) + E_{\perp}\sin\theta\cos(\omega t + \varphi). \tag{5.3}$$

The ratio of time-average power received over incident power may be expressed as

$$P(\theta,\rho,\varphi) = \frac{\langle E_x^2 \rangle}{\langle E_t^2 \rangle} = \frac{\cos^2\theta + \rho^2\sin^2\theta + 2\rho\cos\theta\sin\theta\cos(\varphi)}{1+\rho^2} \tag{5.4}$$

where the variable ρ is the ratio of transverse field amplitudes $\rho = E_{\perp}/E_{//}$. Note that P is a function of the three random variables θ, ρ, and φ. The distribution of θ may be found from ray tracing results using the expression in (5.1). However, the distributions of ρ and φ are related to the complex scattering coefficients of the ground and do not have a simple representation. We approach this problem instead by assuming φ and ρ to be independent RV's with assumed distributions. Due to the complexity of the problem we assume the distribution of φ to be uniform over a range $[0,2\pi]$. For the PDF of ρ we choose the general exponential distribution of the form

$$p_\rho(\rho) = \frac{1}{\mu}e^{-\frac{\rho}{\mu}}, \tag{5.5}$$

which is a function of the single parameter μ. If we let $\mu \to 0$, then $p_\rho(\rho)$ approaches a delta function at zero which corresponds to a received signal that is linearly polarized along what we have denoted the parallel axis in Figure 5.3. In the limit that $\mu \to \infty$, $p_\rho(\rho)$ approaches a uniform distribution, which would correspond to a received signal that whose ratio of transverse amplitudes may take any value in the range $[0,\infty]$ with equal probability. Therefore, the choice of an exponential distribution for ρ provides a convenient method of testing a variety of cases by varying a single parameter.

Given distributions of ρ and φ, (5.4) may be averaged over these parameters to obtain

$$\bar{P}(\theta) = A\cos^2\theta + B\sin^2\theta \qquad (5.6)$$

where the coefficients A and B are given by

$$\begin{cases} A = \int \frac{1}{1+\rho^2} p_\rho(\rho)d\rho \\ B = \int \frac{\rho^2}{1+\rho^2} p_\rho(\rho)d\rho \end{cases} \qquad (5.7)$$

Note that $\bar{P}(\theta)$ is independent of φ when φ is assumed to be uniformly distributed over 2π radians. In section 5.3, we will investigate the dependence of the results on the form of the distribution $p_\rho(\rho)$. Given the PDF of θ from ray tracing results and the constant coefficients A and B for a given distribution $p_\rho(\rho)$, the PDF of $\bar{P}$ is found from the RV transformation denoted in (5.6).

After obtaining a distribution of incident power S_I from ray tracing results as described in the section 5.2.1, the distribution of received power may be formulated as the product

$$S_R = S_I\bar{P}. \qquad (5.8)$$

Note that if $\bar{P}$ and S_I are transformed to a logarithmic base then (5.8) becomes

$$\log S_R = \log S_I\bar{P} = \log S_I + \log\bar{P}, \qquad (5.9)$$

and $p_{\log S_R}(x)$ can be expressed as

$$p_{\log S_R}(x) = p_{\log\bar{P}}(x) * p_{\log S_I}(x). \qquad (5.10)$$

5.2.3 Noise

The measured distribution of ground-scattered power is a function in part of various noise processes throughout the radar system. If the random noise is assumed to be additive and independent of the ground scattered signal then the overall variance of the received signal is simply the sum of the variance of the ground scattered signal and the variance of the noise. In addition to the effect of additive noise, the measured results presented in this study are influenced by the fact that power is expressed in decibels

above an estimated noise level. The effects of noise on the observed distribution will be discussed in terms of the separate effects of 1) addition of random noise power and 2) normalization by a random noise estimate.

5.2.3.1 Additive Noise

Consider first that the received signal at the antenna is converted into baseband in-phase (I) and quadrature (Q) components. If the assumption is made that the band-pass noise is additive, white, and Gaussian (AWGN), then the baseband signal has noise components n_I and n_Q in the I and Q dimensions that are identically distributed zero-mean Gaussian random processes, i.e. $N(0, \sigma)$. In addition, if the power spectrum of the signal of interest is symmetric about the modulation frequency, then it can be shown that the low-pass noise components in the I and Q dimensions are uncorrelated and independent [*Carlson et al.*, 2002]. The total noise power under these assumptions is then given by

$$n_P = n_I^2 + n_Q^2. \tag{5.11}$$

Considering that n_I and n_Q are identically distributed zero-mean Gaussian random variables, $p_{n_P}(x)$ can be shown to be

$$p_{n_P}(x) = p_{n_{I/Q}^2} * p_{n_{I/Q}^2} = \frac{1}{2\sigma^2} e^{-\frac{x}{2\sigma^2}}, \quad x \geq 0. \tag{5.12}$$

Note (5.12) can be derived by finding the square of a Rayleigh distribution. Given the distribution of $p_{n_P}(x)$ and the distribution of the received signal $p_{S_R}(x)$ derived by considering the effects of a time-variant propagation path and a random signal polarization, the distribution of the sampled signal, $p_{S_M}(x)$, is the convolution of the two component distributions:

$$p_{S_M}(x) = p_{n_P}(x) * p_{S_R}(x). \tag{5.13}$$

In (5.13) it is important to note that the distributions of $p_{n_P}(x)$ and $p_{S_R}(x)$ correspond to linear values of the respective RV's. In Section 5.2.2 we found $p_{\log S_R}(x)$ so that $p_{S_R}(x)$ may be found by a RV transformation from decibels to linear units.

5.2.3.2 Noise Normalization

In standard operation, SuperDARN radars transmit multiple-pulse sequences and calculate the autocorrelation function (ACF) of the backscattered signal. The ACF from N transmit sequences are averaged together and a fitting method is used to calculate parameters including Doppler velocity and spectral width at each range bin. The ten lowest power (un-fitted) range bins are averaged together and interpreted as an estimate of the noise level. Power values are then expressed in decibels above the estimated noise level.

Assuming that noise samples from different transmit sequences are independent and identically distributed, the noise power distribution after averaging N transmit sequences together can be found by convolving $p_{n_P}(x)$ in (5.12) with itself $N - 1$ times and scaling by a factor of $1/N$ to yield $p_{n_{P-AVE}}(x)$. Next, $p_{n_{P-AVE}}(x)$ can be convolved with itself nine times and scaled by a factor of $1/10$ to yield the noise estimate distribution, $p_{n_{EST}}(x)$ that results from averaging ten range bins together. If we perform a RV transformation of the sampled signal S_M and the noise level estimate n_{EST} from linear units to decibels then the PDF of the sampled received signal distribution S in decibels above the estimated noise level can be expressed as

$$p_{\log S}(x) = p_{\log S_M}(x) * \left(-p_{\log n_{EST}}(x)\right). \tag{5.14}$$

5.2.3.3 Determining Noise PDF's from Measurements

Given the analysis in sections 5.2.3.1-5.2.3.2, the effects of noise on the measured signal distribution can be accounted for by estimating the parameter σ that controls the shape of the noise power, $p_{n_P}(x)$, and estimated noise level, $p_{n_{EST}}(x)$, distributions. A maximum-likelihood-estimate (MLE) of σ was determined by comparing theoretical curves of $p_{n_{EST}}(x)$ for arbitrary values of σ to a data set of observed noise level estimates. The distribution of $p_{n_P}(x)$ can then be found from (5.12) after finding the

MLE of σ. Figure 5.4 (a) illustrates a comparison of a measured distribution of estimated noise level and a MLE fit curve of $p_{n_{EST}}(x)$ whereas Figure 5.4 (b) illustrates the corresponding curve of $p_{n_P}(x)$.
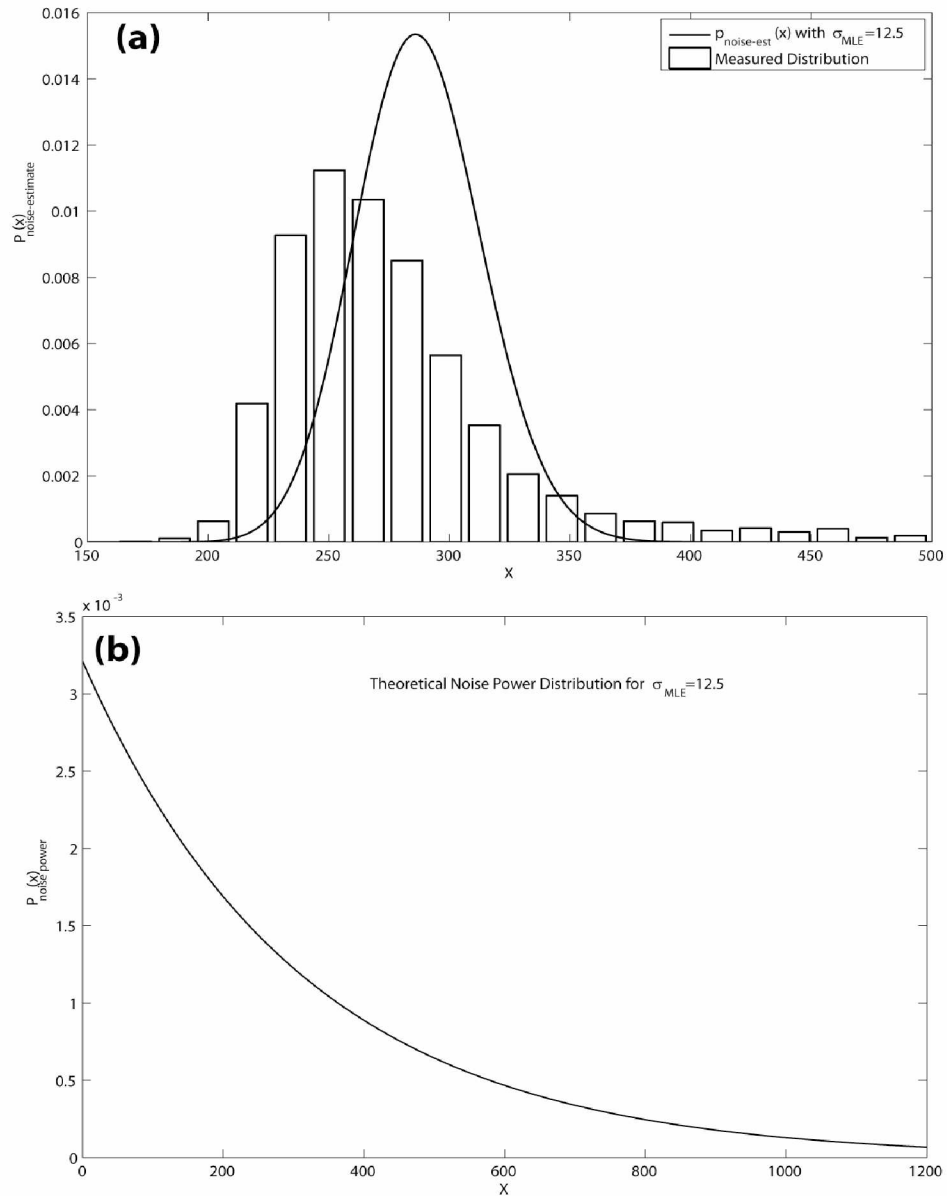
Figure 5.4: A comparison of theoretical and measured distributions of estimated noise level $p_{n_{EST}}(x)$ in (a) and the corresponding theoretical distribution of noise power $p_{n_P}(x)$ in (b). The measured distribution was generated from 3245 samples of sky noise taken 16 October 2009 between UT 00:00:00-01:00:00. Note that the x-axis values of power in (a) and (b) are relative to the analog-to-digital converter sample values of the radar hardware. These probability distributions are subsequently normalized to the maximum observed mean power level so that an equivalent distribution can be generated relative to the numerical values produced in simulation.

Note that the MLE fit curve of $p_{n_{EST}}(x)$ in Figure 5.4 (a) does not provide an accurate fit to the measured distribution. The discrepancy between the theoretical and measured distributions is likely due to the fact that some of the range bins that are averaged to produce a noise estimate contain backscatter from either ionospheric irregularities or the ground. A better fit may be achieved using an alternative theoretical distribution for $p_{n_{EST}}(x)$ but the advantage of using the given distribution is that $p_{n_P}(x)$ is directly known from the relationship discussed in section 5.2.3.2. Note that the theoretical fit of $p_{n_{EST}}(x)$ has less variance than the observed estimated noise and consequently the theoretical curve of $p_{n_P}(x)$ will have less variance than the true curve of noise power. As discussed in sections 5.2.3.1-5.2.3.2, the noise PDF's are convolved with either linear or logarithmic versions of the received signal distribution to account for addition and normalization. The effect of convolution on the ground-scattered power distribution is an increase in variance proportional to the variance of the noise distributions. Consequently, underestimating the variance in the noise distributions will result in an underestimate of the variance in the simulated signal power distribution. However, it will be shown that the noise processes contribute a negligible amount of variance to the total observed ground-scattered power distribution in comparison to the effects of a time-variant propagation path, random polarization, and data averaging. Hence, a more accurate model of the noise distributions will not be pursued here.

5.2.4 Ground Scatter Correlation

As discussed in section 5.2.3.2, the data product in this study undergoes averaging. Specifically, the ACF's from N transmit sequences are averaged together and the lag zero power value of the averaged ACF is taken as an estimate of the received signal power during the integration period. The effect of averaging on the measured distribution of signal power depends on the amount of correlation in the ground scatter between transmit sequences. If samples from different transmit sequences are assumed to be independent and identically distributed then the effect of averaging over N transmit

sequences can be determined by convolving the PDF of the received signal plus noise, $p_{S_M}(x)$, with itself $N-1$ times and scaling by a factor of $1/N$. Conversely, if samples from different transmit sequences are assumed to be deterministic then the distribution of received signal plus noise is unaltered by averaging.

The variance of the received signal plus noise distribution after averaging is a function of the correlation, η, in the ground scatter between transmit sequences. In general, the variance of an average of N random variables that have an average correlation of η is

$$\text{VAR}[\bar{X}] = \frac{\sigma^2}{N} + \frac{N-1}{N}\eta\sigma^2. \tag{5.15}$$

As can be seen from (5.15), the variance of the distribution after averaging is bounded by

$$\frac{1}{N}\sigma^2 \leq \sigma_{AVE}{}^2 \leq \sigma^2 \tag{5.16}$$

where σ^2 is the variance prior to averaging. These bounds correspond to the cases of either independent or deterministic ground scatter samples between transmit sequences that were discussed. It will be shown in section 5.3 that signals are correlated over a period of approximately three integration intervals which implies that signals during a single integration interval are well correlated. Simulation results will be presented for the upper and lower bounds in (5.16).

5.2.5 Simulation Overview

A simulated distribution of ground-scattered power is achieved by first obtaining a distribution given a randomly perturbed ionosphere and then transforming that distribution to account for random polarization, noise, and ground scatter correlation. First, L ray tracing trials are performed to generate a simulated PDF of incident power, $p_{S_I}(x)$, due to a time-variant propagation path resulting from random electron density fluctuations. Next, given the distribution of the Faraday rotation angle θ determined from ray tracing results and a choice of the distribution $p_\rho(\rho)$, the PDF of the averaged polarization factor $\bar{P}$ is determined from the RV transformation in (5.6). The received

signal distribution $p_{\log S_R}(x)$ accounting for a random polarization may then be found from convolving the distributions of $p_{\log \bar{P}}(x)$ and $p_{\log S_I}(x)$. On the assumption that AWGN corrupts the signal, $p_{S_R}(x)$ is convolved with a theoretical noise power distribution $p_{n_P}(x)$ to yield the sampled signal PDF $p_{S_M}(x)$. At this point, the effect of data averaging in the limiting cases that ground scatter samples between transmit sequences are either deterministic or independent is considered. While $p_{S_M}(x)$ is unaltered by data averaging in the case of deterministic samples, the assumption of independent samples requires a transformation of $p_{S_M}(x)$ as discussed in Section 5.2.4 to yield $p_{S_M}{}^*(x)$. Finally, $p_{S_M}(x)$ and $p_{S_M}{}^*(x)$ are transformed to reflect normalization by a random noise estimate, $p_{n_{EST}}(x)$, to yield the theoretical PDF of ground-scattered power, $p_S(x)$ or $p_S{}^*(x)$.

5.3 Analysis

The result of the simulation process described in section 5.2 is a PDF of ground-scattered power at each time delay range where observations are made by the Kodiak SuperDARN. These results will be analyzed in terms of the corresponding statistical averages of mean and standard deviation versus time delay range. First in section 5.3.1, the contribution of each random process modeled in simulation to the simulated mean and standard deviation versus time delay profile will be investigated. Next, in section 5.3.2 the simulation results and observations will be analyzed by comparing sample estimates of mean and standard deviation as a function of time delay range. Given observed ground-scattered power distributions of N samples at each range bin, estimates of the mean and standard deviation are calculated using the expressions

$$\hat{\bar{x}} = \frac{1}{N}\sum_{t=1}^{N} x_t, \tag{5.17}$$

and

$$\widehat{\sigma_x} = \sqrt{\frac{1}{N-1}\sum_{t=1}^{N}(x_t - \hat{\bar{x}})^2}. \tag{5.18}$$

5.3.1 Comparison of Random Process Effects

Here we investigate the effects of each of the modeled random processes on the simulated mean and standard deviation profiles as a function of range. First we investigate the effects of the noise processes and verify our claim in section 5.2.3 that noise processes contribute a negligible amount of variance to the overall profile. Next we study the effects of random polarization as discussed in section 5.2.2. In particular, we will explore the choice of the $p_\rho(\rho)$ distribution on the composite standard deviation profile. Finally, we consider the effects of altering the width of the electron density perturbation amplitude distribution and the perturbation scale size.

5.3.1.1 Noise Process Effects

Figure 5.5 (a)-(b) illustrate the simulated mean and standard deviation profiles that were calculated by considering the effects of the noise processes discussed in section 5.2.2 in addition to electron density perturbations with amplitudes drawn from $N(0,10\%)$ and a scale size of 5 km. For clarity Figure 5.5 illustrates upper-bound curves only which means that the ground scatter samples between transmit sequences are assumed to be completely correlated. In Figure 5.5 (a) the three mean profile curves generated considering electron density perturbations alone and electron density perturbations in addition to the noise processes are nearly indistinguishable. Similarly, in Figure 5.5 (b) the three standard deviation profile curves differ at most by tenths of a decibel which supports our earlier claim that the noise processes contribute a negligible amount of variance to the observed ground scatter statistics.
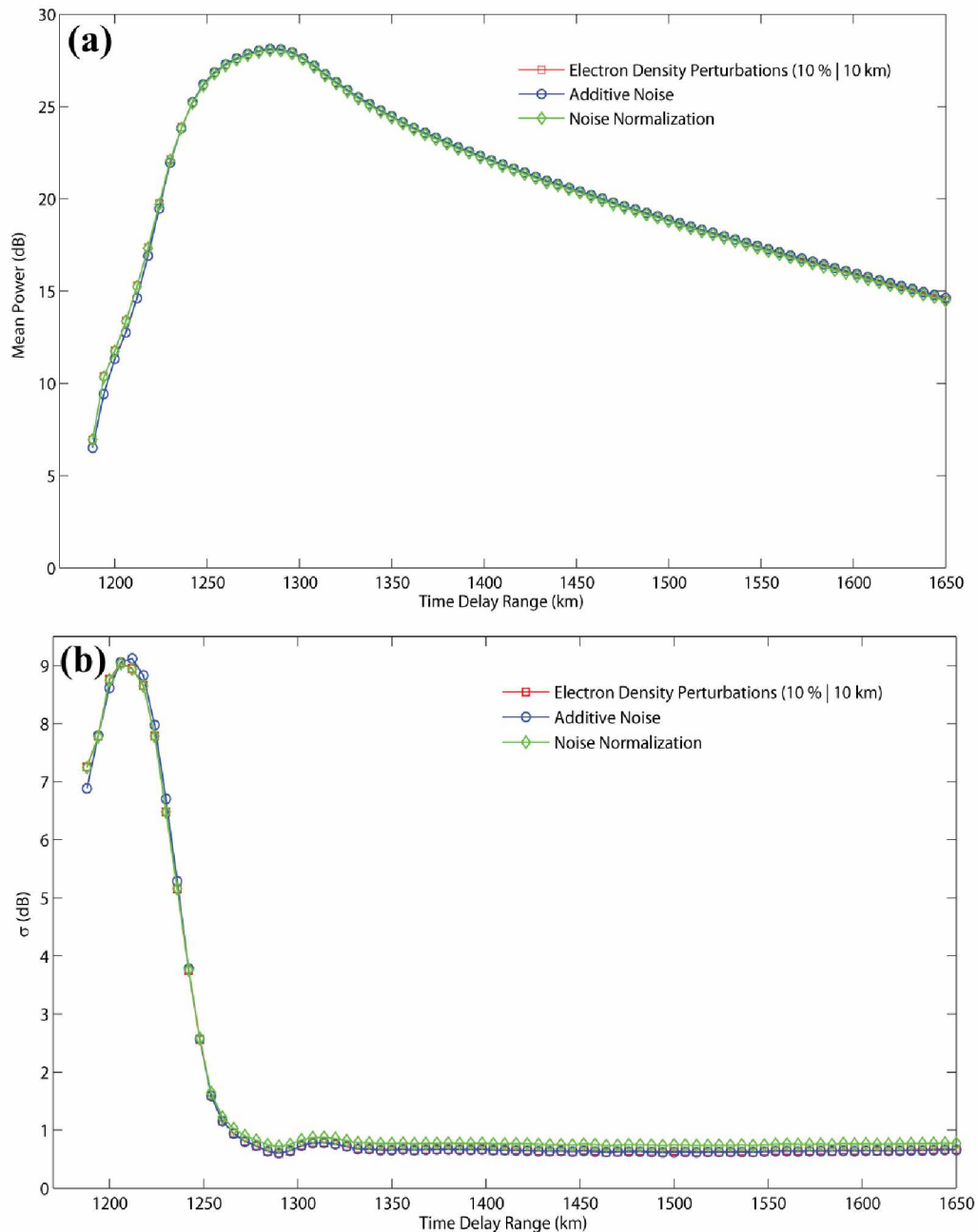
Figure 5.5: A comparison of the contribution noise processes to the simulated mean and standard deviation profile for typical simulation results. Note that the mean and standard deviation curves for each random process are in addition to the depicted curves generated with electron density perturbations. The electron density perturbation amplitudes were distributed according to $N(0,10\%)$ with a scale size of 5 km. In addition, the curves illustrated in (b) are upper-bounds on standard deviation which means that ground scatter samples between transmit sequences in the same integration interval are assumed to be completely correlated.

5.3.1.2 Polarization Effects

Before investigating the effects of the polarization factor $\bar{P}$ on the mean and standard deviation profiles, we demonstrate that the Faraday rotation angle θ distribution is relatively insensitive to perturbation parameters. Figure 5.6 (a) illustrates the simulated histogram of θ at an arbitrary range gate for a set of density perturbation parameters and Figure 5.6 (b) illustrates the mean and standard deviation of the simulated θ distributions for a variety of perturbation parameters. In Figure 5.6 (a) note that the simulated distribution is approximately Gaussian in shape as demonstrated by the overlaid Gaussian curve. In addition, the curves in Figure 5.6 (b) demonstrate that the mean and standard deviation of the θ distributions versus range are relatively independent of the annotated density perturbation parameters. For simplicity, we assume that the θ distributions are independent of the density perturbation parameters and have a Gaussian distribution at each range gate with mean and standard deviation given by the average of the curves for various perturbation parameters illustrated in Figure 5.6 (b).
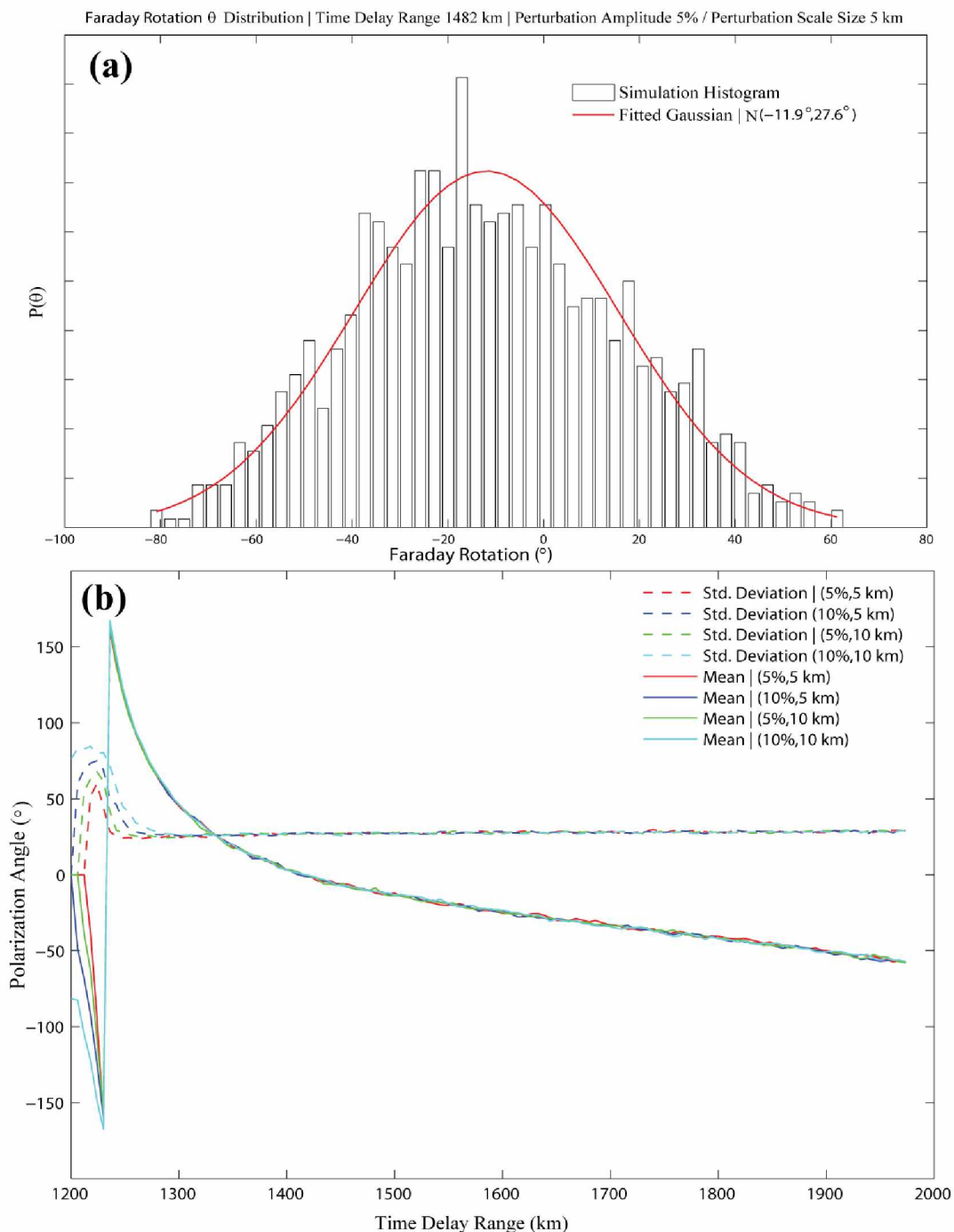
Figure 5.6: Example distribution of Faraday rotation in addition to the simulated moment profiles. The plot in (a) illustrates the histogram of simulated Faraday rotation angles at a range gate of 1482 km in addition to a fitted Gaussian curve with parameters $\mathcal{N}(-11.9°, 27.6°)$. The plot in (b) depicts the simulated mean and standard deviation curves versus time delay range for the annotated perturbation parameters.

Given the PDF of θ, the polarization factor $\bar{P}$ distribution may be found from the RV transformation in (5.6) given coefficients A and B. We now turn our attention to the form of the distribution $p_\rho(\rho)$ which governs the values of A and B. Recall that we chose $p_\rho(\rho)$ to be a general exponential distribution as in (5.5) which is a function of the single parameter μ. Figure 5.7 (a)-(b) depict the mean and standard deviation profiles given the $\bar{P}$ distribution that corresponds to the annotated choice of μ for a given set of perturbation parameters. Note in Figure 5.7 that each curve is generated considering the effects of electron density perturbations, noise, and random polarization with a $\bar{P}$ distribution found using (5.5)-(5.7) for the annotated value of μ. However, only upper bound curves corresponding to completely correlated ground scatter samples between transmit sequences during an integration interval are illustrated in Figure 5.7. As depicted in Figure 5.7, the choice of μ is an influential factor in the shape of the mean and standard deviation profiles. In general, increasing the value of μ increases the roll-off of the mean profile and raises the standard deviation at time delay ranges greater than 1300 km. In order to determine a value of μ and fully specify the $\bar{P}$ distribution, we choose the value of μ that produces the best fit of both the simulated mean and standard deviation profiles to the measured results.
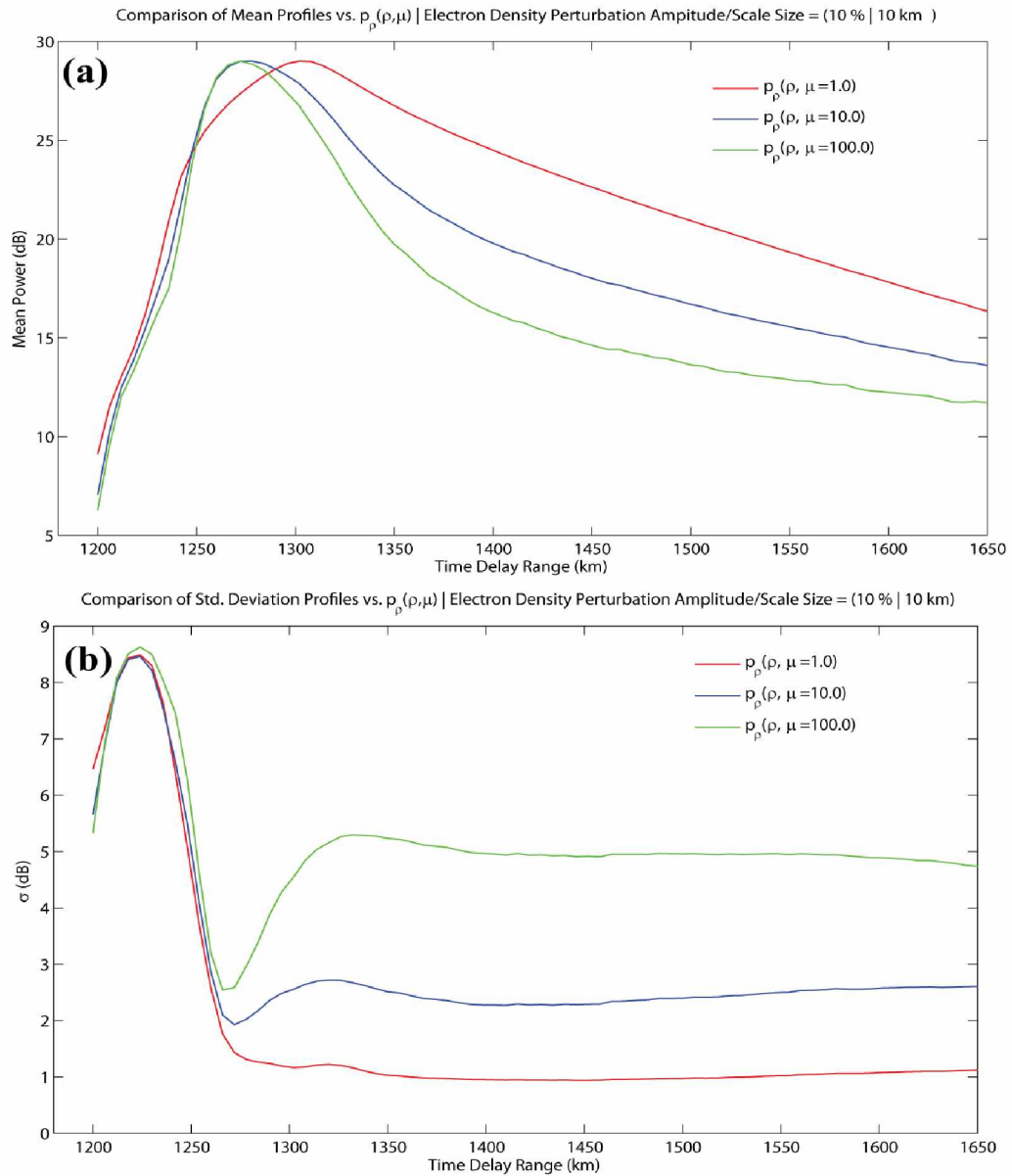
Figure 5.7: A comparison of the simulated mean and standard deviation profiles for a variety of polarization factor, $\bar{P}$, distributions. The $\bar{P}$ PDF used to generate each curve is found using the expressions in (5.5)-(5.7) for the annotated value of μ. Note each curve in the figure is generated considering all random processes discussed in Section 5.2 where the electron density perturbations are distributed according to $N(0,10\%)$ with a scale size of 10 km. In addition, the curves illustrated in (b) are upper-bounds on standard deviation which means that ground scatter samples between transmit sequences in the same integration interval are assumed to be completely correlated.

5.3.1.3 Electron Density Perturbation Effects

Here we investigate the effect of the electron density perturbation amplitude and scale size on the simulated mean and standard deviation profile. All random processes including noise and polarization are included in the results presented in this section. Note that we use a value of $\mu = 10.0$ and (5.5)-(5.7) to calculate the PDF of the averaged polarization factor $\bar{P}$. In addition, only upper bound curves corresponding to completely correlated ground scatter samples between transmit sequences during an integration interval are illustrated. Figure 5.8 illustrates the mean and standard deviation profiles found by varying the perturbation scale size between 5-20 km while maintaining a perturbation amplitude distribution of $N(0,10\%)$. Figure 5.9 illustrates the mean and standard deviation profiles found by increasing the width of the perturbation amplitude distribution from $N(0,5\%) - N(0,20\%)$ while maintaining a constant scale size of 10 km.
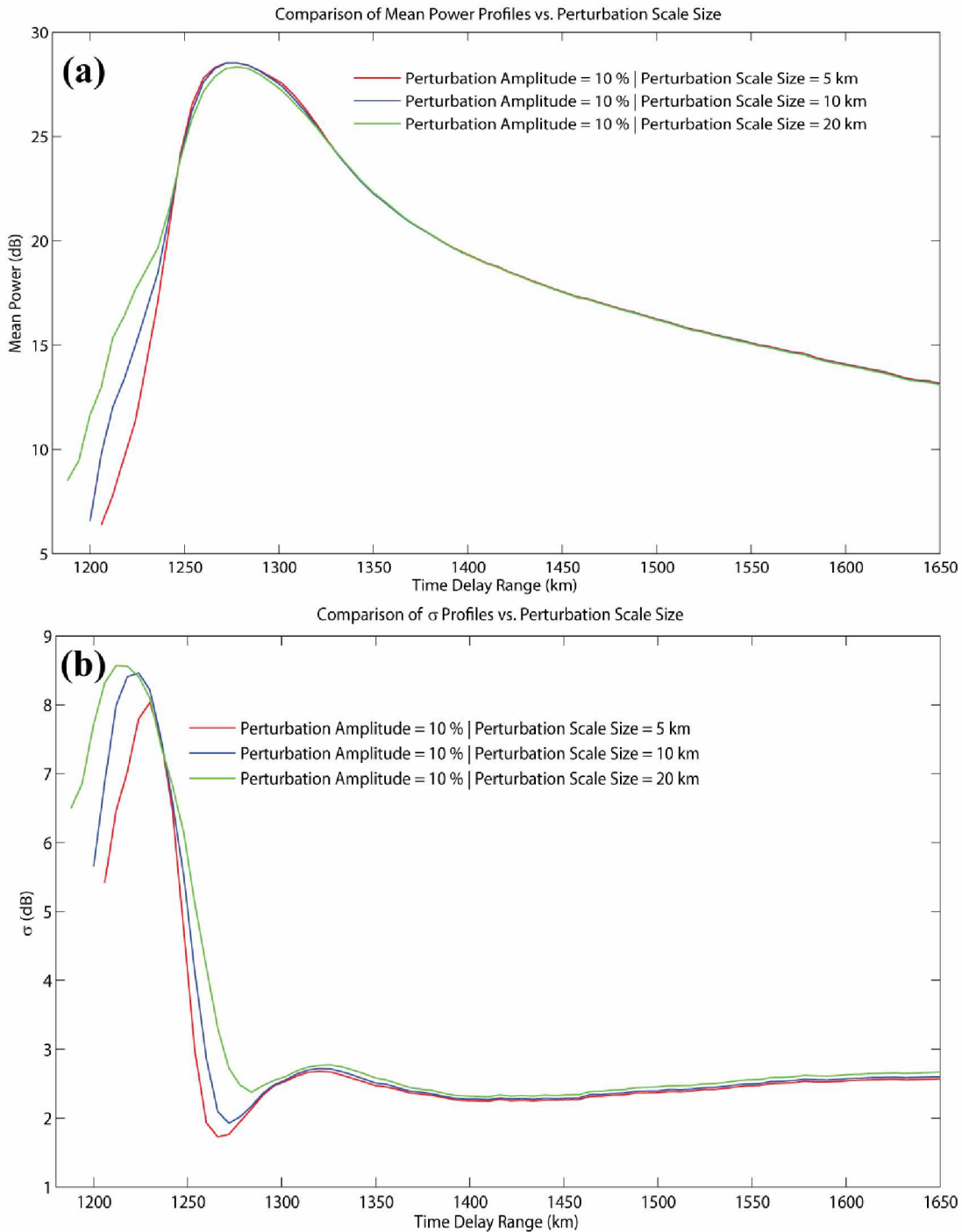
Figure 5.8: A comparison of the simulated mean and standard deviation profiles for a variety of perturbation scale sizes. The perturbation amplitude for each curve was distributed according to $\mathcal{N}(0,10\%)$. In addition, the curves illustrated in (b) are upper-bounds on standard deviation which means that ground scatter samples between transmit sequences in the same integration interval are assumed to be completely correlated.
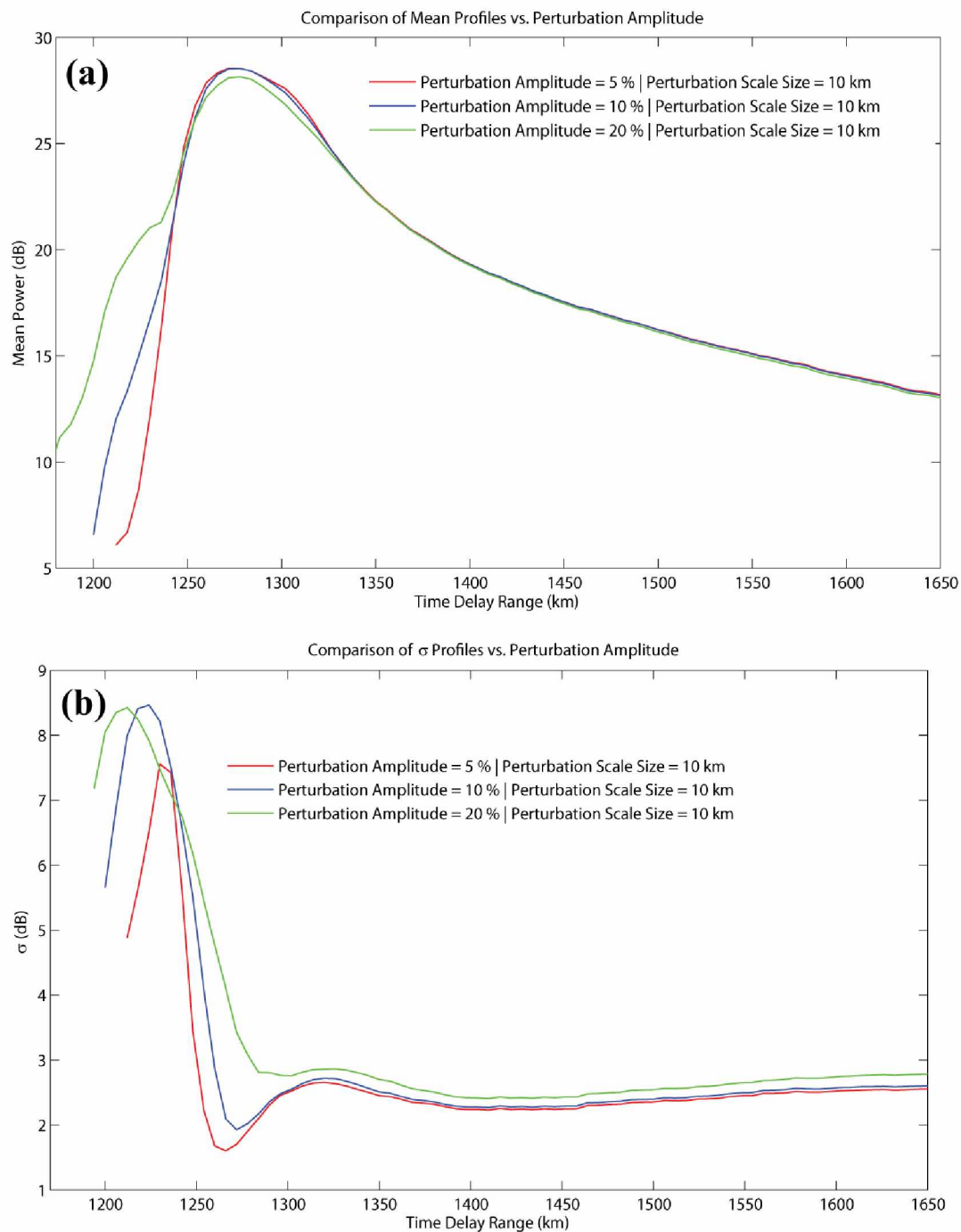
Figure 5.9: A comparison of the simulated mean and standard deviation profiles for a variety of perturbation amplitude distribution widths. The perturbation scale size for each curve was held constant at 10 km. In addition, the curves illustrated in (b) are upper-bounds on standard deviation which means that ground scatter samples between transmit sequences in the same integration interval are assumed to be completely correlated.

In general, note from Figure 5.8 and Figure 5.9 that the standard deviation is proportional to the slope of the mean profile. To illustrate, note that the large local maximum region in all the standard deviation profiles around 1200 km in range corresponds to the region of the mean profile preceding the skip distance maximum where the slope is very steep. Similarly, at ranges greater than the skip distance maximum where the slope of the mean profile is relatively constant, the standard deviation profile remains approximately constant. Next, note that increasing either the perturbation width or the perturbation scale size has the effect of raising the level of the mean profile. In general, the magnitude of power enhancements or reductions is proportional to perturbation amplitude and scale size. However, the mean profile tends to increase as the width of the perturbation amplitude distribution increases or the perturbation scale size increases because the minimum power received is bounded below by the noise level. Therefore, even though power reductions are as likely as power enhancements, the mean increases because the distribution of ground-scattered power can only expand in one direction.

Finally, note that increasing the perturbation amplitude or scale size results in a modest increase in the standard deviation profile. In the local maxima region between 1200-1250 km of the standard deviation profile, doubling or quadrupling the width of the perturbation amplitude distribution or the perturbation scale size results in an increase of about 1 dB. In addition, the width of the local maximum region increases between 10-20 km for each doubling of either the perturbation amplitude or scale size. At ranges greater than 1300 km of the standard deviation profile, doubling or quadrupling the perturbation parameters results in an increase on the order of tenths of a decibel.

5.3.2 Comparison of Simulated and Measured Distributions

In performing this study, a time period was sought where the ground-scattered power observed at Kodiak appeared to be uniform over an extended duration. After finding an appropriate time period, correlation of ground scatter between integration

intervals was investigated by calculating the sample ACF of lag zero power at numerous range bins using the expression

$$R(k) = \frac{c(k)}{c_0} \tag{5.19}$$

where $c(k)$ is an estimate of the autocovariance at lag k given by

$$c(k) = \frac{1}{N}\sum_{t=1}^{N-k}(x_t - \bar{x})(x_{t+k} - \bar{x}), \tag{5.20}$$

and x_t is the discrete time series of measured lag-zero power. Inspection of the sample ACF at various range bins was used to determine the minimum lag spacing K required for a set of independent samples. In addition to being spaced by a minimum number of integration intervals, the samples were also filtered based on whether or not the spectral width and Doppler velocity at that range bin are consistent with ground scatter. Given an appropriate set of measured samples at each range bin, simulated distributions were then generated as described in section 5.2.5 given variable perturbation amplitude distributions and scale sizes. The background ionospheric density profile used in simulation was based on ionosonde measurements made at the High Altitude Auroral Research Program (HAARP) station in Gakona, Alaska.

5.3.2.1 Measured Statistics

As previously discussed, visual inspection of RTI plots illustrates that the ground-scattered power observed in beam direction 9 is relatively uniform on 16 October 2009 between UT 00:25:00-00:40:00 where Figure 5.1 (a) illustrates the RTI plot during this interval. Figure 5.10 illustrates the corresponding sample ACF calculated over a time series of $N = 164$ samples where each sample corresponds to an integration interval of 1 second.
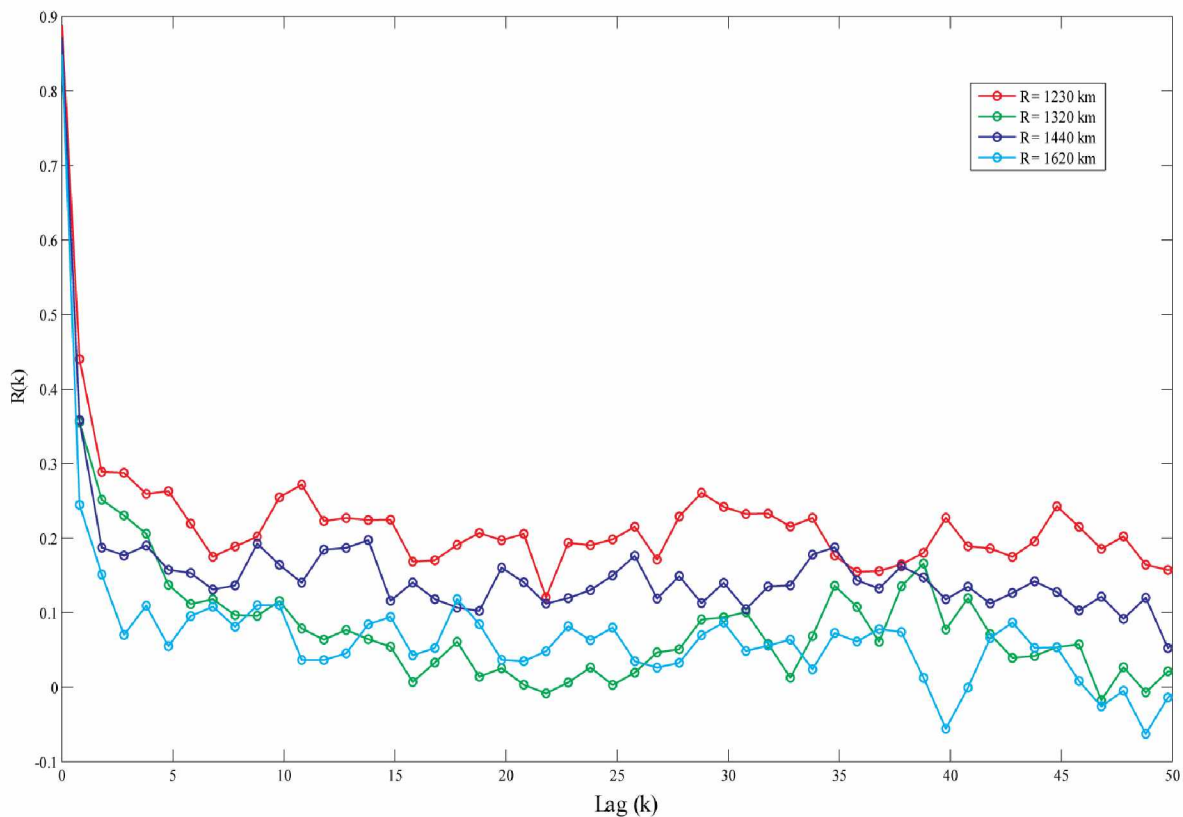
Figure 5.10: Sample autocorrelation function of lag zero power at various range bins on 16 October 2009 UT 00:25:00-00:40:00. Note the sample population size was $N = 816$ and (5.20) was calculated for lags $0 \leq k \leq 164$.

Note in Figure 5.10 that lag-zero power values are correlated over an interval of no more than $K = 3$ lags regardless of range. A set consisting of 816 samples during the time period UT 00:25:00-00:40:00 was decimated by a factor of $1/3$ and further filtered by considering only those samples flagged as ground scatter. The final set of independent measured ground scatter samples includes $N = 136$ samples at 300 range bins spanning a time delay range of 180-1974 km.

5.3.2.2 Results

Simulation results were generated for a variety of perturbation parameters given a background ionospheric density profile based on ionosonde measurements made at the HAARP station in Gakona, Alaska during the period 16 October 2009 between UT 00:25:00-00:40:00. A value of $\mu = 50$ was chosen in order to calculate the polarization factor $\bar{P}$ distribution from (5.5)-(5.7) after visually inspecting the fit of the simulated mean and standard deviation profiles to the measured results. As discussed in section 5.3.1.3, the effects of increasing the width of the perturbation amplitude distribution is similar to increasing the perturbation scale size so there is not a unique set of perturbation parameters that approximate the measured data.

Figure 5.11 (a)-(b) illustrates a comparison of the measured mean and standard deviation profile to the simulation results obtained with electron density perturbation amplitudes distributed according to $\mathcal{N}(0,10\%)$ and a scale size of 20 km. In Figure 5.11 (a), the solid and dashed curves represent the simulated mean profile given sample sizes of $N = 10^4$ and $N = 136$ respectively. Note that at distances greater than the skip distance maximum, the simulation curves accurately approximate the trend of the measured profile. The effect of the relatively small sample size of $N = 136$ on the simulation results is to introduce perturbations on the order of one decibel about the curve obtained with $N = 10^4$ samples.
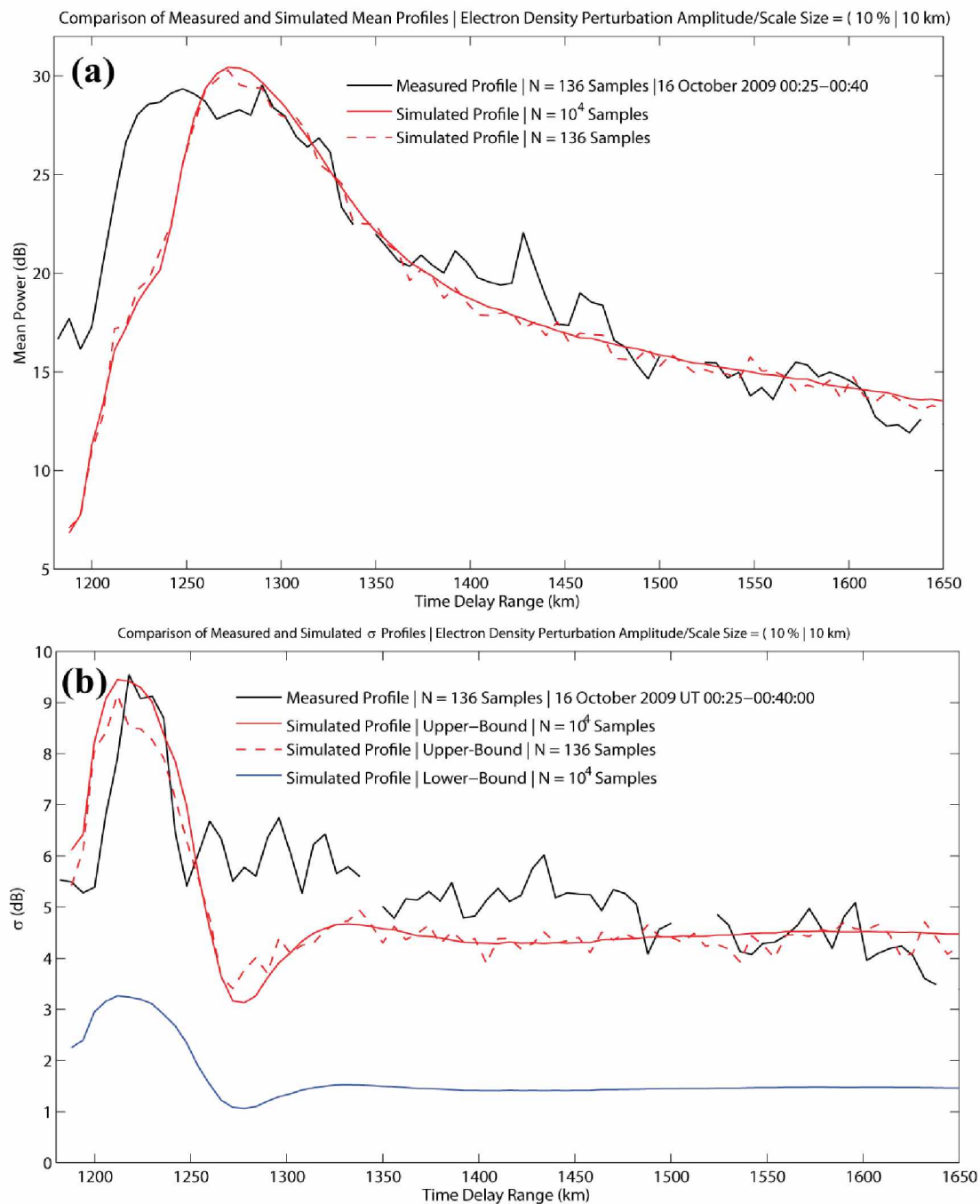
Figure 5.11: A comparison of observed and simulated mean, (a), and standard deviation, (b), profiles. The observed profiles are estimated from a sample set of $N = 136$ samples on 16 October 2009 between UT 00:25:00-00:40:00. Simulation curves are presented for sample sizes of $N = 136$ and $N = 10^4$ in both plots. Note that (b) features simulation curves for the upper and lower bounds on standard deviation corresponding to assumptions of complete correlation or complete independence between ground scatter samples from different transmit sequences in the same integration interval.

Figure 5.11 (b) illustrates a comparison of three simulation curves with the measured profile. The red and blue colored curves illustrate the upper and lower bounds on standard deviation that are a function of ground scatter sample correlation between transmit sequences as discussed in section 5.2.4. As in Figure 5.11 (a), the solid and dashed red curves illustrate simulation results for sample sizes of $N = 10^4$ and $N = 136$ respectively. The effect of a small sample size of $N = 136$ is to introduce perturbations on the order of one-half decibel about the curve obtained with $N = 10^4$ samples. Note in Figure 5.11 (b) that the upper-bound simulation curves capture the most prominent features of the measured profile including a local maxima region centered at 1225 km with a width of 50 km and a peak value of approximately nine decibels. In addition, at ranges beyond 1300 km the simulated curves are approximately flat and within one-half decibel of the measured standard deviation profile. However, we note that the simulated curves feature a dip in standard deviation near 1275 km that is not a characteristic of the measured profile. In addition, the simulated curves fail to capture the small negative trend of the measured profile at ranges greater than 1250 km.

One of the objectives of this study was to quantify background electron density perturbations in the ionosphere. From inspection of Figure 5.11 (a)-(b), we find that the annotated electron density perturbation parameters re-create the most prominent characteristics of the mean and standard deviation profiles such as trend and local maxima. However, a number of factors limit the accuracy of our estimate of the perturbation parameters. As mentioned previously, the effects of increasing the width of the amplitude distribution and increasing the perturbation scale size are very similar which creates ambiguity in any attempt to specify a particular set of perturbation parameters by comparison with the measured statistical moment profiles. In addition, we noted that restrictions on the independence of ground scatter samples between integration intervals and a static background ionospheric profile limits the size of the measurement sample set. A limited sample size may obscure important features in the measured statistical moment profiles. Finally, we utilized an averaged polarization factor $\bar{P}$ whose

PDF is found by assuming PDF's of unknown parameters and averaging over the spectrum of the unknown parameters as discussed in section 5.2.2. Although we found that the simulated profiles capture the most prominent feature of the measured results, some of the noted discrepancies may be resolved with a more accurate model of the polarization factor.

5.4 Discussion

In this chapter, the ground-scattered power distributions observed by the Kodiak SuperDARN were investigated by comparing estimates of mean and standard deviation as a function of time delay range. Four fundamental random processes including time-variant propagation path due to electron density perturbations, random signal polarization, system noise, and ground scatter correlation were modeled in generating simulated distributions of ground-scattered power.

A number of factors contribute to discrepancies between the simulated and observed statistics. These factors include ambiguity between the width of the electron density perturbation amplitude distribution and the perturbation scale size, the limited sample size of measured results, and uncertainty in the form of the polarization factor PDF.

Despite these limitations, it was shown that the most prominent features in the measured statistical moment profiles are directly related to the effects of electron density perturbations. Future work may include refining the model of the polarization factor through experimental observations and obtaining tighter bounds on the standard deviation profile by calculating the correlation of ground scatter samples between transmit sequences in the same integration interval. With the refinements suggested above, the simulation method presented here would provide a more accurate tool for quantifying electron density perturbations in the ionosphere and predicting oblique HF clutter distributions.

Chapter 6   Conclusions & Future Work

6.1 Conclusion

The objective of this thesis was the development of a robust numerical method of calculating ground-scattered power for HF OTH radars from the results of ray tracing along with two significant applications. In Chapter 3, an improved numerical method of calculating ground-scattered power from the results of ray tracing was presented. The improved method overcomes limitations in a previous method published by *Bristow &* *Greenwald 1995* and provides a valuable tool for studying a variety of different physical processes. Two applications were investigated in Chapter 4 and Chapter 5. In Chapter 4, the effects of an artificial layer on observed ground-scattered power was investigated and it was demonstrated that a simple model could be used to accurately predict the location and amplitude of power enhancements. Conversely, a comparison of simulated and observed ground-scattered power profiles can be utilized to estimate the physical dimensions and altitude of artificial layers. In Chapter 5, a method of investigating the physical processes that produce the temporal variation in observed ground-scattered power was investigated. Specifically, statistical moment versus time delay range profiles were simulated using a Monte-Carlo method. It was demonstrated that the observed statistical moment profiles could be related to the random processes of electron density fluctuations, polarization, noise, and correlation of ground scatter samples.

6.2 Future Work

There are a number of areas in which the research presented here may be improved or expanded. First, all of the research presented in this thesis is based on ray tracing that is performed in two dimensions with the implicit assumption of uniformity in the remaining dimension. It is a straightforward and simple matter to modify the existing

ray tracing code to be performed in three dimensions as discussed in the theory presented in Chapter 2. Furthermore, the numerical method presented in Chapter 3 can be modified in a straightforward manner to calculate the ground-scattered power from the results of a three-dimensional ray tracing analysis. Note that the results of a ray-tracing analysis in three dimensions would be (x, y) coordinates of rays that intersect the ground plane as a function of time delay. Following the theory presented in Chapter 3, the rays contained in the illuminated area at an arbitrary time could be related to a solid angle of the transmitted beam pattern and consequently a total amount of scattered power may be found by integrating over the appropriate solid angle surface. Assuming isotropic re-radiation, one would arrive at an expression very similar to equation (3.6) where the single integral over an elevation angular length would be replaced by a double integral over a solid angle surface. The most important advantage of performing ray tracing in three dimensions and using the results to calculate ground-scattered power would be the ability to investigate focusing effects that occur in azimuth rather than elevation. The ability to determine ray focusing in azimuth may provide further insight into the investigation of artificial layer effects on ground-scattered power presented in Chapter 4.

The Monte-Carlo simulation method presented in Chapter 5 provided insight into the physical phenomena that contribute to observed ground scatter statistics. However, a number of factors limited the utility of the method to accurately characterize background electron density perturbations. These factors include ambiguity between the width of the electron perturbation amplitude distribution and the scale size of the perturbations, uncertainty in the form of the polarization factor PDF, and also the amount of correlation between ground-scatter samples from different transmit sequences but the same integration interval. The ambiguity between the width of the electron perturbation amplitude distribution and the scale size of the perturbations may be eliminated in future work by allowing the scale size to be a random variable with a defined distribution and then averaging the results over the scale size distribution. In addition, uncertainty in the form of the polarization factor PDF may be removed through experimental results where

the full polarization of the incident signal is measured and used to determine an empirical PDF. Similarly, the amount of correlation between ground scatter samples from different transmit sequences within the same integration interval is a quantity that can be determined experimentally and used to develop an empirical model.

Appendix I   Numerical Error in Ray Tracing Results

AI.1   Introduction

The numerical error in ray tracing results are briefly presented here. Specifically, the error in the calculated path length of a ray obtained through ray tracing will be determined as a function of both the truncation error in numerical integration and the resolution of the electron density profile grid.

AI.2   Numerical Integration Error

As discussed in Chapter 2, the numerical integration of ray paths is performed using a fourth-order Runge-Kutta (RK4) method that has a local truncation error of $O(h^5)$. The local truncation error for a given step size may be estimated by halving the step size and then taking the difference of the results [*Kincaid et al.*, 2009]. The cumulative error in path length is upper-bounded by the sum of the absolute values of local truncation errors. Figure AI.1 illustrates a typical ray path plot and Table AI.1 depicts the corresponding comparison of the total path length and cumulative path length error. Note that the upper-bound on path length error is on the order of tens of meters. From (3.6), calculated power is proportional to R^{-1} so a difference in path length of tens of meters relative to thousands of kilometers introduces a negligible amount of error.
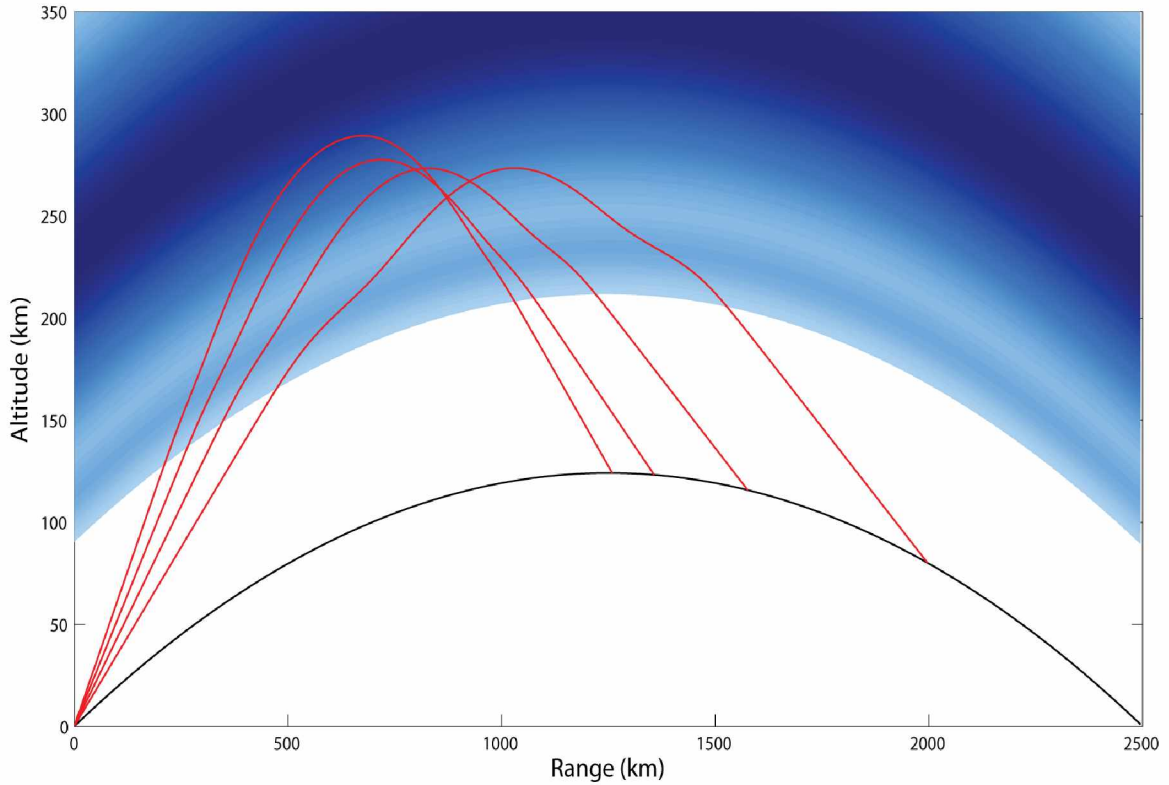
Figure AI.1: Typical ray path plot corresponding to tabulated data in Table AI.1.

Table AI.1: Comparison of ray path length and cumulative path length truncation error

Elevation Angle α (°)	Path Length P (km)	Error δP (m)	$\delta P/P$
5	2059	1.46	7×10^{-7}
10	1644	1.59	1×10^{-6}
15	1437	2.84	2×10^{-6}
20	1355	4.00	3×10^{-6}

AI.3 Grid Resolution Error

Another source of error in ray tracing results from modeling the continuous ionospheric electron density distribution as a finite sized grid of electron density values. One method of investigating the error associated with grid resolution is to find the difference in calculated ray paths for various grid resolutions. Figure AI.2 illustrates

curves of ray path length versus elevation angle calculated at the annotated grid resolutions.
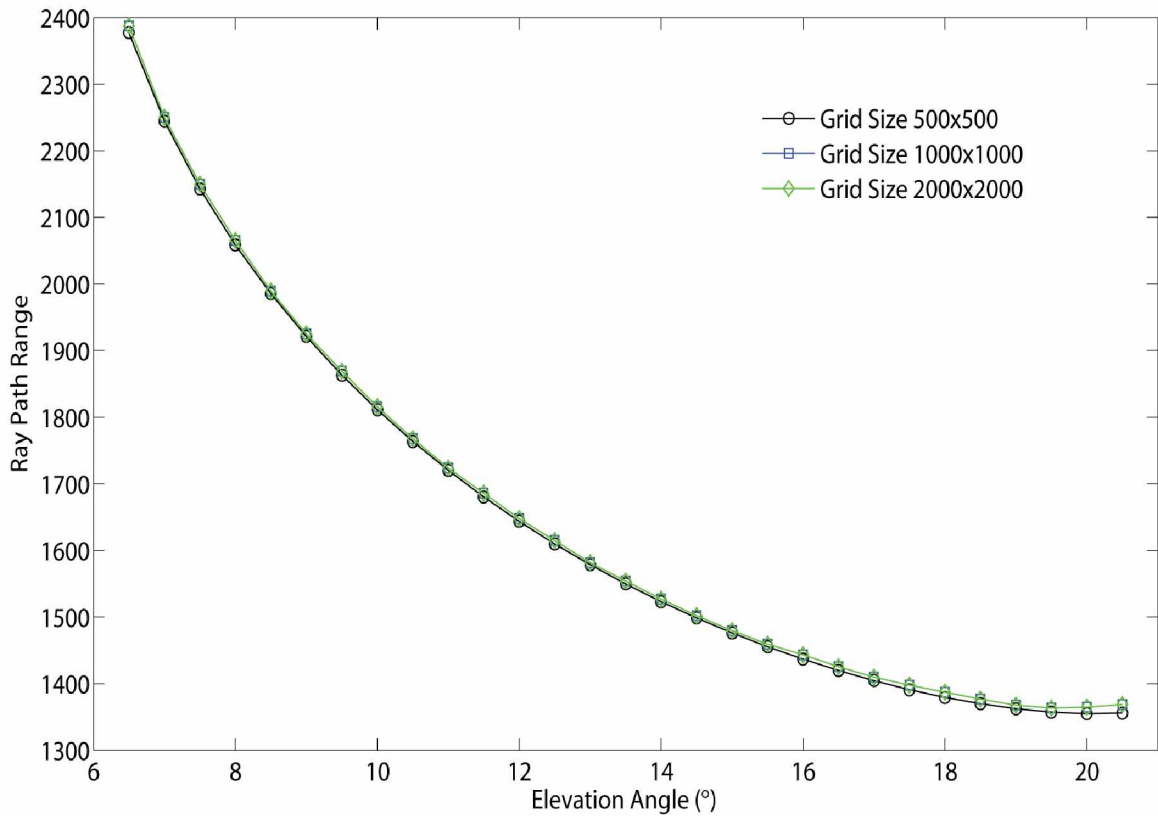
Figure AI.2: Curves of ray path length vs. elevation angle as the electron density profile grid size is increased.

Note in Figure AI.2 that the curves are indistinguishable for low elevation angles. At higher elevation angles, doubling the grid size from 500×500 to 1000×1000 results in a maximum path length difference on the order of 10 km. An error in path length of 10 km results in an error of ~0.05 dB in calculated power using (3.6) for path lengths greater than 1000 km. However, the greatest path length difference obtained upon further doubling the grid size from 1000×1000 to 2000×2000 is $< 10^{-6}$, which indicates there is a negligible change in the results for grid resolutions exceeding 1000×1000. Given that the phenomena under investigation here result in power

enhancements on the order of several decibels, the numerical error in the results due to finite grid resolution is ignored.

Appendix II   Investigation of Diffraction around an Artificial Layer

AII.1   Introduction

One phenomena of interest that was not investigated in Chapter 4 is the diffraction of a wave front around an artificial density layer. In Chapter 4 it was illustrated through ray tracing that rays tend to refract around artificial density layers which produces focusing effects observed as enhancements in the ground-scattered power. One may expect that when a wave front refracts around an artificial layer region that there may be interference effects or areas of constructive and destructive phase addition. Interference effects could result in a fading characteristic where the power enhancements produced by the artificial density layer are a function of range. Here a simplified investigation of diffraction effects is performed.

AII.2   Simplified Diffraction Problem

The effects of diffraction around an artificial layer were approximated by assuming a plane wave incident on an obstruction that is centered in azimuth of the beam pattern. The problem was reduced to one dimension and the pertinent geometry is illustrated in Figure AII.1.
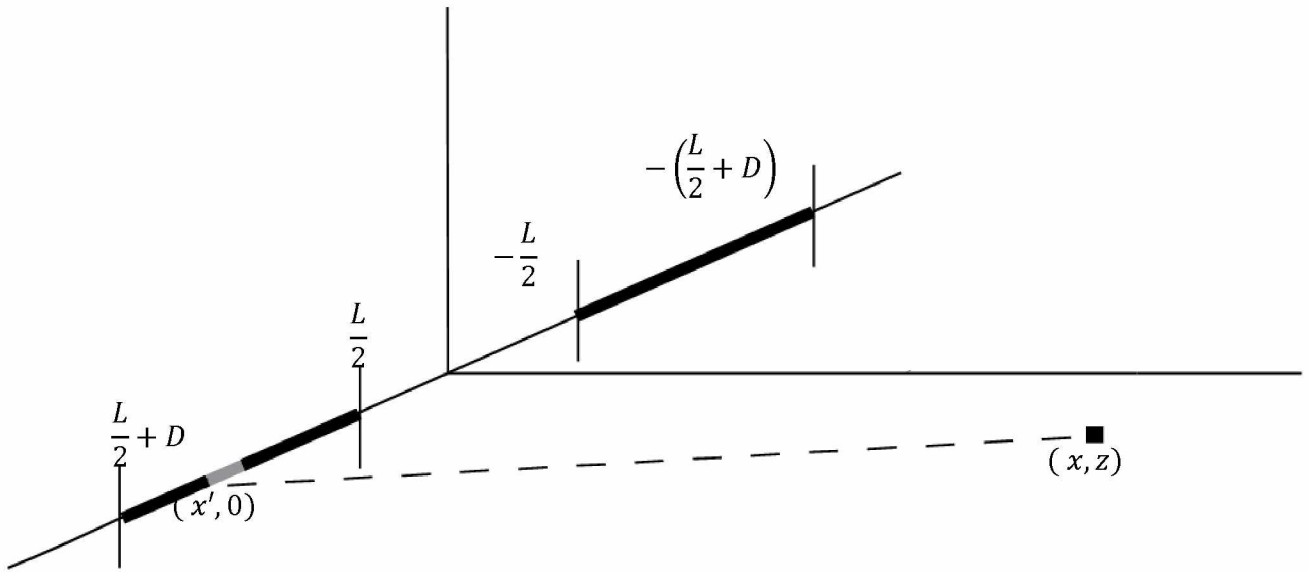
Figure AII.1: Illustration of aperture elements and geometry for simplified diffraction study.

The size of the aperture elements was estimated from the 3 dB azimuth beam pattern and the range of the artificial layer from the transmitter. Assuming an azimuth beam width of 6°, an artificial layer width of 30 km, and a distance of 800 km between the transmitter and the obstruction, the aperture lengths annotated in Figure AII.1 are $L = 30$ km and $D = 27$ km.

In addition, whether the curvature of the waves emanating from the aperture should be accounted for in the calculation of intensity depends on the size of the aperture with respect to the range at which the intensity is being calculated. As a general rule, the boundary between the Fresnel and Fraunhofer diffraction regions is approximately given by $F = 1$ where F is

$$F = \frac{a^2}{\lambda P}. \tag{AII.1}$$

In (AII.1) a is the largest linear dimension of the aperture, λ is the wavelength, and P is the distance to the point at which the intensity is calculated. Given $a = D \cong 27$ km and $\lambda = 30$ m, the boundary between Fresnel and Fraunhofer diffraction regions is at

$P \cong 2 \times 10^4$ km. The intensity at values of P in the range $[600, 800]$ km is desired which implies that $F > 1$ and the curvature of the waves must be accounted for in calculating intensity. The expression for the scalar E-field at a range R given an aperture surface S is

$$\bar{E} = \frac{j\beta}{2\pi} \int_S \frac{\bar{E}(x',y',0)}{R} e^{-j\beta R} dS. \tag{AII.2}$$

Using the geometry illustrated in Figure AII.1, the values of the variables in (AII.2) are

$$\begin{cases} \bar{E}(x',y',0) = E_0 \\ R = \sqrt{(x-x')^2 + z^2} \\ dS = dx' \end{cases} \tag{AII.3}$$

After making two change of variable substitutions, the expression in (AII.3) may be reduced to

$$\bar{E}(x,z) = -\frac{j\beta}{2\pi} \int_{\theta_1}^{\theta_2} E_0\, e^{-j\beta z \sec\theta} \sec\theta d\theta - \frac{j\beta}{2\pi} \int_{\theta_3}^{\theta_4} E_0 e^{-j\beta z \sec\theta} \sec\theta d\theta \tag{AII.4}$$

where the limits of integration are given by

$$\begin{cases} \theta_1 = \tan^{-1}\left(\left(x - \frac{L}{2}\right) \Big/ z \right) \\ \theta_2 = \tan^{-1}\left(\left(x - \left(\frac{L}{2} + D\right)\right) \Big/ z \right) \\ \theta_3 = \tan^{-1}\left(\left(x + \left(\frac{L}{2} + D\right)\right) \Big/ z \right) \\ \theta_4 = \tan^{-1}\left(\left(x + \frac{L}{2}\right) \Big/ z \right) \end{cases} \tag{AII.5}$$

At this point the expression in (AII.4) is evaluated numerically and the intensity is calculated as

$$I = \frac{1}{2\eta_0} |\bar{E}|^2. \tag{AII.6}$$

AII.3 Results

Figure AII.2 (a)-(b) illustrate plots of intensity evaluated using (AII.4) and (AII.6) for $L = 0$ km and $L = 30$ km and correspond to the absence or presence of an artificial layer respectively. Note in Figure AII.2 (b) that the artificial layer produces a power reduction in the center of the beam along the ground as compared to Figure AII.2 (c) because waves emanating from the aperture have not "filled in" the obstructed area at these ranges. Although the presence of an artificial layer significantly affects the intensity on the ground, we are interested in the effect on the scattered power.

Given plots of intensity along the ground, the scattered power is proportional to the sum of the intensity over the illuminated area. Assuming the illuminated area fills the beam in azimuth (x dimension) and is $\cong c\tau \cong 12$ km in ground range (z dimension), the scattered power along the ground given the plots illustrated in Figure AII.2 (a)-(b) is depicted in Figure AII.2 (c). Note that the only difference between the curves in Figure AII.2 (c) is a reduction of the mean profile by $\cong 2$ dB in the presence of an artificial layer because the intensity on the ground is effectively averaged over a large spatial area. Recalling the large variance in observed ground-scattered power discussed in Chapter 4, we do not expect diffraction to play an important role in the observed ground-scattered power in the presence of an artificial layer.
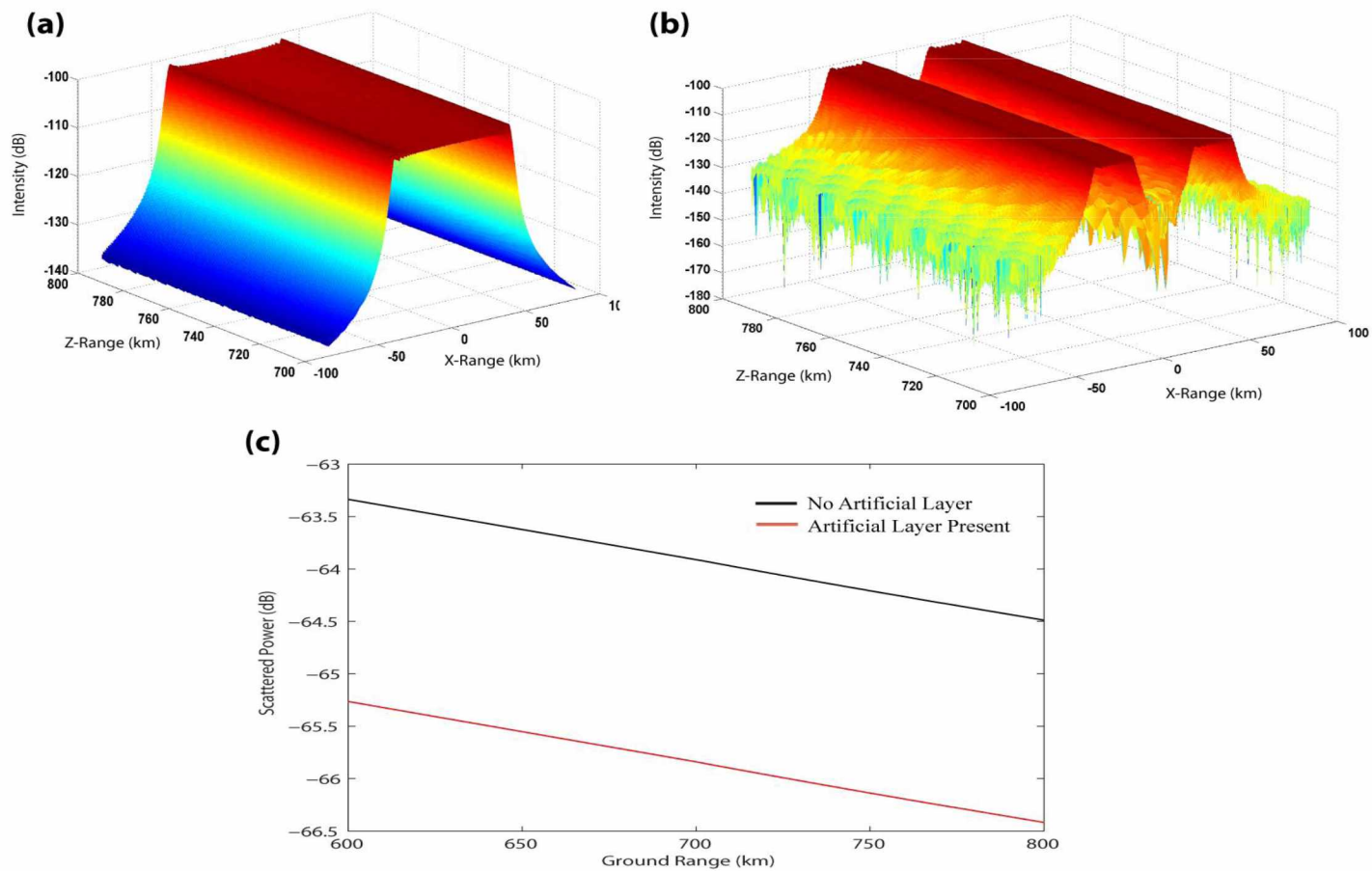
Figure AII.2: Plots of intensity and scattered power. (a) depicts the calculated intensity along the ground in the absence of an artificial layer. (b) illustrates the calculated intensity along the ground in the presence of an artificial layer. (c) depicts the scattered power versus ground range given the intensity plots in (a) and (b). Note that the values of intensity and power in (a)-(c) do not reflect absolute values and only illustrate the trend.

Appendix III Random Variable Transformations & Numerical Implementation

AIII.1 Introduction

In Chapter 5 a number of random variable transformations are performed to model the effects of random polarization and noise processes on a given distribution of ground-scattered power. In this chapter, a brief introduction to performing random variable transformation is presented followed by an illustration of the random variable transformations that are performed in Chapter 5. In addition, challenges encountered in obtaining the PDF of the polarization factor and the implemented solutions in numerical simulation are presented.

AIII.2 Random Variable Transformations

Consider a random variable (RV) X with the corresponding PDF $p_x(x)$. Now suppose that a new RV Y is defined as a function of X, say $Y = h(X)$. Over any monotonic range of $h(X)$, we can find the PDF of Y by equating the areas under the PDF curves

$$
\begin{aligned}
|p_y(y)dy| &= |p_x(x)dx| \\
p_y(y) &= p_x(x)\left|\frac{dx}{dy}\right|
\end{aligned}
\qquad\text{(AIII.1)}
$$

which can be expressed in terms of Y alone by using the inverse function $X = h^{-1}(Y)$ as

$$
p_y(y) = p_x(h^{-1}(Y))\left|\frac{dh^{-1}(Y)}{dy}\right|. \qquad\text{(AIII.2)}
$$

Note that if $h(X)$ is not monotonic over the entire range of values of X, then multiple values of X yield the same Y. However, each monotonic range of X can be treated as a mutually exclusive set so that the cumulative PDF of Y can be expressed as

$$
p_y(y) = p_x\left(h_1^{-1}(Y)\right)\left|\frac{dh_1^{-1}(Y)}{dy}\right| + p_x\left(h_2^{-1}(Y)\right)\left|\frac{dh_2^{-1}(Y)}{dy}\right| + \cdots \qquad\text{(AIII.3)}
$$

where the ith monotonic region is denoted by the subscript on the transformation function $h(X)$ [*Carlson et al.*, 2002].

In Chapter 5, we repeatedly perform transformations of a RV from linear units to decibels and vice-versa. Given a RV X in linear units bounded by the range $[0, \infty]$, the transformation $Y = 10 \log_{10} X$ is monotonically increasing so the PDF of Y may be expressed using (AIII.2) as

$$p_y(y) = p_x\left(10^{Y/10}\right)\left|10^{Y/10}(1/10)\ln 10\right|. \qquad \text{(AIII.4)}$$

Similarly, the RV transformation from decibels to linear units is found to be

$$p_y(y) = p_x(10 \log_{10} Y)\left|\frac{1}{Y}\left(\frac{10}{\ln 10}\right)\right|. \qquad \text{(AIII.5)}$$

AIII.3 Numerical Model of the Polarization Factor

In the previous section, the general expression for a RV transformation and the specific expressions for RV transformations between linear and decibel units were derived. In addition to these RV transformations, in Chapter 5 we perform the transformation

$$X = A \cos^2 \theta + B \sin^2 \theta \qquad \text{(AIII.6)}$$

where θ is a RV with an arbitrary PDF and the terms A and B are constant coefficients. A number of challenges arise when practically evaluating the PDF of X using (AIII.2). These challenges include the fact that θ has an arbitrary PDF so an analytical expression for $p_\theta(\theta)$ is not available and also that the PDF of X may have discontinuities under the transformation in (AIII.6).

AIII.3.1 Modeling Arbitrary θ Distribution

First, let us consider the problem that θ may have an arbitrary PDF. We overcome this problem by approximating $p_\theta(\theta)$ as the sum of a large number of weighted uniform distributions. The objective of this approach is to solve the transformation in (AIII.6) for a narrow uniform distribution so that the solution for an

arbitrary distribution may be found as a weighted sum of simpler solutions. Figure AIII.1 depicts this approach by illustrating a $p_\theta(\theta)$ that is Gaussian distributed along with an approximate $p^*_\theta(\theta)$ composed of $N = 40$ weighted uniform distributions.
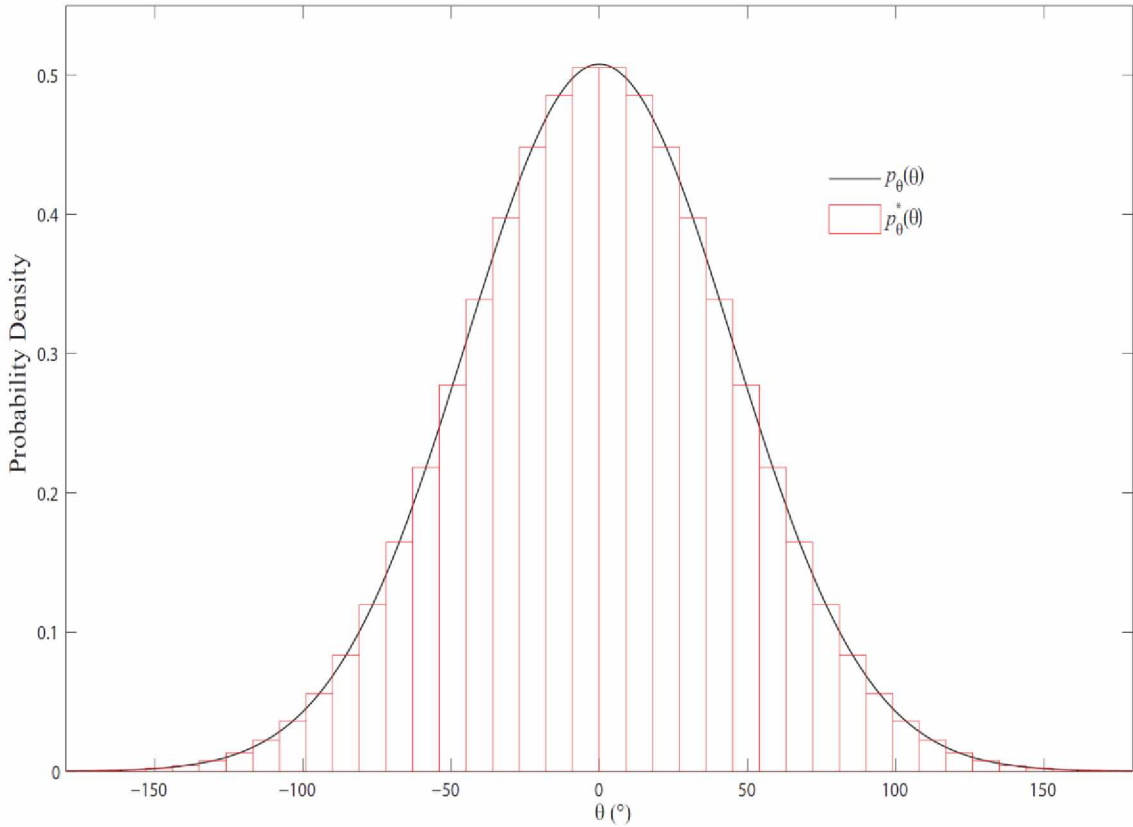
Figure AIII.1: Illustration of an arbitrary $p_\theta(\theta)$ distribution along with an approximate $p^*_\theta(\theta)$ distribution composed of the sum of weighted, narrow, uniform distributions.

Given the range $0 - 2\pi$ subdivided into N intervals, the approximate PDF of an arbitrary distribution $p^*_\theta(\theta)$ may be expressed as

$$p^*_\theta(\theta) = \sum_{i=1}^{N} w_i p_{\theta-Uniform}(\theta) \qquad \text{(AIII.7)}$$

where $p_{\theta-Uniform}(\theta)$ is a uniform distribution of width $2\pi/N$ in the ith interval and the weights w_i are

$$w_i = \frac{2\pi}{N} p_\theta(\theta_i). \qquad \text{(AIII.8)}$$

In (AIII.8), the value θ_i is chosen to be the midpoint of the ith interval. Before illustrating the solution to the transformation in (AIII.6) for a narrow uniform distribution, we first discuss the problem of discontinuities that may arise under the transformation in (AIII.6).

AIII.3.2 Discontinuities in Polarization Factor PDF

Consider the RV transformation in (AIII.6) for the case $B = 0$ and $p_\theta(\theta)$ is a uniform distribution over $[0, 2\pi]$. The expression for $p_x(x)$ in decibel units may be found using (AIII.3) as

$$p_x(x) = \left(1/(A10)\right)(\log 10)\, \frac{10^{x/10}}{\pi\left[10^{x/10}\left(1 - 10^{x/10}\right)\right]^{1/2}}. \tag{AIII.9}$$

At the values $X = (0, -\infty)$, $p_x(x)$ asymptotically approaches $+\infty$ which prevents practical representation of $p_x(x)$ in simulation. However, recall from Chapter 5 that the PDF $p_x(x)$ is utilized in a convolution operation to find the effect of random polarization on the received signal distribution. Reflect that the convolution of two PDF's is expressed as

$$p_z(z) = p_x * p_y = \int p_x(\lambda)\, p_y(z - \lambda)d\lambda, \tag{AIII.10}$$

and that the cumulative distribution function (CDF) of $p_z(z)$ in (AIII.10) is

$$F_z(z) = \int_{-\infty}^{z} p_z(\alpha)d\alpha = \int_{-\infty}^{z}\left[\int p_x(\lambda)\, p_y(\alpha - \lambda)d\lambda\right]d\alpha. \tag{AIII.11}$$

If we change the order of integration in (AIII.11) we obtain

$$F_z(z) = \int p_x(\lambda)\left[\int_{-\infty}^{z} p_y(\alpha - \lambda)d\alpha\right]d\lambda$$

$$\therefore$$

$$F_z(z) = \int p_x(\lambda)F_Y(\alpha - \lambda)\, d\lambda$$

$$\therefore$$

$$F_z(z) = p_x * F_Y = F_x * p_Y \tag{AIII.12}$$

where the CDF of the result is expressed as a convolution of a PDF and a CDF. Although we illustrated in (AIII.9) that $p_x(x)$ has discontinuities, the CDF of X can be shown to be

$$F_x(x) = \frac{1}{\pi} \cos^{-1}\left(1 - 2\left(10^{x/10}\right)\right), \qquad \text{(AIII.13)}$$

which is continuous in the range $X \in [-\infty, 0]$. Therefore, instead of directly calculating the PDF of the received signal power given the PDF of the incident signal power and the possibly discontinuous PDF of the polarization factor, we calculate the CDF of the received signal using the relationship in (AIII.12) because there exists a practical representation of the CDF of the polarization factor even when the PDF is discontinuous. The PDF of the received signal distribution may then be found by differentiating the result calculated in (AIII.13).

AIII.3.3 Linear Approximation of the Polarization Factor PDF

We demonstrated in the previous section that an analytic solution can be found to the RV transformation in (AIII.6) in the specific case where $B = 0$ and $p_\theta(\theta)$ is a uniform distribution over $[0, 2\pi]$. However, recall that we wish to find the RV transformation given an arbitrary $p_\theta(\theta)$ distribution which we have modeled as a weighted sum of narrow uniform distributions, $p_{\theta-Uniform}(\theta)$, using (AIII.7) and (AIII.8). Given that the individual uniform distributions span a small angular width θ_W, we may replace the terms $\cos^2 \theta$ and $\sin^2 \theta$ in (AIII.6) with their linear approximations found from a Taylor series expansion. The linear approximation to the RV transformation in (AIII.6) considering a narrow uniform distribution centered at θ_i is

$$X = A^* + (\theta - \theta_i)B^* \qquad \text{(AIII.14)}$$

where the terms A^* and B^* are constant coefficients given by

$$\begin{cases} A^* = (A \cos^2 \theta_i + B \sin^2 \theta_i) \\ B^* = [2(B - A) \sin \theta_i \cos \theta_i] \end{cases} \qquad \text{(AIII.15)}$$

The PDF of a narrow uniform distribution spanning a width θ_W centered at θ_i under the RV transformation in (AIII.14) can be found from (AIII.2) to be the constant

$$p_x(x) = \left|\frac{1}{B^*}\right| \frac{1}{\theta_W}. \tag{AIII.16}$$

Further, the CDF of (AIII.16) in decibel units can be expressed using (AIII.4) as

$$F_v(v) = \left|\frac{1}{B^*}\right| \frac{\ln 10}{10\theta_W} \left(10^{v/10} - 10^{v_{min}/10}\right) \tag{AIII.17}$$

where $v_{min} = 10 \log_{10} \min(X)$.

Finally, given an arbitrary $p_\theta(\theta)$ distribution which we have approximated using narrow uniform distributions and the linear approximation to the RV transformation in (AIII.14), we may express the cumulative CDF as

$$F^*_v(v) = \sum_{i=1}^{N} w_i F_v(v). \tag{AIII.18}$$

In Chapter 5, we use the expression in (AIII.18) to develop the CDF of the polarization factor $\bar{P}$ given an arbitrary $p_\theta(\theta)$ distribution. The CDF of $\bar{P}$ in decibel units is convolved with the PDF of an incident signal power distribution to determine the cumulative distribution of received signal power which is subsequently differentiated to obtain a PDF.

References

Box, George E. P., G. M. Jenkins, and G. C. Reinsel (1994), *Time Series Analysis*, Prentice-Hall, Inc., Englewood, New Jersey.

Bristow, W. A., and R. A. Greenwald (1995), Estimating Gravity Wave Parameters from Oblique High-Frequency Backscatter: Modeling and Analysis, *J. Geophys. Res.*, 100(A3), 3639–3648, doi:10.1029/94JA02704.

Budden, K. G. (1985). *The propagation of radio waves: Theory of radio waves of low power in the ionosphere and magnetosphere*. Cambridge University Press, Cambridge.

Carlson, B. A, P. B. Crilly, and J. C. Rutledge (2002). *Communication Systems*, McGraw-Hill, New York, New York.

Chen, F. (1984). *Introduction to Plasma Physics and Controlled Fusion*. Plenum Press, New York, New York.

Coleman, C. J. (1998), A ray tracing formulation and its application to some problems in over-the horizon radar. *Radio Science*, volume 33, pp 1187-1197

Coleman, C. J. (1997), On the simulation of backscatter ionograms. *Journal of Atmospheric and Solar-Terrestrial Physics*, volume 59, pp 2089-2099

Coleman, C. J. (1994), A coordinate registration algorithm based on numerical ray tracing. *Research report RR-0009, DSTO*

Davies, K. (1965). *Ionospheric Radio Propagation*. U.S Dept. of Commerce, National Bureau of Standards, Washington D.C.

Greenwald, R. A., K. B. Baker, R. A. Hutchins, and C. Hanuise (1985), An HF phased array radar for studying small-scale structure in the high-latitude ionosphere, *Radio Sci.*, *20*, 63.

Greenwald, R. A., K. B. Baker, J. R. Dudeney, and M. Pinnock (1995), DARN/SuperDARN: A global view of the dynamics of high-latitude convection, *Space Sci. Rev.*, *71*, 761.

Kelso, J. M. (1964). *Radio Ray Propagation in the Ionosphere*. McGraw-Hill Inc., New York.

Kendall E., R. Marshall, R. T. Parris, A. Bhatt, A. Coster, T. Pedersen, P. Bernhardt, and C. Selcher (2010), Decameter structure in heater-induced airglow at the High frequency Active Auroral Research Program facility, *J. Geophys. Res.*, 115, A08306, doi:10.1029/2009JA015043.

Kincaid, D., and W. Cheney (2002). *Numerical Analysis*. American Mathematical Society, Providence, Rhode Island.

Moore, R. K., K. A. Soofi, and S. M. Purduski (1980), A Radar Clutter Model: Average Scattering Coefficients of Land, Snow, and Ice, *IEEE Transaction on Aerospace and Electronic Systems*, vol. AES-16, no. 6, pp. 783-799, doi:10.1109/TAES.1980.309003.

Moore, R. K. (2008) Ground Echo, in *Radar Handbook.*, edited by M. Skolnik., pp. 16.1-16.63, McGraw-Hill, Inc., New York.

Nathanson, F. E., J. P. Reilly, and M. N. Cohen (1991), Sea and Land Backscatter, in *Radar Design Principles Signal Processing and Environment*, 2nd ed., pp.314-323, McGraw-Hill, Inc., New York.

Pedersen, T., B. Gustavsson, E. Mishin, E. Kendall, T. Mills, H. C. Carlson, and A. L. Snyder (2010), Creation of artificial ionospheric layers using high-power HF waves, *Geophys. Res. Lett.*, 37, L02106, doi:10.1029/2009GL041895.

Pedersen, T., B. Gustavsson, E. Mishin, E. MacKenzie, H. C. Carlson, M. Starks, and T. Mills (2009),Optical ring formation and ionization production in high-power HF heating experiments at HAARP, *Geophys. Res. Lett.*, 36, L18107, doi:10.1029/2009GL040047.

Peebles, P. Z., Jr. (1998), Radar Cross Section, in *Radar Principles*, pp. 213-230, John Wiley & Sons, Inc., New York.

Rao, N. N. (2004). *Elements of Engineering Electromagnetics*. Pearson Education Inc., Upper Saddle River, New Jersey.

Riley, K. F., M. P. Hobson, and S. J. Bence (2006). *Mathematical Methods for Physics and Engineering: A Comprehensive Guide*. Cambridge University Press, Cambridge.

Theurer, T., and W. A. Bristow (2012). Observations and effects of artificial density layers on oblique high-frequency backscatter, *Radio Sci.*, doi:10.1029/2011RS004861.

Ulaby, F. T. (1980), Vegetation Clutter Model, *IEEE Transactions on Antennas and Propagation*, vol. AP-28, no. 4, pp. 538-545, doi:10.1109/TAP.1980.1142377

Wright, D. M., J. A. Davies, T. K. Yeoman, T. R. Robinson, and H. Shergill (2006), Saturation and hysteresis effects in ionospheric modification experiments observed by the CUTLASS and EISCAT radars, *Ann. Geophys.*, 24, 543–553

Wright, D. M., R. S. Dhillon, T. K. Yeoman, T. R. Robinson, E. C. Thomas, L. J. Baddeley, and S. Imber, (2009) Excitation thresholds of field-aligned irregularities and associated ionospheric hysteresis at very high latitudes observed using SPEAR-induced HF radar backscatter, *Ann. Geophys.*, 27, 1 – 9